A Study of the Dust Mineralogy of Low and High Mass Post-Main Sequence Stars

A THESIS
SUBMITTED TO THE FACULTY OF THE GRADUATE SCHOOL
OF THE UNIVERSITY OF MINNESOTA
BY

Ryan Alan Arneson

IN PARTIAL FULFILLMENT OF THE REQUIREMENTS
FOR THE DEGREE OF
Doctor of Philosophy

Advisor:
Robert D. Gehrz

December, 2017

Acknowledgements

I would like to thank my advisor, Bob Gehrz, who provided me with well-defined research projects to study and for allowing me to take his place as a guest observer onboard SOFIA. Flying on SOFIA to observe TX Per was a once-in-a-lifetime opportunity. I am appreciative of his guidance and support.

I would like to thank Adam Bolton, for introducing me to the field of astrophysics and for giving me my first research experience. Adam's influence has had a lasting effect.

I cannot thank my So-Arneson family enough for all of their support throughout the years. To my Mom and Dad, thank you for allowing me to pursue my dreams and for being my role models. To Grandma, thank you for giving me my first telescope and for always inspiring me.

Most of all I would like to thank my wife, Jacky So, for her constant support and encouragement. This thesis would not have been possible without her.

Dedication

To Little Bunny, my other whole

Abstract

Luminous blue variables (LBVs) represent a post-main sequence phase in which massive stars ($M_i \geq 20\ M_\odot$, Langer et al., 1994) lose a considerable amount of mass via giant eruptions and minor outbursts creating circumstellar nebula. RV Tauri and yellow semi-regular (SRd) variables are two classes of post-main sequence stars with a typical mass of ~ 0.7 $M_\odot$ (Tuchman et al., 1993) that are thought to be the immediate precursors of planetary nebulae (PNe) and have been termed "proto-planetary nebulae" (PPNe). These classes of stars are responsible for creating unique circumstellar environments where various dust species grow, undergo processing and dissipate into the interstellar medium (ISM). This thesis studies the dust mineralogy and mass-loss history of both high mass (LBVs) and low mass (RV Tauri and SRd variables) post-main sequence stars using SOFIA/FORCAST 5 – 40 μm mid-infrared imaging and spectroscopy.

In particular, I present SOFIA/FORCAST 5-40 μm mid-infrared imaging of the dust surrounding the LBV candidates MN 90 and HD 168625 to quantify the mineral abundances of the circumstellar dust and constrain the evolutionary state of these objects. The images between 7.7 – 37.1 μm of HD 168625 compliment previously obtained mid-IR imaging. The dust color temperature and optical depth maps of HD 168625 show evidence for the limb-brightened peaks of an equatorial torus. Our image at 37.1 μm of MN 90 shows a limb-brightened, spherical dust shell. A least-squares fit to the spectral energy distribution of MN 90 yields a dust temperature of 69 ± 3 K, with the peak of the emission at 42 μm. Similarly for HD 168625, I estimate a dust temperature of 160 ± 7 K, with the peak of the emission at 18 μm. Radiative transfer calculations of HD 168625 using **2-D**ust estimate that mass-loss occurred 2.6×10^3 years ago at a rate of $1.3 \times 10^{-7}\ M_\odot\, yr^{-1}$ to create a dust torus/shell with a dust mass of 2.4×10^{-3} $M_\odot$. Similarly, I estimate for MN 90 that mass-loss occurred 6×10^3 years ago at a rate of $8.3 \times 10^{-6}\ M_\odot\, yr^{-1}$ to create a dust shell with a dust mass of $2.5 \times 10^{-2}\ M_\odot$. The **2-D**ust calculations suggest the presence of oxygen rich silicates around both stars.

I further present a SOFIA/FORCAST 5 – 40 μm mid-infrared grism spectroscopic survey that examines the mineralogy of the circumstellar dust in a sample of RV Tauri

and SRd variable stars. A mineralogical model for each star indicates the presence of both carbon rich and oxygen rich dust species–contrary to simple dredge-up models–with a majority of the dust in the form of amorphous carbon and graphite. The oxygen rich dust is primarily in the form of amorphous silicates. For most of the systems, the analysis suggests that the grains are relatively large and have undergone significant processing, supporting the hypothesis that the dust is confined to a Keplerian disk and that the heavily processed, central regions of the disk are viewed from a nearly face-on orientation. These results help to determine the physical properties of post-main sequence circumstellar environments and to constrain models of post-main sequence mass loss and planetary nebula formation.

Contents

List of Tables

List of Figures

Chapter 1

Introduction

Post-main sequence stars are important producers of dust in the universe. As the stars evolve off the main sequence, they shed mass in outflows that produce a variety of dust species that enrich the interstellar medium (ISM). In our own Galaxy, dust enrichment of the ISM is dominated by the dusty winds from low to intermediate mass stars (1 – 8 $M_{\odot}$) during the asymptotic giant branch (AGB) phase (Gehrz, 1989). The relative contribution from high mass stars (M > 8 $M_{\odot}$) is also important and is often used to explain the substantial dust abundances observed in high-redshift galaxies and quasars (Michałowski et al., 2010; Dwek et al., 2007; Beelen et al., 2006; Bertoldi & Cox, 2002). If the dust-forming stars show the standard cosmic element mixture in their photospheres, they mainly form silicate dust in their stellar outflows (see Molster et al. 2010 for a review of observations). With progressive changes in the surface element mixture they start to form completely different dust species. The best known example is the change of spectral type from M over S to C for stars of low and intermediate mass (initial mass M_i < 8 $M_{\odot}$) during their evolution on the thermally pulsing AGB. This results from the dredging up of freshly produced carbon from He burning in the core region to the surface after each pulse. The change in chemistry and spectral type from being oxygen-rich for M stars to carbon-rich for C stars is accompanied by a drastic change in the dust production from silicate to carbon production. Studying the mass-loss history and mineral species of post-main sequence stars provides insight into the physical parameters of the star and their role in the enrichment of the ISM.

Luminous blue variables (LBVs) represent a post-main sequence phase in which

massive stars ($M_i \geq 20\ M_\odot$, Langer et al., 1994) lose a considerable amount of mass via giant eruptions and minor outbursts. These giant eruptions are responsible for producing circumstellar nebulae with sizes of about 1 – 2 pc and expansion velocities anywhere from $\sim 10\ \mathrm{km\,s^{-1}}$ to $\sim 1000\ \mathrm{km\,s^{-1}}$ (as in the case of η Car, Weis, 2012) that are then shaped by wind-wind interactions (van Marle et al., 2007). The morphology of the nebula discloses the mass-loss history and evolutionary stage of the central star and the circumstellar environment. Shenoy et al. (2016) and Gordon et al. (2017) are paradigms on mass-loss histories for which the analysis presented in this thesis is based. By imaging these nebulae at a range of wavelengths, we can study their structure, estimate the dust composition, and quantify the dust temperature and total mass. These parameters will help to determine the physical properties of the circumstellar environments and to constrain the importance of eruptive mass-loss in high-mass, post-main sequence stellar evolution.

RV Tauri and yellow semi-regular (SRd) variables are two classes of post-asymptotic giant branch (post-AGB) stars that lie along the horizontal track on the Hertzsprung-Russell (H-R) diagram linking AGB stars to planetary nebulae (PNe). They are thought to be the immediate precursors of PNe and have been termed "proto-planetary nebulae" (PPNe). RV Tauri stars are characterized by semi-regular, bimodal variability (possibly resulting from interaction with a binary companion; Waelkens & Waters, 1993; Percy, 1993; Fokin, 1994), a high mass-loss rate, and often a prominent infrared (IR) excess (Gehrz & Woolf, 1970; Gehrz, 1972; Gehrz & Ney, 1972). SRd variables are similar to RV Tauri stars in many respects but are probably single star systems, as indicated by the absence of regular pulsations (Percy & Ursprung, 2006). RV Tauri stars are a loosely defined subclass of Population II Cepheid variables named after the prototype RV Tau. They are defined as luminous (I-II) mid-F to K supergiants with a typical mass of $\sim 0.7\ \mathrm{M_\odot}$ (Tuchman et al., 1993; Fokin, 1994). It has been suggested that RV Tauri stars are binary systems with circumstellar dust confined to a disk (Van Winckel et al., 1999) which emit in the thermal IR. By modeling the thermal IR spectrum emission we can determine the source of the IR-excess, identify the dust species present and quantify fundamental dust properties, such as the grain size distribution and dust temperature. These parameters help to determine the physical properties of the post-AGB circumstellar environment and to constrain models of post-AGB mass loss and

planetary nebula formation.

In this thesis I present a study of the mineralogy and mass-loss of 2 candidate LBV stars, 15 RV Tauri and 3 SRd variable stars. All of the stars presented in this thesis have been observed using the Faint Object infraRed CAmera for the SOFIA Telescope (FORCAST) onboard NASA's airborne Stratospheric Observatory for Infrared Astronomy (SOFIA). In Chapter 2, I present our work using imaging and radiative transfer modeling to probe the mass-loss of the luminous blue variable candidates MN 90 and HD 168625 in the 5 – 40 μm range (Arneson et al., 2017, in preparation). In Chapter 3, I utilize near infrared grism spectroscopy between 5 – 40 μm to study the mineralogy of both RV Tauri stars and SRd variable stars (Arneson et al., 2017). A summary is provided in Chapter 4.

Chapter 2

SOFIA/FORCAST Observations of the Luminous Blue Variable Candidates MN 90 and HD 168625

This chapter has been submitted for publication in the Astronomical Journal with the following author list: Arneson, R. A., Shenoy, D. P., Smith, N., and Gehrz, R. D.

Abstract

We present SOFIA/FORCAST imaging of the dust surrounding the luminous blue variable (LBV) candidates MN 90 and HD 168625 to quantify the mineral abundances of the circumstellar dust and constrain the evolutionary state of these objects. Our image at 37.1 μm of MN 90 shows a limb-brightened, spherical dust shell. Our images between 7.7 – 37.1 μm of HD 168625 compliment previously obtained mid-IR imaging. The dust color temperature and optical depth maps of HD 168625 show evidence for the limb-brightened peaks of an equatorial torus. A least-squares fit to the spectral energy distribution of MN 90 yields a dust temperature of 69 ± 3 K, with the peak of the emission at 42 μm. Similarly for HD 168625, we

estimate a dust temperature of 160 ± 7 K, with the peak of the emission at 18 μm. These results help to constrain models of LBV nebulae and their circumstellar environments.

2.1 Introduction

It is widely recognized that luminous blue variables (LBVs) represent a post-main sequence phase in which massive stars ($M_i \geq 20\ M_\odot$, Langer et al., 1994) lose a considerable amount of mass via giant eruptions and minor outbursts. From the expansion velocities of known LBV nebulae, a dynamical age of a few 10^4 years is usually inferred, which points to a very short-lived evolutionary phase – only about 40 are known (Clark et al., 2005; Weis, 2011; Nazé et al., 2012). Although the category is still not clearly defined, these objects exhibit a high luminosity ($\geq 10^{5.5}\ L_\odot$), low amplitude photometric variability (~ 0.1 mag) on timescales ranging from weeks to months, and a larger, irregular photometric variability, called S Dor variability, with amplitudes of 1 – 2 mag occuring on timescales of years to decades with mass-loss rates of $\sim 10^{-5} - 10^{-4}$ $M_\odot\, yr^{-1}$. In addition, some LBVs exhibit giant eruptions, η Car being the most famous example (Humphreys et al., 1999). These giant eruptions are responsible for producing circumstellar nebulae with sizes of about 1 – 2 pc and expansion velocities anywhere from $\sim$ 10 $\mathrm{km\,s^{-1}}$ to $\sim$ 1000 $\mathrm{km\,s^{-1}}$ (as in the case of η Car, Weis, 2012) that are then shaped by wind-wind interactions (van Marle et al., 2007). These nebulae can have various morphologies; Weis (2011) estimates 50% are bipolar, 40% spherical, and 10% are irregular. The bipolar nebulae may be formed from density gradients in the wind (Frank et al., 1995), different mass-loss episodes in which the wind changes from equatorial to polar during the bistability jump (Smith et al., 2004), or the rotation of the star (Dwarkadas & Owocki, 2002; Smith & Townsend, 2007). Thus, the morphology of the nebula discloses the mass-loss history and evolutionary stage of the central star and the circumstellar environment.

In this work we present 5 – 40 μm mid-IR observations with the Faint Object infraRed CAmera for the SOFIA Telescope (FORCAST; Herter et al., 2012) instrument on board the NASA Stratospheric Observatory for Infrared Astronomy (SOFIA; Becklin

et al., 2007; Gehrz et al., 2009; Young et al., 2012) of the two compact nebulae, MN 90 and HD 168625. By imaging these nebulae at a range of wavelengths, we can study their structure, estimate the dust composition, and quantify the dust temperature and total mass. These parameters will help to determine the physical properties of the circumstellar environments and to constrain the importance of eruptive mass-loss in post-main sequence stellar evolution. In Section 3.3 we summarize the observations and data reduction strategies of the stars observed. Section 3.4.2 describes the axisymmetric radiative transfer code **2-D**ust and the derived dust geometry parameters and inferred mass-loss histories. We discuss the results of our analysis of MN 90 and HD 168625 in Section 3.6 and finally we provide the conclusions in Section 3.7.

MN 90 (central star 2MASS J18455593-0308297) was discovered and catalogued by Gvaramadze et al. (2010) using the Multiband Imaging Photometer (MIPS; Rieke et al., 2004) aboard the *Spitzer Space Telescope* (Werner et al., 2004; Gehrz et al., 2007) in the MIPS Galactic Plane Survey (MIPSGAL; Carey et al., 2009), which mapped 278 deg^2 of the inner Galactic plane: $-65^\circ < l < -10^\circ$ and $10^\circ < l < 65^\circ$ for $|b| < 1^\circ$. It is one of a large number of similar shells found in MIPSGAL images that resemble the circumstellar nebulae of LBVs and late WN-type Wolf Rayet stars (WNL). The lack of optical counterparts for most of them indicates they are highly obscured (Wachter et al., 2010). Follow-up spectroscopy of some of the other MIPS Nebulae have revealed them to be LBVs, candidate LBVs or early-type supergiants (see the summary list in Kniazev et al., 2015). MN 90 is nearly circular and appears to be a limb-brightened shell with a star at the center. The star is undetected in *Swift* UV images, Palomar Observatory Sky Survey (POSS) visual images, and the ground-based visual images used to make the HST Guide Star Catalog. The distance to MN 90 is unknown and there is little information about its physical parameters. Wachter et al. (2010) included MN 90 along with a large sample of numerous similar shells for follow-up spectroscopy but ultimately did not report any spectra for this particular star. Based on the analysis of other stars in their sample, they grouped MN 90 along with other shells for which they predict the stars are early-type. Nazé et al. (2012) did not dectect any X-ray emission from MN 90 in their XMM-*Newton* survey of a sample of known and candidate LBVs. There is one other reference to MN 90 as a nebula; Mizuno et al. (2010) lists MN 90 as MGE029.5086-00.2090, but other than reporting a MIPSGAL flux at 24 μm, there is

nothing more specific about the central star. We are unaware of any other imaging or spectroscopy of MN 90 that may have been obtained. Hereafter we will use "MN 90" to refer to both the nebula and the central star.

HD 168625 (IRAS 18184–1623) was first identified as a candidate LBV by Chentsov & Luud (1989), who classified it as spectral type B5.6 ± 0.3 with $T_* \simeq 13000$ K. Its spectral type seems to vary from B2 (Popper & Seyfert, 1940) to B8 (Morgan et al., 1955), although no dramatic light-variations have been been reported in the last 40 years (van Genderen et al., 1992; Sterken et al., 1999). The lack of evidence for large variations kept HD 168625 from being classified as an LBV. However, it was found to be LBV-like by Hutsemekers et al. (1994) who, using near-infrared (near-IR) and visible imaging and spectroscopy, found a high mass-loss rate and a shell with two regions: an inner $10'' \times 13''$ elliptical ring and a perpendicular outer horn-shaped region suggesting a bipolar outflow. Nota et al. (1996) used deeper Hα imaging of the nebula to identify faint filaments in the bipolar structure that extended to $16'' \times 21''$, indicating that a LBV-like major outburst occurred $\sim 10^3$ years ago. Given its curious characteristics, HD 168625 has been the focus of several additional studies. Meixner et al. (1999) included it in their large, mid-infrared (mid-IR) proto-planetary nebula candidates survey and imaged it at 8.8, 12.5, and 20.6 μm, which revealed a toroidal dust shell. From mid-IR images at 4.7, 10.1, 11.6, and 19.9 μm, Robberto & Herbst (1998) used an analytical spherical model to derive a dust temperature of 135 K and a dust mass of 2.8×10^{-3} $M_\odot$. Similarly, Pasquali et al. (2002) used mid-IR imaging at 4 and 11 μm to derive a dust temperature of 113 K, and a nebular expansion velocity of 19 km s^{-1} using ground-based echelle spectra. O'Hara et al. (2003) modeled the morphology of the toroidal dust region using **2-D**ust and found a dust mass of $2.5 \pm 0.1 \times 10^{-3}$ $M_\odot$. Mahy et al. (2016) used far-infrared (far-IR) imaging and spectroscopy with optical spectra to constrain the CNO abundances of HD 168625 and the surrounding nebula to determine that the central star had an initial mass between 28 – 33 $M_\odot$ and lost its material after the blue supergiant phase. Smith (2007) was the first to question the origins of the filamentary bipolar structure of the nebula around HD 168625 and argued against the interaction between a faster wind of the star and slower ejections as a possible explanation, while other scenarios involving either the evolution of a single star or interactions between two massive stars were advanced. Namely, a single rotating star could eject an equatorial torus even if

it is not rotating at the critical speed. Presumably this can occur because the stars approach or violate the classical Eddington limit during their giant eruptions when the mass is ejected, allowing the star's rotation to be more influential at the resulting lower effective gravity. Taylor et al. (2014) found no evidence for a binary companion to HD 168625 from radial velocity monitoring and a modest rotation speed of 53 $\mathrm{km\,s^{-1}}$. The presence of a possible companion star was detected by Aldoretta et al. (2015) using interferometric observations. A wide-orbit companion with a projected separation of $1.15''$ was later confirmed by Martayan et al. (2016) using adaptive optics images, but there is no evidence that it is gravitationally bound to HD 168625 and is too distant to have any impact on the shaping of the nebula. The role companions play in the formation and evolution of LBV and LBV-like objects is still not well understood.

2.2 Observations & Data Reduction

The targets were observed with SOFIA/FORCAST during Guest Investigator (GI) Cycles 2 and 3. Descriptions of the SOFIA Observatory and its science instrument (SI) suite have been given by Becklin et al. (2007), Gehrz et al. (2009), and Young et al. (2012).

FORCAST is a dual-channel mid-IR imager covering the 5 – 40 μm range. Each channel uses a 256 $\times$ 256 pixel array and provides a distortion-corrected $3.2' \times 3.2'$ field of view with a scale of $0.768''$ $\mathrm{pix^{-1}}$. The Short Wave Camera (SWC) uses a Si:As blocked-impurity band (BIB) array optimized for $\lambda < 25$ μm, while the Long Wave Camera's (LWC) Si:Sb BIB array is optmized for $\lambda > 25$ μm. Observations were taken in standard two-position chop-and-nod mode with the direction of the nod matching the direction of the chop (NMC). The data were reduced by the SOFIA Science Center using the FORCAST Redux v1.0.1β and v1.0.6 pipelines (Clarke et al., 2015) for HD 168625 and MN 90, respectively. After correction for bad pixels and droop effects, the pipeline removed sky and telescope background emission by first subtracting chopped image pairs and then subtracting nodded image pairs. The resulting positive images were aligned and merged. The merged images were then coadded using a robust mean.

We observed MN 90 on UT 2015 July 3 during Guest Investigator (GI) Cycle 3 using the F371 filter ($\lambda_0 = 37.1$ μm $\Delta\lambda = 3.3$ μm). The total coadded exposure time for

Table 2.1. Summary of SOFIA/FORCAST Observations of HD 168625

Filter	λ_0 (μm)	$\Delta\lambda$ (μm)	Exp. Time (s)	PSF FWHM (arcsec)
F077	7.7	0.47	30	2.5″
F111	11.1	0.95	30	2.5″
F197	19.7	5.5	16	2.7″
F253	25.3	1.86	25	3.0″
F315	31.5	5.7	25	3.1″
F336	33.6	1.9	31	3.1″
F348	34.8	3.8	30	3.4″
F371	37.1	3.3	26	3.5″

the observation of MN 90 was 1553 sec (25.9 min). Observations of the asteroid Vesta provided the PSF, with a near-diffraction-limited FWHM at 37.1 μm of 3.6″.

We observed HD 168625 on UT 2014 June 13 during Guest Investigator (GI) Cycle 2 using eight different filters which are summarized in Table 2.1. Observations of Beta Andromedae provided the PSF.

2.2.1 Spectral Energy Distributions

We present the IR spectral energy distributions (SEDs) of MN 90 and HD 168625 in Figure 2.1 and Figure 2.2, respectively. To supplement our newly acquired SOFIA/FORCAST photometry, we also gathered archival data from the NASA/IPAC Infrared Science Archive (IRSA; Berriman, 2008) database. These include photometry from the Two Micron All-Sky Survey (2MASS; Skrutskie et al., 2006) at 1.25, 1.65, and 2.17 μm, the *AKARI* satellite (Murakami et al., 2007) at 9 and 18 μm, the *Wide-field Infrared Survey Explorer* (*WISE*; Wright et al., 2010) at 3.4, 4.6, 12 and 22 μm, the *Midcourse Space Experiment* (*MSX*; Egan et al., 2003) at 8.3, 12.1, 14.7, and 21.3 μm the *Spitzer* MIPS at 24 μm, and the *Spitzer* Infrared Array Camera (IRAC) Galactic Legacy Infrared Midplane Survey Extraordinaire I (GLIMPSE I; Benjamin et al., 2003; Churchwell et al., 2009) program at 3.6, 4.5, 5.8, and 8 μm. Photometry from our SOFIA/FORCAST images and the *Herschel* (Pilbratt, 2003) Photoconductor Array Camera and Spectrometer (PACS; Poglitsch et al., 2010) at 70, 100, and 160 μm were obtained by using

aperture photometry after sky background subtraction. Note that in the longer wavelength *Herschel* PACS/SPIRE images of MN 90 from $160 - 500$ μm the dust shell is no longer distinguishable above bright diffuse background emission. For HD 168625 we further include the *Infrared Astronomical Satellite* (*IRAS*; Neugebauer et al., 1984) Low Resolution Spectrometer (LRS) spectra from Volk & Cohen (1989).

We model the dust shell flux as equilibrium thermal emission from dust grains all at a single radius r_d from the star. We assume the grains' emissivity behaves as a power law with $Q_{abs} \propto \lambda^{-\beta}$. We adopt a power-law index of $\beta = 1.0$, which is a typical value for the circumstellar dust of evolved stars (e.g., Knapp et al. (1993)). For MN 90, a least-squares fit of a $\lambda B_\lambda(T)$ curve modified with this emissivity yields $T_d = 69 \pm 3$ K, with the peak of the emission at $\lambda = 42$ μm. For HD 168625, a least-squares fit of a $\lambda B_\lambda(T)$ curve modified with this emissivity $Q_{abs} \propto \lambda^{-1}$ yields $T_d = 160 \pm 7$ K, with the peak of the emission at $\lambda = 18$ μm.

2.2.2 MN 90

Our FORCAST 37.1 μm image of MN 90 is shown in Figure 2.3. The nebula is clearly resolved, with a radius of $\sim 30''$. It is nearly circular, with brightened limbs slightly enhanced towards the southeast. The appearance is consistent with previously obtained images at 24, 37.1 and 70 μm. Based on its appearance we will analyze the nebula as a thin, hollow shell whose far-IR spectrum is due to equilibrium thermal emission from dust grains all at the same distance from the star. This type of shell can result, for example, when a post-red supergiant (post-RSG) star has developed a fast wind during an LBV phase which sweeps up gas and dust lost during the previous RSG phase (Smith, 2014).

2.2.3 HD 168625

The FORCAST images of HD 168625 are shown in Figure 2.4. The nebula is clearly resolved, with a partially complete ring structure that has two peaks almost symmetric around the star. We concur with Meixner et al. (1999); O'Hara et al. (2003) in their interpretation of these two peaks as limb-brightened peaks of a torus of dust with a radius of $\sim 15''$. The appearance is consistent with previously obtained images at 8.8,

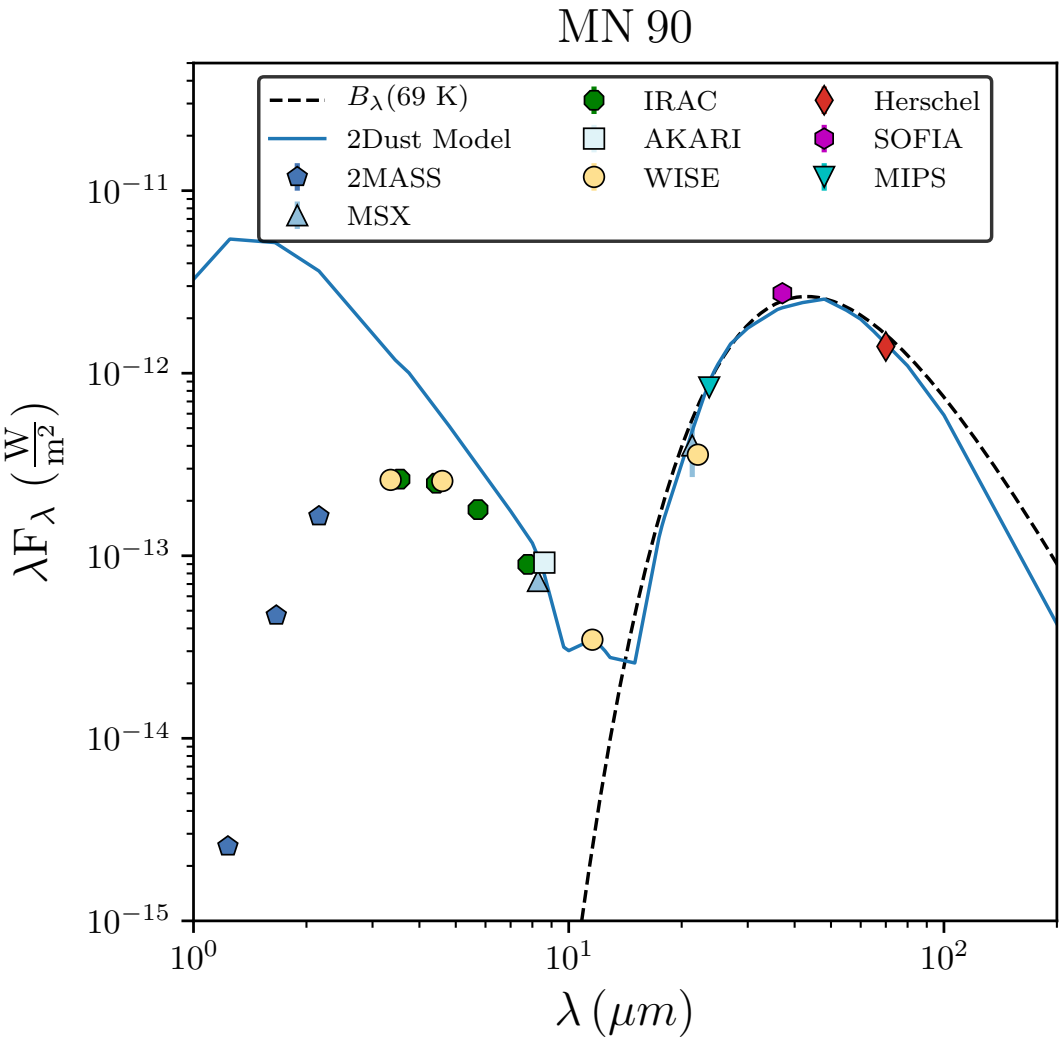

Figure 2.1 – Observed and model SEDs of MN 90. The reddened model SED is shown as a solid blue line. The dashed lines are the best fitting $Q_{abs}(\lambda) \cdot \lambda B_\lambda(T_d)$ functions with an assumed power law emissivity $Q_{abs}(\lambda) \propto \lambda^{-1}$, which yields $T_d = 69 \pm 3$ K with the peak of the emission at $\lambda = 42$ μm. Photometry data points are from this work (SOFIA) and archival databases.

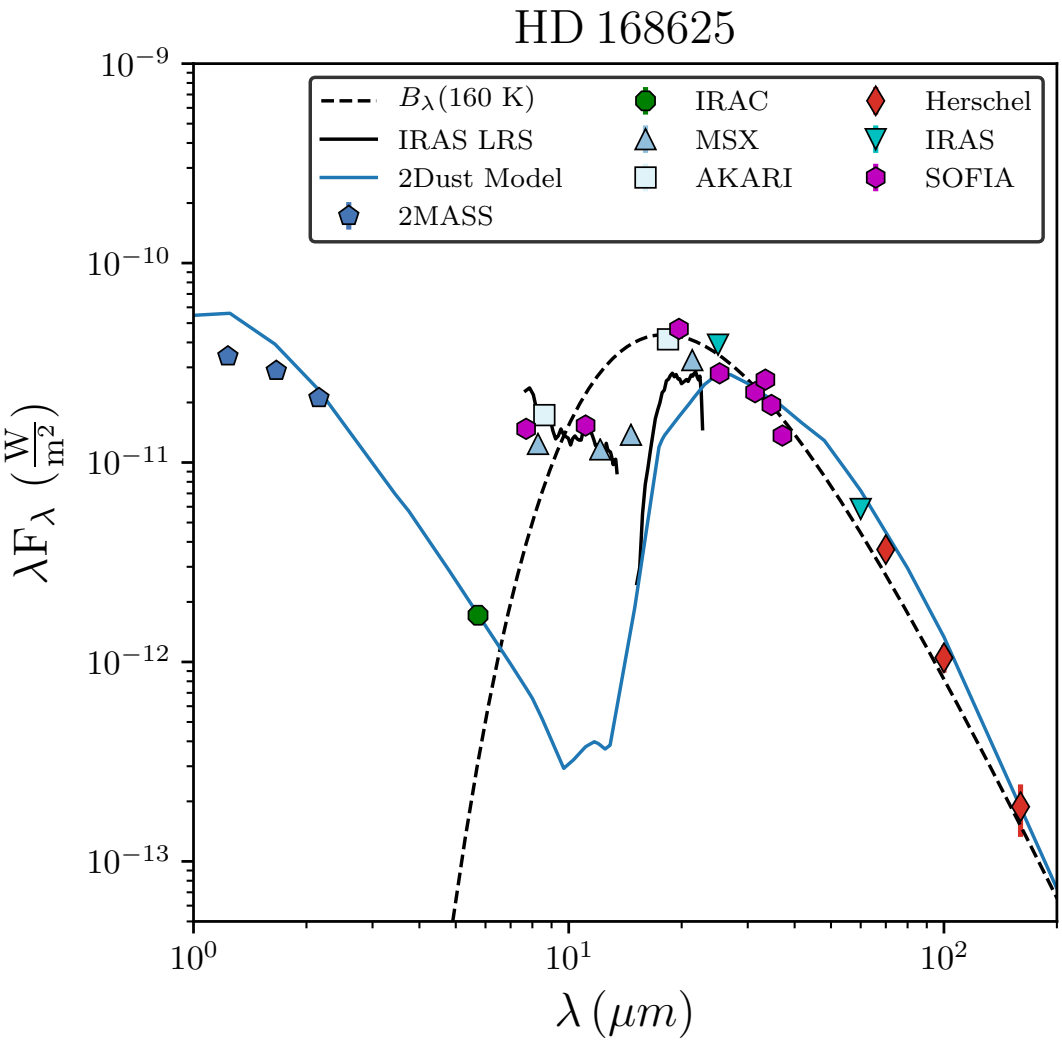

Figure 2.2 – Observed and model SEDs of HD 168625. The reddened model SED is shown as a solid blue line. The solid black line is the *IRAS* LRS (Volk & Cohen, 1989). The dashed line is the best fitting $Q_{abs}(\lambda) \cdot \lambda B_\lambda(T_d)$ function with an assumed power law emissivity $Q_{abs}(\lambda) \propto \lambda^{-1}$, which yields $T_d = 160 \pm 7$ K with the peak of the emission at $\lambda = 18$ μm. Photometry data points are from this work (SOFIA), and archival databases.

12.5, and 20.6 μm from Meixner et al. (1999) and PACS 70 μm images (Groenewegen et al., 2011). It is important to mention, that our SOFIA/FORCAST images do not detect the outer polar rings seen in *Spitzer* IRAC images (Smith, 2007), suggesting the rings must be cold. Figure 2.5 shows the temperature and optical depth maps that are derived from the SOFIA/FORCAST 11.1 and 34.8 μm images by following the method described by Dayal et al. (1998). Our temperature map estimates torus temperatures of $\sim$ 165, which is in agreement with the estimate of 160 K obtained from our least-squares fit to the IR excess but is slightly higher than the equilibrium temperature estimates made by Pasquali et al. (2002, 113 K), Robberto & Herbst (1998, 135 K) and O'Hara et al. (2003, 130 K). The map predicts optical depths between 8×10^{-5} and 3×10^{-4}, about a factor of ten lower than our model predicts, but in line with the results of O'Hara et al. (2003). This indicates that the nebula is optically thin and the east and west emission peaks coincide with the regions in which the optical depth is high, confirming the interpretation that we are observing the limb-brightened edges of an optically thin edge-on dust torus surrounding the central star.

2.2.4 IR Reddening

The mid-IR photometry (5 – 40 μm) must be de-reddened for comparison with the **2-D**ust model SED outputs, or conversely, the **2-D**ust SEDs must be reddened, as we have done. We used the Fritz et al. (2011) extinction law as it utilizes the most recent near-IR (1 – 2.4 μm) observations of the galactic center. We extend the law longward of 24 μm by adopting the Draine (2003) interstellar extinction curve defined in Figure 10 of that paper, as was done by Lau et al. (2013). We scaled the $A_{K_s}$of the Fritz et al. (2011) extinction law based on the distance to the objects. We accomplished this by utilizing the 3-D Milky Way dust map of Green et al. (2015) to estimate the extinction. We then converted from extinction to reddening by assuming $A_{K_s} = 0.320 \times \mathrm{E(B-V)}$, as calculated by Yuan et al. (2013) for a 7000 K source spectrum at $\mathrm{E(B-V)} = 0.4$ mag, using the Cardelli et al. (1989) reddening law and assuming $\mathrm{R_V} = 3.1$.

As previously mention in Section 2.1, the distance to MN 90 is unknown. In the absence of further information about the star beyond the catalogued $1.2 - 8$ μm photometry, we consider the implications of assuming that MN 90 is an LBV. We assume a

luminosity of $L_\star = 3 \times 10^5\ L_\odot$, at the lower end of luminosities for LBVs in their quiescent state between outbursts (see e.g. Figure 1 of Smith et al., 2004). This luminosity corresponds to $T_\star \approx 14000$ K. For dust grains with emissivity $Q_{abs}(\lambda) \propto \lambda^{-\beta}$, the radius r_d of the shell may be computed with:

$$r_d^2 = \frac{L_\star}{16\pi\sigma T_d^4} \left(\frac{T_\star}{T_d}\right)^\beta \tag{2.1}$$

where T_d is the grains' equilibrium temperature. Substituting the assumed values for the star and the fitted $T_d = 69$ K obtained using $\beta = 1.0$ yields $r_d = 0.6$ pc. For the shell's observed angular radius of $30''$ this places MN 90 at a distance of 4.2 kpc. At this distance we estimate a reddening of $A_{K_s} = 0.52$ for MN 90.

The distance to HD 168625 is also not well known. Hutsemekers et al. (1994) and Nota et al. (1996) assumed HD 168625 had a distance of 2.2 kpc, the same distance as the neighboring Omega Nebula (M17). Robberto & Herbst (1998) used infrared (IR) observations and estimates of stellar parameters to obtain a distance of 1.2 kpc. Whereas, a kinematic distance of 2.8 kpc was derived by Pasquali et al. (2002). HD 168625 is only $1'$ away from the LBV HD 168607. Both are found in the outskirts of the star-forming region M17, and are thought to be part of the larger Ser OB1 association at $\sim$ 2.2 kpc (Chentsov & Gorda, 2004). The *Gaia* DR1 distance to HD 168607 is 0.98 ± 0.27 kpc or 1.16 ± 0.35 kpc using the ABJ parallaxes (Smith & Stassun, 2017). Given its association with HD 168607, we adopt a distance of 1.2 kpc for HD 168625. We estimate a reddening of $A_{K_s} = 0.27$ for HD 168625. Note that any visual wavelength values are subject to considerable uncertainty, as Fritz et al. (2011) points out that there are several possible extrapolations from their anchor region around Brackett-γ (2.166 μm) into the visual.

2.3 Radiative Transfer Modeling

2.3.1 2-Dust Introduction

We utilize the the axisymmetric radiative transfer code **2-D**ust (Ueta & Meixner, 2003) to estimate the stellar parameters and dust shell morphology of MN 90 and HD 168625. The code solves the equation of radiative transfer following the principle of long characteristic (i.e. traces the radiation hitting the dust grain from anywhere in the shell

including the star and other dust radiation) in a 2-D polar grid, while considering a 3-D radiation field at each grid point. The dust opacities are calculated using Mie theory from a user-given size distribution and optical constants of the dust grains. It can be used to model a variety of axisymmetric astronomical dust systems. The dust distribution is expressed analytically as

$$\begin{aligned}\rho(r,\theta) \;=\; & \rho_{min}\Big(\frac{r}{r_{min}}\Big)^{-B\left(1+C\sin^F\theta\{\exp[-(r/r_{sw})^D]/\exp[-(r_{min}/r_{sw})^D]\}\right)} \\ & \times\big[1+A(1-\cos\theta)^F \\ & \times\{\exp[-(r/r_{sw})^E]/\exp[-(r_{min}/r_{sw})^E]\}\big]\end{aligned} \tag{2.2}$$

where r is the radius within the limits of r_{min} and r_{max}, r_{sw} is the boundary between the spherical AGB wind and the axisymmetric superwind, θ is the latitude, and ρ_{min} is the dust mass density on the equatorial axis at the inner edge of the envelope. The letters $A-F$ are input parameters that define the profle. We used a Mathis et al. (1977) power law grain size distribution:

$$n(a) = a^{-3.5} \quad , \quad a_{min} < a < a_{max} \tag{2.3}$$

where a_{min} is the minimum grain size and a_{max} is the maximum grain sized, as specified by inputs. A more extensive discussion of the geometric parameters given in Equation (2) is given in Ueta & Meixner (2003). For more examples of the use of **2-D**ust, see Ueta et al. (2001a,b); Meixner et al. (2002); O'Hara et al. (2003); Meixner et al. (2004).

2.3.2 Input Parameters

O'Hara et al. (2003) previously analyzed the morphology and parameters for the circumstellar dust around HD 168625 using **2-D**ust, therefore, we adopt most of their parameters.

Previous mid-IR spectra of HD 168625 by Skinner (1997) indicate the presence of silicates in the dust shell of HD 168625 and previous studies of the dust shells surrounding the LBVs Wra 751 and AG Car indicate that amorphous silicates are the dominant species (Voors et al., 2000). Therefore, we only considered a single amorphous silicate species, ($MgFeSiO_4$; Dorschner et al., 1995), in our dust distribution model. Because **2-D**ust cannot account for transiently heated very small dust grains or polycyclic aromatic

hydrocarbon (PAH) emission, which has been observed in previous observations(Volk & Cohen, 1989; Skinner, 1997; Umana et al., 2010), we ignore fitting the **2-D**ust model to the 8 – 15 μm region. There is also evidence of crystalline forsterite grains being present (Blommaert et al., 2014), which may contribute to the emission at $\sim$ 11 and 19 μm seen in the *IRAS* LRS.

Most estimates of the effective temperature of the central star of HD 168625 are between 12000 – 15000 K (Nota et al., 1996; O'Hara et al., 2003; Mahy et al., 2016), and may vary by a few thousand degrees. The temperature and radius of the star have been adjusted to roughly match the observed SED. However, since the data points are taken by many observers over several decades, we cannot model HD 168625 at any single epoch. The inner radius of the dust shell is well constrained by these mid-IR images to be 8.5$''$ or 0.05 pc at a distance of 1.2 kpc.

As previously mentioned, little is know about MN90 and the central star. We use the SOFIA/FORCAST 37.1 μm image to constrain the angular size of r_{min} to a value of 20$''$ or 0.41 pc at a distance of 4.2 kpc. We started with a stellar temperature of 14000 K and radius 100 $R_{\odot}$. Like HD 168625, the temperature and radius of the star have been adjusted to roughly match the observed SED and we used a single species dust distribution of amorphous silicates.

2.3.3 Model Results

We ran 150 models to obtain the best fit to the SED and SOFIA/FORCAST images of both stars. The best fit SEDs of MN 90 and HD 168625 are shown in Figures 2.1 and 2.2. Input dust distribution parameters for both stars are given in Table 2.2. Derived stellar and dust parameters for the best fit models of MN 90 and HD 168625 are given in Tables 2.3 and 2.4.

The model SED for MN 90 fits the data well in the wavelength region $\lambda \geq 8$ μm. The discrepancy at shorter wavelengths may be due to the choice of the anchor region for the reddening as discussed in Section 2.2.4, an underestimate in the distance, or incorrect stellar parameters. Our model image of MN 90 compares well with the FORCAST 37.1 μm image except for the northwest edge of the shell which appears brighter in the FORCAST image suggesting that the shell is slightly asymmetric. However, the morphology of the dust shell is well modeled as a symmetric sphere. We found the best

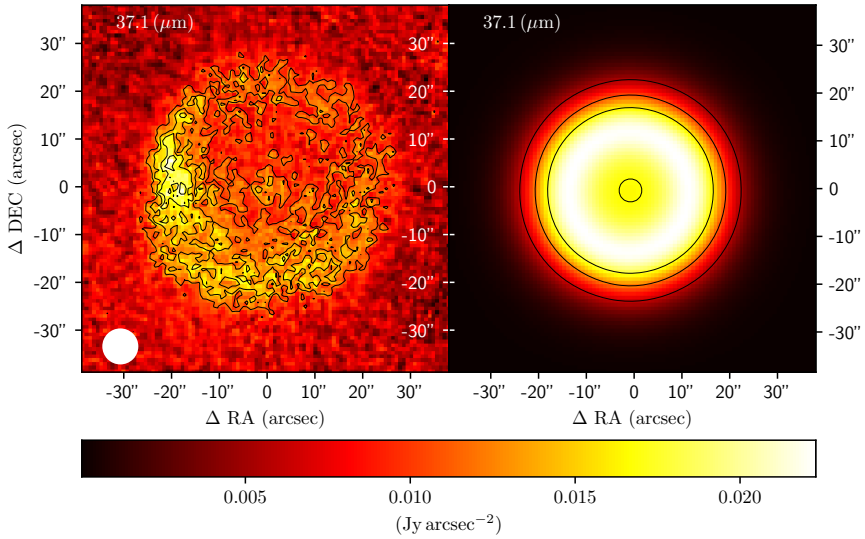

Figure 2.3 – Observed SOFIA/FORCAST image (left) and **2-D**ust model image (right) of MN 90 at 37.1 μm with north up and east to the left. The models have been scaled to the same total flux as the observed image and convolved with a Gaussian with FWHM equal to the matching PSF of the SOFIA/FORCAST image (inset white circle). In the observed SOFIA/FORCAST image, the contours are spaced at 1σ, 2σ, and 3σ intervals above the background noise. In the **2-D**ust model, the contours are space at 20% intervals of the peak intensity. The central star is not included in the model.

Table 2.2. **2-D**ust Density Function Parameters for the Best-Fit Models

Parameter	MN 90	HD 168625
A	1	31
B	2	2
C	2.5	4
D	0	6
E	0	3
F	0	4
θ_{inc}	0°	55°
$\tau_{37.1\mu\mathrm{m}}$ at eq.	6×10^{-4}	5×10^{-3}

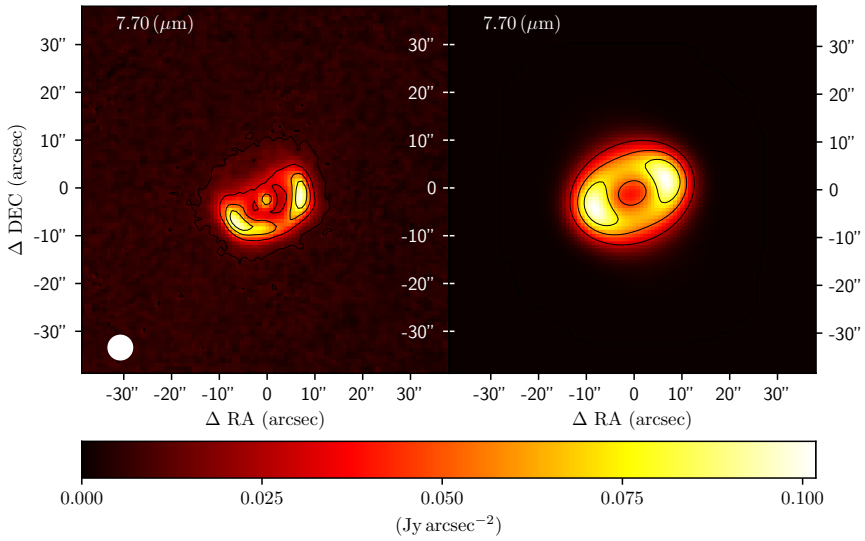

(a) FORCAST F077

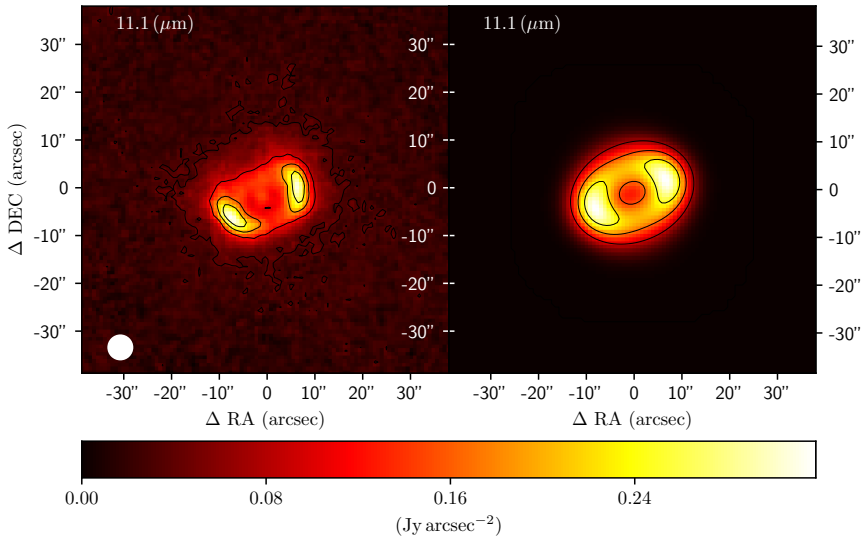

(b) FORCAST F111

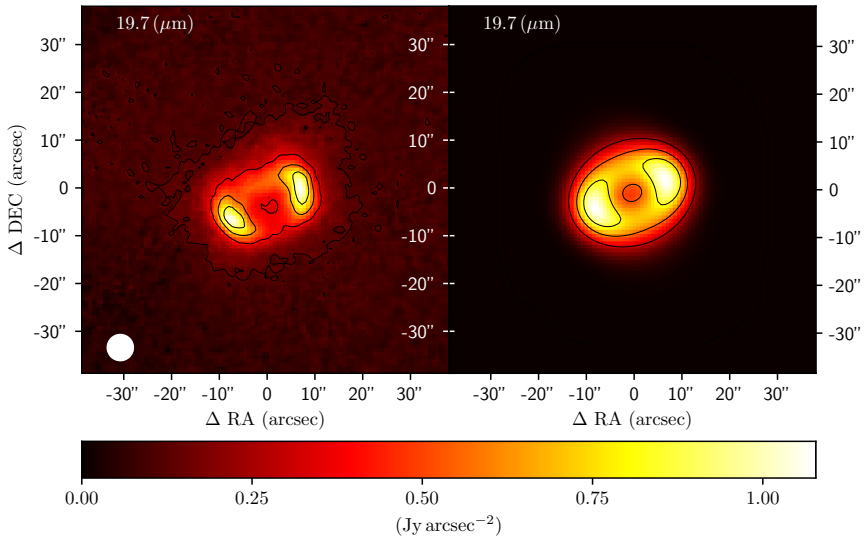

(c) FORCAST F197

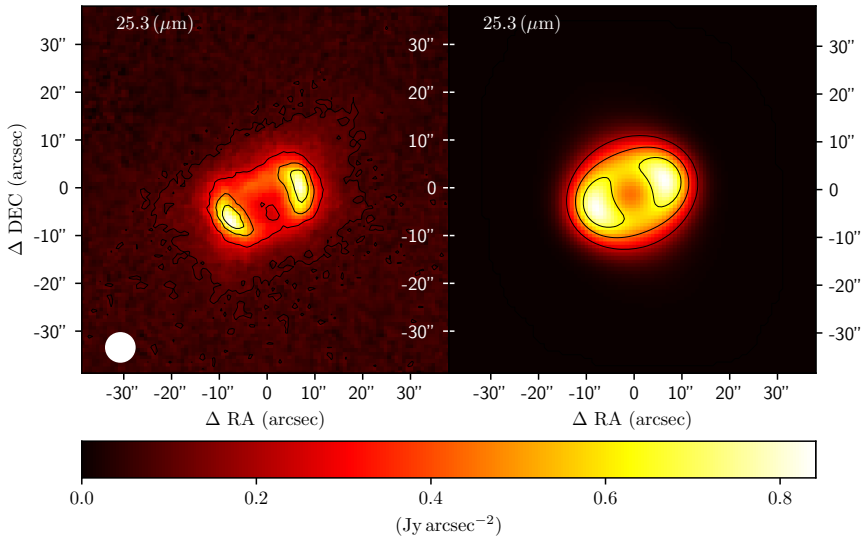

(d) FORCAST F253

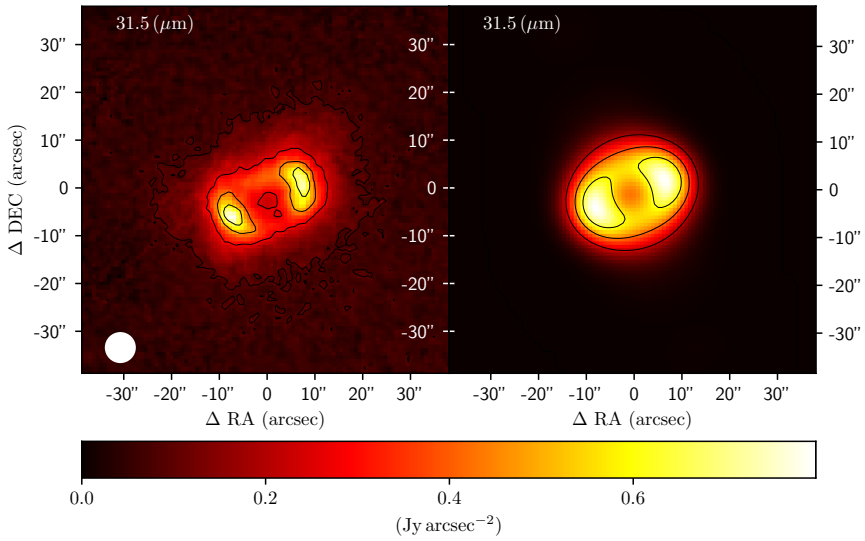

(e) FORCAST F315

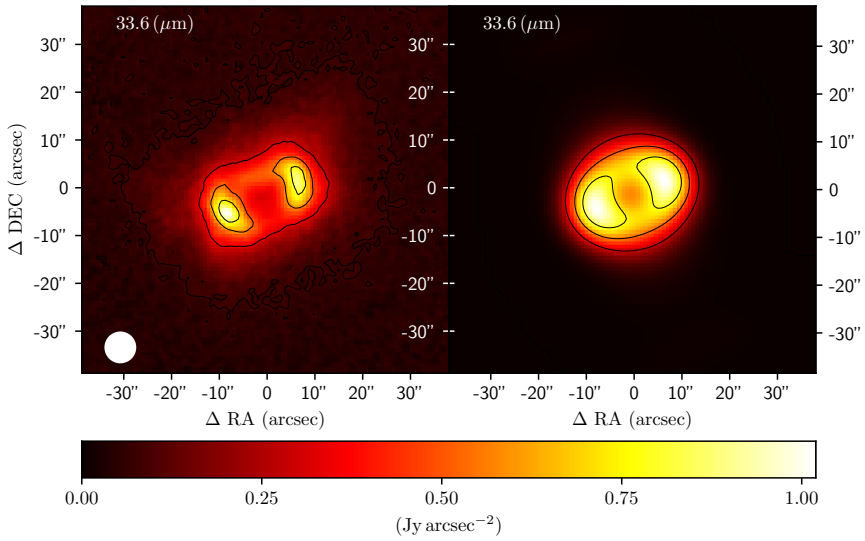

(f) FORCAST F336

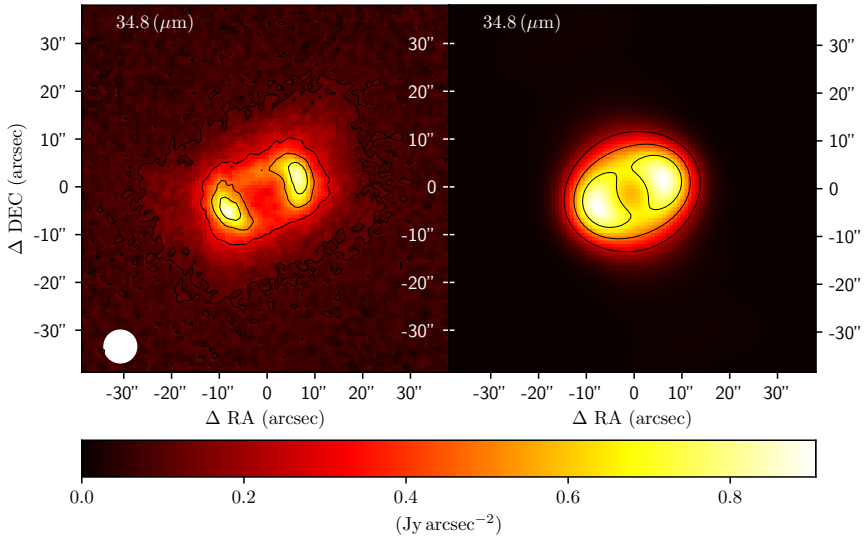

(g) FORCAST F348

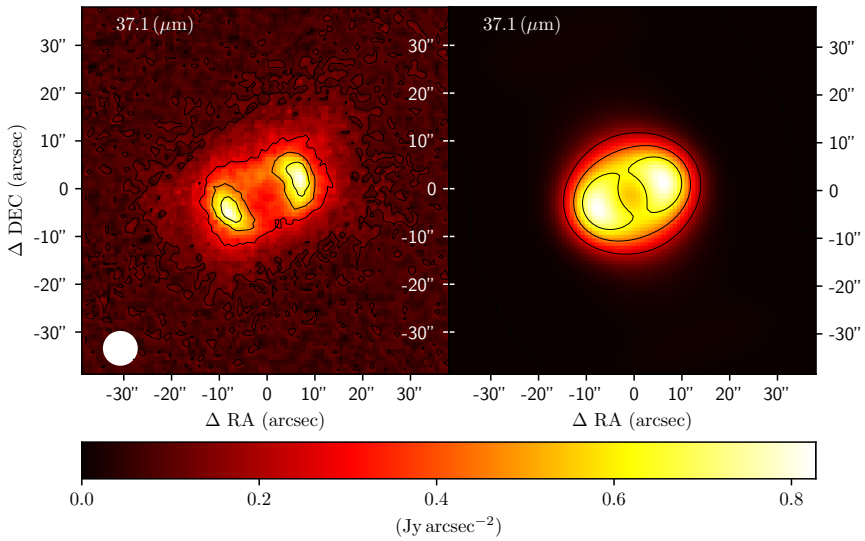

(h) FORCAST F371

Figure 2.4 – Observed SOFIA/FORCAST image (left) and **2-D**ust model image (right) of HD 168625 at (a) 7.7 μm, (b) 11.1 μm, (c) 19.7 μm, (d) 25.3 μm, (e) 31.5 μm, (f) 33.6 μm, (g) 34.8 μm, and (h) 37.1 μm with north up and east is to the left. The models have been scaled to the same total flux as the observed image and convolved with a Gaussian with FWHM equal to the matching PSF of the SOFIA/FORCAST image (inset white circle). In the observed SOFIA/FORCAST images, the contours are spaced at 1σ, 2σ, and 3σ intervals above the background noise. In the **2-D**ust model, the contours are space at 20% intervals of the peak intensity. The central star is not included in the model.

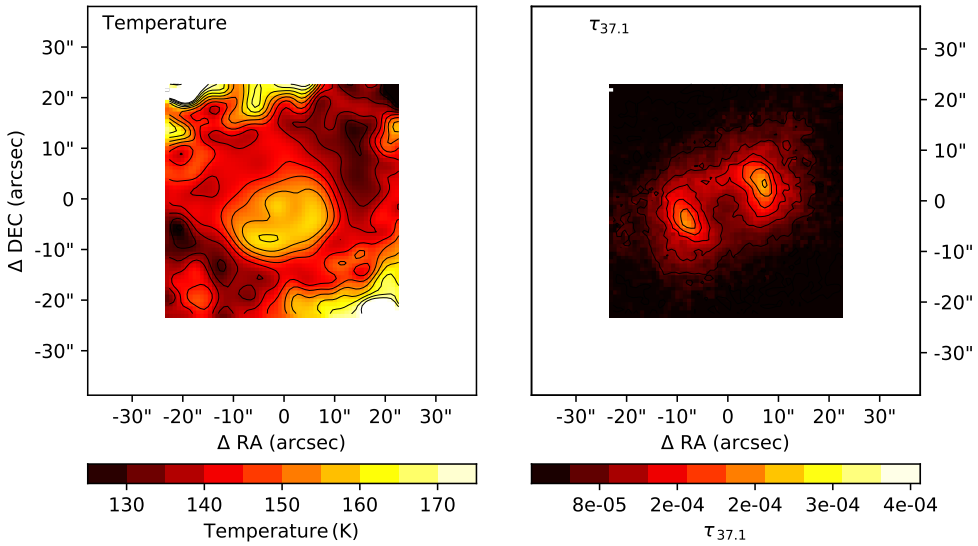

Figure 2.5 – Temperature map (left) and optical depth map at 37.1 μm (right) of HD 168625. Temperature contours go from 125 to 175 K with an interval of 5 K. The optical depth map has contours from 2×10^{-5} to 4×10^{-4} at intervals of 4×10^{-5}. In both images, spurious data around the edges have been removed.

fit density distribution had an amorphous silicate shell extending from $r_{min} = 0.31$ pc to $3r_{min} = 0.92$ pc. The grain size distribution suggests that the silicates had grain sizes between 0.1 – 0.5 μm. Our model gives a dust mass of 2.5×10^{-2} $M_{\odot}$ and a dust mass-loss rate of 8.3×10^{-6} $M_{\odot}\, yr^{-1}$.

The model SED for HD 168625 fits the data well in most of the wavelength range except for 8 – 15 μm for the reasons mentioned in Section 2.3.2. We confirm the dust distribution model of O'Hara et al. (2003) with only minor differences in the stellar temperature, radius and grain size distribution. The morphology of the dust is found to be a disk-like shell with an equator-to-pole density ratio of 31, an elliptical midshell, and an inclination angle of 55° with the plane of the sky. Our model images compare well with the FORCAST observations except for the gap in the northern rim of the 7.7 μm emission and the gap in the southern rim of the 19.7, 25.3, 31.5, and 33.6 μm, emission which may indicate the lack of large dust grains in this region or a different composition. This supports the suggestion that the dust shell may include small, transiently heated dust grains that are not at thermal equilibrium and are not accounted for in these

Table 2.3. MN 90 **2-D**ust Input and Derived Parameters

Input	
$L_* \propto d$	$7.1 \times 10^4\ L_\odot$
T_*	14000 K
$R_* \propto d$	85 $R_\odot$
d	4.2 kpc
ISM A_{K_s}	0.52
$r_{min} \propto d$	0.31 pc
$r_{max} \propto d$	0.92 pc
$r_{sw} \propto d$	0.46 pc
a_{min}	0.1 μm
a_{max}	0.5 μm
v_{exp}[a]	50 km s^{-1}
Composition	Amorphous Silicates[b]
Derived	
$M_{dust} \propto d^2$	$2.5 \times 10^{-2}\ M_\odot$
$\dot{M}_{dust} \propto d^2$	$8.3 \times 10^{-6}\ M_\odot\, yr^{-1}$
τ_{AGB}[c] $\propto d$	$3.4 \times 10^3\ yr$

[a]Typical for LBVs (Nota et al., 1995)

[b]$MgFeSiO_4$ (Dorschner et al., 1995)

[c]Timescale for mass-loss on the AGB

models. The grain size distribution suggests that grain sizes between 0.001 – 0.5 μm exist in the circumstellar environment. Our model gives a dust mass of 2.4×10^{-3} $M_{\odot}$and a dust mass-loss rate of 1.3×10^{-7} $M_{\odot}\, yr^{-1}$. This is likely an underestimate the mass because we are only looking at material in the equator, $\sim$ 10 – 20% of the solid angle of the entire nebula. The bipolar nebula seen in *Spitzer* images suggests that the circumstellar material at higher latitudes was ejected with higher speed, and therefore it is farther from the star and cooler, which went undetected in the SOFIA imaging that only detects the inner torus. The model suggests that HD 168625 lost mass in a torus-shaped outburst, which has been suggested for all LBVs by Hutsemekers et al. (1994). The current fast wind of the LBV has probably interacted with this torus, creating an elliptical bubble perpendicular to the plane of the torus, which is consistent with a unified model of LBV nebulae proposed by Nota et al. (1995).

2.4 Discussion

As previously mentioned in Section 2.3.2, crystalline forsterite has been detected around HD 168625. This indicates that at least some of the circumstellar material, probably that confined to the torus, has undergone annealing and suggests that the circumstellar environment is similar to that of lower mass progenitors i.e. proto-planetary nebulae (PPNe). We should point out that our model for HD 168625 included moderately sized grains (0.1 – 0.5 μm) as did the model found by O'Hara et al. (2003, 0.001 – 1.0 μm) which points to the nebula being relatively young and unprocessed. Aside from the similarities in morphology between PPN and LBVs, a key difference may be the duration of mass-loss. Far-IR images at 55 μm of HD 168625 by O'Hara et al. (2003) suggests that the outer dust shell is no more than 5 times the inner radius. Whereas, for the Egg Nebula, a well-studied PPN, 180 μm images suggest that the outer shell is a few hundred times larger than the inner radius (Speck et al., 2000). The mass-loss shells of LBVs appear to be more compressed than for PPNs, suggesting that the mass-loss occurred in a more short-lived ($< 10^4$ yr) phase compared with PPNs ($\sim 10^5$ yr).

Table 2.4. HD 168625 **2-D**ust Input and Derived Parameters

Input	
$L_* \propto d$	$2.5 \times 10^4\ L_\odot$
T_*	12000 K
$R_* \propto d$	$60\ R_\odot$
d	1.2 kpc
ISM A_{K_s}	0.27
$r_{min} \propto d$	0.05 pc
$r_{max} \propto d$	0.26 pc
$r_{sw} \propto d$	0.15 pc
a_{min}	0.001 μm
a_{max}	0.5 μm
v_{exp}[a]	19 km s^{-1}
Composition	Amorphous Silicates[b]
Derived	
$M_{dust} \propto d^2$	$2.4 \times 10^{-3}\ M_\odot$
$\dot{M}_{dust} \propto d^2$	$1.3 \times 10^{-7}\ M_\odot\, yr^{-1}$
τ_{AGB}[c] $\propto d$	$7.6 \times 10^3\ yr$

[a]Pasquali et al. (2002)

[b]$MgFeSiO_4$ (Dorschner et al., 1995)

[c]Timescale for mass-loss on the AGB

2.4.1 HD 168625

Mahy et al. (2016) used *Herschel*/PACS spectroscopy and CNO abundances to estimate an initial mass of 28 – 33 $M_{\odot}$ for HD 168625 and propose that the star lost its mass during or just after the blue supergiant (BSG) phase and has not yet reached the red supergiant (RSG) phase. Furthermore, they found that single star evolutionary tracks were able to explain the N content between the nebula and the central star. This depends on the assumption that the star is a single star, whereas Smith & Tombleson (2015) argue that LBVs may be the product of binary evolution. As mentioned in Section 2.1, a wide-orbit binary companion to HD 168625 has been observed, but the influence this companion has on the evolution and morphology of HD 168625 is negligible. Given that no X-ray emission has been observed (Nazé et al., 2012) rules out mass transfer via Roche lobe overflow. The rotation rate of HD 168625 is estimated to be 53 $\mathrm{km\,s^{-1}}$ (Taylor et al., 2014) which is not high enough to explain the bipolar structure based on rotation or binary merger. Furthermore, no companion has been detected in radial velocity monitoring.

If we use the canonical gas-to-dust ratio of 100 we estimate a total (gas plus dust) shell mass-loss rate of 1.4×10^{-5} $M_{\odot}\,yr^{-1}$ and a total mass of 0.24 $M_{\odot}$. This is likely an underestimate of the mass because we are only looking at material in the equatorial torus. Dividing our value for $r_{min} = 0.05$ pc by the nebular expansion velocity measured by Pasquali et al. (2002) gives an expansion time of $\simeq 2600$ yr, and using our value of $r_{max} = 0.26$ pc, the mass-loss lasted for $\simeq 1 \times 10^4$ yr. As noted in Table 2.4, the **2-D**ust estimates for the dust mass and mass-loss rate are proportional to the distance squared and given the uncertainty in the distance to HD 168625 the values we have estimated in this work should be interpreted with appropriate caution.

2.4.2 MN 90

The morphology of MN 90 lacks a large equator-to-pole mass distribution like most LBVs and is nearly spherical, similar to V4998 Sgr (Lau et al., 2014). The total mass (gas plus dust) lost by the star and the rate of mass-loss are estimated to be about 2.5 $M_{\odot}$ and 8.4×10^{-4} $M_{\odot}\,yr^{-1}$ using the canonical gas-to-dust ratio of 100. Dividing our value for $r_{min} = 0.31$ pc by an assumed expansion velocity of 50 $\mathrm{km\,s^{-1}}$ gives an

estimated expansion time of $\simeq$ 6000 yr and using our value of r_{max} = 0.92 pc, we estimate the mass-loss lasted for $\simeq 1.2 \times 10^4$ yr. As noted in Table 2.3, the **2-D**ust estimates for the dust mass and mass-loss rate are proportional to the distance squared and given the distance to MN 90 is unknown the values we have estimated in this work should be interpreted as hypothetical.

Based on the mid-IR morphology and results from radiative transfer calculations, MN 90 is a very luminous star surrounded by an optically thin possibly oxygen rich dust shell located at about 4.2 kpc. However, given the uncertainties in the distance and stellar parameters, no strong conclusions about the nature of MN 90 can be made. It is necessary to observationally uncover the physical characteristics of the central star to determine the exact evolutionary status of MN 90. Because MN 90 is not visible in the optical due to heavy extinction, near-IR spectroscopic information is needed to constrain the physical parameters for the central star. Furthermore, continuous near-IR photometry to better characterize the variability of the source would be useful. Regardless of the exact evolutionary status, MN 90 seems highly likely to be an evolved, massive post-main sequence star.

2.5 Conclusion

Our SOFIA/FORCAST images between 7.7 – 37.1 μm of HD 168625 compliment previously obtained mid-IR imaging. The dust color temperature and optical depth maps that we derive from our observations show evidence for the limb-brightened peaks of an equatorial torus and for very small, transiently heated dust grains. A least-squares fit of a $\lambda B_\lambda(T_d)$ curve with emissivity $Q_{abs}(\lambda) \propto \lambda^{-1}$ to the SED of HD 168625 yields an estimated dust temperature of 160 ± 7 K, with the peak of the emission at 18 μm. Our detailed radiative transfer model using **2-D**ust supports the claim that the dust resides in a thin, axisymmetric dust shell and estimates that HD 168625 lost 2.4×10^{-3} $M_\odot$ of dust in a massive stellar wind with a mass-loss rate of 1.3×10^{-7} $M_\odot\, yr^{-1}$ that ended approximately 2600 years ago. Using a canonical gas-to-dust ratio of 100 we estimate a total mass-loss of 0.24 $M_\odot$ for HD 168625 which is a lower limit given we are only observing the inner equatorial torus, $\sim$ 10 – 20% of the solid angle of the entire nebula. These **2-D**ust estimates assume that HD 168625 has a luminosity of 2.5×10^4 $L_\odot$, at

the lower end of luminosities of LBVs in their quiescent state, and a distance of 1.2 kpc.

Our SOFIA/FORCAST image at 37.1 μm of MN 90 shows a limb-brightened, spherical dust shell surrounding the central star. A least-squares fit of a $\lambda B_\lambda(T_d)$ curve with emissivity $Q_{abs}(\lambda) \propto \lambda^{-1}$ to the SED of MN 90 yields a dust temperature of 69 ± 3 K, with the peak of the emission at 42 μm. Our **2-D**ust model supports the idea that the dust resides in a thin, spherical dust shell and estimates that MN 90 lost 2.5×10^{-2} $M_\odot$ of dust in a massive stellar wind with a mass-loss rate of 8.3×10^{-6} $M_\odot\, yr^{-1}$ that ended approximately 6000 years ago. These **2-D**ust estimates assume that MN 90 has a luminosity of 7.1×10^4 $L_\odot$, at the lower end of luminosities of LBVs in their quiescent state, and a distance of 4.2 kpc. Using the canonical gas-to-dust mass ratio of 100, we estimate a total mass-loss of 2.5 $M_\odot$ for MN 90. Our **2-D**ust model of MN 90 has good agreement with observations if we assume very small, transiently heated silicate grains.

With a more direct and reliable measurement of the distances to MN 90 and HD 168625, more accurate dust mass and mass-loss rates could be estimated. The uncertainty in the distance to MN 90 and the limited information regarding its physical parameters make it a prime candidate for follow-up observations and photometric monitoring.

Chapter 3

A SOFIA/FORCAST Grism Study of the Mineralogy of Dust in the Winds of Proto-planetary Nebulae: RV Tauri Stars and SRd Variables

This chapter has been published in the Astrophysical Journal with the following bibiliographic reference: Arneson, R. A., Gehrz, R. D., Woodward, C. E., et al. 2017, ApJ, 843, 51

Abstract

We present a SOFIA/FORCAST grism spectroscopic survey to examine the mineralogy of the circumstellar dust in a sample of post-asymptotic giant branch yellow supergiants that are believed to be the precursors of planetary nebulae. Our mineralogical model of each star indicates the presence of both carbon rich and oxygen rich dust species–contrary to simple dredge-up models–with a majority of the dust in the form of amorphous carbon and

graphite. The oxygen rich dust is primarily in the form of amorphous silicates. The spectra do not exhibit any prominent crystalline silicate emission features. For most of the systems, our analysis suggests that the grains are relatively large and have undergone significant processing, supporting the hypothesis that the dust is confined to a Keplerian disk and that we are viewing the heavily processed, central regions of the disk from a nearly face-on orientation. These results help to determine the physical properties of the post-AGB circumstellar environment and to constrain models of post-AGB mass loss and planetary nebula formation.

3.1 Introduction

RV Tauri and yellow semi-regular (SRd) variables are two classes of post-asymptotic giant branch (post-AGB) stars that lie along the horizontal track on the Hertzsprung-Russell (H-R) diagram linking AGB stars to planetary nebulae (PNe). They are thought to be the immediate precursors of PNe and have been termed "proto-planetary nebulae" (PPNe)[1] . RV Tauri stars are characterized by semi-regular, bimodal variability (possibly resulting from interaction with a binary companion; Waelkens & Waters, 1993; Percy, 1993; Fokin, 1994), a high mass-loss rate, and often a prominent infrared (IR) excess. SRd variables are similar to RV Tauri stars in many respects but are probably single star systems, as indicated by the absence of regular pulsations (Percy & Ursprung, 2006).

RV Tauri stars are a loosely defined subclass of Population II Cepheid variables named after the prototype RV Tau. They are defined as luminous (I-II) mid-F to K supergiants with a typical mass of ~ 0.7 $M_{\odot}$ (Tuchman et al., 1993; Fokin, 1994) that show alternating deep and shallow minima in their light curves (Preston et al., 1963). They have formal periods (defined as the time between successive deep minimia) between 30 and 150 days, but cycle-to-cycle variability is common, and the amplitudes may reach up to 4 magnitudes in V (Percy, 1993). RV Tauri stars are divided into two

[1] The phrase "proto-planetary" is also widely used by the exoplanetary and planet formation communities to refer to dusty disks around young stars. Also note that in the literature the terms preplanetary or proto-planetary nebulae have been used interchangeably with the term post-AGB objects.

photometric classes ('a' and 'b') based on their light curves (Kukarkin, 1958). The RVa class contains constant mean magnitude stars, and the RVb class contains stars that have a varying mean magnitude with a period of 600 to 1500 days. There are several possible explanations for these light variations. One explanation for the alternating minima is that there is a resonance between the fundamental period and the first overtone (Takeuti & Petersen, 1983; Shenton et al., 1992; Tuchman et al., 1993; Fokin, 1994). Another possibility is that the light variations are due to a geometrical projection effect where the pulsating star is periodically obscured by a circumbinary disk (Van Winckel et al., 1999; Maas et al., 2002).

Preston et al. (1963) classified the RV Tauri stars into three spectroscopic classes ('A', 'B', 'C'). RVA stars are spectral type G – K, and show strong absorption lines and normal CN or CH bands while TiO bands sometimes appear at photometric minima. RVB stars are generally hotter spectral types, weaker lined, and show enhanced CN and CH bands. RVC stars are also weak lined but show normal CN and CH molecular bands. There is no correlation between the photometric and spectroscopic classes.

It has long been known (Gehrz & Woolf, 1970; Gehrz, 1972; Gehrz & Ney, 1972) that some RV Tauri stars (e.g. AC Her, U Mon, R Sct, R Sge) show very strong thermal IR emission from circumstellar dust. Observations by the *Infrared Astronomical Satellite* (*IRAS*) confirmed these previous detections and increased the sample size. *IRAS* detected considerable cool, circumstellar dust around many of the RV Tauri stars, which has been interpreted as being due to strong, dusty mass-loss during AGB evolution (Jura, 1986). From CO observations, Alcolea & Bujarrabal (1991) suggest a mass loss rate of 4×10^{-7} to 7×10^{-6} $M_{\odot}yr^{-1}$ within the last 10^2 to 10^3 years for most of the RV Tauri stars. Because of their position on the H-R diagram, variability, high mass-loss rate and rarity (about 110 are known), it is generally believed that RV Tauri stars represent a relatively short-term, unstable transitional phase between the AGB and PNe phases of solar-mass stars. If RV Tauri stars are assumed to be evolving on the post-AGB track, models predict that they spend about 200 years as variables and take about 1000 years to go from AGB to PNe (Schoenberner, 1983; Percy et al., 1991; Fokin, 1994), however some (e.g. R Sct) are "lazy", spend more time in the RV Tauri stage as evidenced by their mass loss history, have higher CO emission, and show a relatively low IR excess in the 5 – 20 μm range but a larger IR excess for $\lambda \gtrsim 50$

μm (Bujarrabal et al., 1988; Alcolea & Bujarrabal, 1991). The lack of a near-IR excess and the presence of a large mid- and far-IR excess is evidence for a thick and extended dust envelope that is relatively cool. The detection of SiO around R Sct could be an indication of on-going, weak mass loss (Bujarrabal et al., 1989). Alcolea & Bujarrabal (1991) estimate that $\sim 1/5$ RV Tauri stars exhibit this "lazy" evolutionary behavior.

Interestingly, RV Tauri stars do not have the same high C and s-process overabundances that are characteristic of other post-AGB stars. Instead, their photospheres are "depleted" of refractory elements (Gonzalez et al., 1997b,a; Giridhar et al., 1998, 2000, 2005; Van Winckel et al., 1998; Molster et al., 2002a,b,c; Maas et al., 2002, 2005; Deroo et al., 2005; Gielen et al., 2007, 2009; Rao & Giridhar, 2014). This phenomenon is not fully understood, but is apparently due to a chemical rather than a nucleosynthetic process (van Winckel, 2003). The refractory elements, which have a high dust condensation temperature, are separated from the volatiles as the condensed grains are driven away by radiation pressure in the circumstellar environment. The depleted gas is then re-accreted onto the stellar photosphere leaving it with a peculiar composition similar to that of the depleted gas in the interstellar medium (ISM) (Hinkle et al., 2007). Waters et al. (1992) suggested that these abundance anomalies are more likely to occur when the dust is trapped in a circumstellar disk. These same depletion patterns are also observed in binary post-AGB stars with circumbinary disks (Van Winckel et al., 1995). This has led to the suggestion that the depleted RV Tauri stars are also binaries with a circumstellar disk (Van Winckel et al., 1999). In their study, de Ruyter et al. (2006) included many RV Tauri stars in the class of post-AGB binaries with disks and suggested that the thermal IR spectrum originates in the Keplerian circumstellar disk. The narrow velocity width lines of the ^{12}CO and ^{13}CO J $= 2 \rightarrow 1$ and J $= 1 \rightarrow 0$ transitions of AC Her, V441 Her, and R Sct and the ^{12}CO J $= 3 \rightarrow 2$ and J $= 2 \rightarrow 1$ transitions of AR Pup are indicative of a Keplerian disk (Bujarrabal et al., 2013, 2015). The trapping of grains in a disk could provide the environment needed to enable grains to grow to sizes significantly larger than those in the ISM or in the stellar outflows of single stars (Shenton et al., 1995; de Ruyter et al., 2005). The similar class of SRd stars, however, does not show evidence of disks and may evolve from single stars.

Depending on the oxygen and carbon abundances in the circumstellar gas, either oxygen- or carbon-rich dust is formed. It has been found that many of the RV Tauri

stars have very weak CO J = 2 → 1 lines, unlike the stronger CO J = 2 → 1 lines characteristic of other, more massive, post-AGB stars (Alcolea & Bujarrabal, 1991; He et al., 2014; Bujarrabal et al., 2015). It is possible that the unique circumstellar environment of RV Tauri stars either surpresses the formation of CO molecules (possibly through UV photodissociation) or underexcites them (Alcolea & Bujarrabal, 1991; McDonald et al., 2015). However, the weakness may be due to the compactness of the disk, as has been suggested for the case of AC Her (Bujarrabal et al., 2015). In oxygen-rich gas, dust such as olivine ($Mg_{2(1-x)}Fe_{2x}SiO_4$) and pyroxene ($Mg_{1-x}Fe_xSiO_3$) is formed. In carbon-rich gas, carbon rich dust particles such as SiC, amorphous carbon, and possible polycyclic aromatic hydrocarbons (PAHs) are formed.

The amount of crystalline grain material compared to amorphous grain material is generally low, $\sim 10 - 15\%$, and is dominant only in rare cases. Crystalline material is also generally only detected in stars that have experienced high mass loss rates (above $10^{-5}M_{\odot}yr^{-1}$) (Cami et al., 1998; Sylvester et al., 1999; Sogawa & Kozasa, 1999; Suh, 2002). However, both crystalline and amorphous grains have been detected simultaneously in stellar outflows, both in the present study as well as in others. Gielen et al. (2008, 2009) showed that dust processing in circumstellar disk environments is conducive to creating large, crystalline grains. As the disk is subjected to the hard radiation and stellar wind from the central source, the dust crystallization fraction increases (Gielen et al., 2011) and the disk dissipates (Kastner et al., 2004; Gezer et al., 2015; Kastner et al., 2016; Lisse et al., 2017). Thus, the IR excess associated with the dusty disk diminishes as the system ages and transitions to a PN.

In this work we present 5 – 40 μm IR spectra on a diverse sample of RV Tauri and SRd variables from a grism spectroscopic study of suspected proto-planetary nebula precursors with the Faint Object infraRed CAmera for the SOFIA Telescope (FORCAST; Herter et al., 2012) instrument on board the NASA Stratospheric Observatory for Infrared Astronomy (SOFIA; Becklin et al., 2007; Gehrz et al., 2009; Young et al., 2012). With this rich data set, we produce spectroscopic sampling of these objects in the mid-IR. By modeling the emission we can determine the source of the IR-excess, identify the dust species present and quantify fundamental dust properties, such as the grain size distribution and dust temperature. These parameters help to determine the physical properties of the post-AGB circumstellar environment and to constrain models

of post-AGB mass loss and planetary nebula formation.

In Section 3.2 we summarize the stars observed by our program. An overview of the observations and data reduction strategies is given in Section 3.3. Section 3.4 contains the construction of the spectral energy distributions and the spectral decomposition model we used to measure the mineralogy of the program stars. The results of our model, a discussion of our results and our conclusions are presented in Sections 3.5 – 3.7.

3.2 Program Stars

We have selected a sample of RV Tauri and related SRd stars based upon: 1) their availability for SOFIA flights from Palmdale, CA and Christchurch, NZ, 2) diversity of their IR spectral energy distributions (SEDs), 3) our ability to obtain a signal-to-noise ratio compatible with our science objectives in a reasonable integration time.

The properties of the 18 RV Tauri and SRd variables presented in this work are summarized in Table 3.2. TX Per is sometimes categorized as an RV Tauri star and sometimes as an SRd variable. We concur with Percy & Coffey (2005), which refers to TX Per as being a "mild" RV Tauri as the consecutive minima are very similar in depth, and categorize TX Per as an RV Tauri variable.

The mineralogy of many of these systems has been studied previously (Molster et al., 2002c; Deroo et al., 2006; Gielen et al., 2007, 2011; Blommaert et al., 2014; Hillen et al., 2015). These studies have mostly focused on crystalline silicates. Most of the studies found evidence for large, crystalline dust grains indicative of highly processed material. Some of the studies suggest that the crystalline and amorphous silicates are at different temperatures suggesting that the two species are spatially separated and have different formation histories.

3.3 Observations and Data Reduction

The targets were observed with SOFIA during Guest Investigator (GI) Cycles 2, 3, and 4. Descriptions of the SOFIA Observatory and its science instrument (SI) suite have been given by Becklin et al. (2007), Gehrz et al. (2009), and Young et al. (2012). All of

Table 3.1. Properties of the RV Tauri and SRd Variables in this Survey

Name	Type	Spectral Type	Period (d)[a]	$[Fe/H]_0$[b]	PC[c]	SC[c]	SED[d]	T_{eff} (K)	Binarity[e]	Chemical Type[f]	Ref.
TW Cam	RV	F8IbG8Ib	87	-0.40	a	A	Disk	4800			1
UY CMa	RV	G0	114	-0.50	a	B		5500			2
o[1] Cen	SRd	G3Ia0	200								3
RU Cen	RV	A7IbG2pe	65	-1.10	a	B	Disk	6000	Y		4, 5
SX Cen	RV	F5G3/5Vp	33	-0.30	b	B	Disk	6250	Y		4, 5
SU Gem	RV	F5M3	50	0.00	b	A	Disk	5250			6
AC Her	RV	F2pIbK4e	75	-0.90	a	B	Disk	5900	Y	O	7
V441 Her	SRd	F2Ibe	70				Disk		Y	O	8, 9
U Mon	RV	F8IbeK0pIb	91	-0.50	b	A	Disk	5000	Y	O	1, 10
CT Ori	RV	F9	136	-0.60	a	B	Disk	5500			10, 11
TV Per	SRd	K0	358								12
TX Per	RV	Gp(M2)K0e(M2)	78	-0.60	a	A		4250			6
AR Pup	RV	F0IF8I	76	0.40	b	B	Disk	6000		O	10, 13
R Sge	RV	G0IbG8Ib	71	0.10	b	A	Disk	5100			13
AI Sco	RV	G0K2	71	-0.30	b	A	Disk	5300		C?	2, 10
R Sct	RV	G0IaeK2p(M3)Ibe	147	-0.20	a	A	Uncertain	4500			1
RV Tau	RV	G2IaeM2Ia	79	-0.40	b	A	Disk	4500		C	1
V Vul	RV	G4eK3(M2)	76	0.10	a	A	Disk	4500			2, 6

[a]Pulsation period in days

[b]The estimated initial metallicity obtained via the Zn or S abundance (Gezer et al., 2015)

[c]Photometric class (PC) and spectroscopic class (SC)

[d]Spectral energy distribution classification from Gezer et al. (2015)

[e]Y indicates confirmed binarity based on radial velocity measurements. Confirming binarity using this method is difficult because the photospheres of these variables have large amplitude radial pulsations.

[f]Stellar chemical type from He et al. (2014) and references therein

References. — (1) Giridhar et al. (2000); (2) Giridhar et al. (2005); (3) O'Connell (1961); (4) Maas et al. (2002); (5) Maas et al. (2005); (6) Rao & Giridhar (2014): (7) Giridhar et al. (1998); (8) Waters et al. (1993); (9) de Ruyter et al. (2006); (10) Kiss et al. (2007); (11) Gonzalez et al. (1997a); (12) Payne-Gaposchkin (1952); (13) Gonzalez et al. (1997b)

the targets in our survey were observed using FORCAST.

FORCAST is a dual-channel mid-IR camera and spectrograph operating between 5 – 40 μm. Each channel consists of a 256 $\times$ 256 pixel array that yields a $3.4' \times 3.2'$ field-of-view with a square plate scale of $0.768''$, after distortion correction. The Short Wave Camera (SWC) uses a Si:As blocked-impurity band (BIB) array optimized for $\lambda < 25$ μm, while the Long Wave Camera's (LWC) Si:Sb BIB array is optmized for $\lambda > 25$ μm. Observations can be made through either of the two channels individually or, by use of a dichroic mirror, with both channels simultaneously across the entire range. All of the observations presented in this work were taken in the single channel, long-slit mode. We utilized FORCAST's suite of grisms, which provided low spectral resolution (R $\approx$ 200) over the 5 – 40 μm range. The following grisms were used for our observations: G1 covering 4.9 – 8.0 μm, G3 covering 8.4 – 13.7 μm, G5 covering 17.6 – 27.7 μm, and G6 covering 28.7 – 37.1 μm. All of the observations were taken in the "nod match chop" mode (C2N) which used a chop throw of $30''$, a chop angle of either 0° or 30°, and no dithering.

The data were reduced by the SOFIA Science Center using FORCAST Redux v1.5.0 and v1.2.0 pipeline versions (Clarke et al., 2015) and released to the authors as level 3 results. We stacked the spectra when there were multiple observations of a given target. We did not use any of the data points between 9.19 – 10.0 μm as these are strongly affected by telluric ozone absorption. The spectra were smoothed with a 3 point un-weighted boxcar to emphasize spectral features.

3.4 Spectral Energy Distributions of the Survey Objects

We present the IR SEDs of the survey objects in Figure 3.1. As can be seen in Figure 3.2, all of the program stars except for TX Per were observed with the G1, G3, and G5 grisms, and only 7 of the 18 stars were also observed with the G6 grism. TX Per was fainter than expected and we were only able to obtain the G1 grism spectrum (4.9 – 8.0 μm). We were unable to model the spectral energy distribution of TX Per with such a limited wavelength range. The continuum normalized SOFIA grism spectra are shown in Figure 3.2. We have also gathered archival broadband IR photometry for comparison with the SOFIA spectra. Photometry from the Two Micron All-Sky Survey (2MASS;

Skrutskie et al., 2006) at 1.25, 1.65, and 2.17 μm, the *AKARI* satellite (Murakami et al., 2007) at 9 and 18 μm, the *Wide-field Infrared Survey Explorer* (*WISE*; Wright et al., 2010) at 3.4, 4.6, 12 and 22 μm, the *Midcourse Space Experiment* (*MSX*; Egan et al., 2003) at 8.28, 12.13, 14.65, 21.34 μm, and the *Infrared Astronomical Satellite* (*IRAS*; Neugebauer et al., 1984) at 12, 25, 60, and 100 μm were all taken from the NASA/IPAC Infrared Science Archive (IRSA; Berriman, 2008) database. Photometry from the *Herschel* (Pilbratt, 2003) Photoconductor Array Camera and Spectrometer (PACS; Poglitsch et al., 2010) at 70, 100, and 160 μm and Spectral and Photometric Imaging Receiver (SPIRE; Griffin et al., 2010) at 250, 350, and 500 μm were obtained by using aperture photometry after sky background subtraction. The archival photometry data points were *not* used in any of the least squares fitting routines and are only plotted to visualize the SED of each star.

3.4.1 Dust Species

Previous studies have shown that the most common dust species present in circumstellar environments are amorphous and crystalline silicates with olivine and pyroxene stoichiometries (Molster et al., 2002a,b,c; Gielen et al., 2011). Amorphous olivine has very prominent broad features around 9.8 and 18 μm. These features arise from the Si-O stretching and O-Si-O bending modes. Amorphous pyroxene shows a 10 μm feature similar to that of amorphous olivine, but shifted towards shorter wavelengths. Crystalline forsterite has prominent emission features at 11.2, 23.7, and 33.7 μm. Many of the stars in our sample are known to be oxygen rich (see Table 3.2) however an increased abundance of carbon dredged up as the star evolves is possible (Iben, 1981; Chan & Kwok, 1990). Models suggest that stars with main sequence masses less than 1.5 $M_{\odot}$ do not experience third dredge-up. Therefore, the surface composition of these stars is fixed by the first dredge-up and red giant branch extra-mixing, and they are oxygen rich AGB stars. For main sequence stars with masses over 6 $M_{\odot}$ the stars undergo shallow third dredge-up episodes. Stars in the intermediate main sequence mass range undergo repeated third dredge-up episodes that bring carbon to the surface to become carbon stars (for a review see Straniero et al. 2006; Karakas & Lattanzio 2014). The interpulse time for the third dredge-up is a few times 10^4 years with carbon stars undergoing several pulses after the carbon abundance first exceeds the oxygen abundance (Straniero

et al., 1997). The interpulse time exceeds the expansion time for circumstellar shells and as expected nearly all normal AGB stars have shells of the same composition as the star. Carbon rich AGB stars are expected to have circumstellar shells dominated by amorphous carbon or graphite grains with some silicon carbide (SiC) possibly present (Suh, 2000; Speck et al., 2005, 2009). Amorphous carbon does not have prominent IR features but contributes to the dust continuum emission, however, graphitic carbon and silicon carbide have emission features at 11.53 μm and in the 10 – 13 μm region, respectively. The strong depletion of iron in the photospheres of RV Tauri stars suggests that metallic iron may be present in the circumstellar environment. Iron grains can form at temperatures 50 – 100 K lower than silicates and are stable in O-rich environments above 700 K (Kemper et al., 2002). Like amorphous carbon, metallic iron lacks prominent IR features and contributes to the overall dust continuum. Therefore, the dust species we included in our model are crystalline forsterite, amorphous olivine, amorphous pyroxene, amorphous carbon, silicon carbide, graphite, and metallic iron. We only considered the magnesium-rich crystalline species of olivine (forsterite) as it has been found that the iron content of circumstellar crystalline olivine around evolved stars is lower than 10% (Tielens et al., 1998; Molster et al., 2002c). In addition, we only included amorphous enstatite and pyroxene with an iron content of 0% as these species were found to be better fits to the spectra than the same species with an iron content of 50%. We tried including Mg-righ crystalline olivine, Mg-rich crystalline enstatite, crystalline bronzite, crystalline fayalite, iron oxide, amorphous alumina, and amorphous silica in our model, however none of these dust species were significantly present. We discuss the addition of some of these species more in Section 3.6.4.

Mass absorption coefficients for the different dust species are calculated from optical constants using a homogeneous sphere approximation (Min et al., 2005). Although the continuous distribution of ellipsoids approximation (CDE; Bohren & Huffman, 1983) is widely used, it is only valid in the Rayleigh limit for small grain sizes. Because we are interested in the grain size distribution we did not use the CDE approximation. The details of the different optical constants that we used can be found in Table 3.2. In cases where the refractive index was reported for the three crystallographic directions, we assumed even distributions of each orientation. There are many laboratory

Table 3.2 Dust Species and Properties Used in this Work

Dust Species	Composition	Structure	Density (g/cm^3)	Grain Size (μm)	Reference
Forsterite	Mg_2SiO_4	C	3.27	0.1	Koike et al. (2003)
Olivine	Mg_2SiO_4	A	3.71	0.1, 2.0	Dorschner et al. (1995)
Pyroxene	$MgSiO_3$	A	3.20	0.1, 2.0	Dorschner et al. (1995)
Carbon	Pyrolized at 400° C	A	1.435	0.1, 2.0	Jaeger et al. (1998b)
Silicon Carbide	α-SiC	C	3.26	0.1, 2.0	Pegourie (1988)
Graphite		C	2.24	0.1, 2.0	Draine & Lee (1984)
Metallic Iron	Fe	C	7.87	0.1, 2.0	Pollack et al. (1994)

Note. – The mineral structure is denoted as either amorphous (A) or crystalline (C).

measurements of IR optical constants available, corresponding to different material compositions, crystal structures, annealing temperatures, measurement environments, grain sizes, and grain orientations. These different measurements produce spectra with similar global features but with unique differences. While the minerals we have chosen to use in our model may result in different relative abundances compared to those derived in previous studies, we are less concerned with making comparisons with those works and more concerned with drawing comparisons between the program stars in the present study.

3.4.2 Spectral Decomposition Model

To identify the minerals present and to quantify the grain size distributions, we fit the observed SOFIA spectra with synthetic spectra of various mineral species. The synthetic spectra were calculated from the optical constants of each mineral. The conversion from laboratory measured optical constants of dust to mass absorption coefficients is not straightforward. Several factors affect the observed emission features, including the chemical composition of the dust, the grain size, and the grain shape (Min et al., 2003, 2005). We constructed a basic model to fit the full FORCAST wavelength range. Given that we see the silicate features in emission, we assume that the dust features are in an optically thin part of the disk and, therefore, we approximate the spectrum as a linear combination of dust absorption profiles. The emission model is given by

$$\lambda F_\lambda \propto \sum_i c_i \mu_i(\lambda) \times \sum_j a_j \lambda B_\lambda(T_j), \tag{3.1}$$

where $\mu_i(\lambda)(\mathrm{cm}^{-1})$ is the absorption coefficient of dust component i and c_i gives the volume fraction of that dust component, $B_\lambda(T_j)$ $(\mathrm{W\,sr^{-1}\,m^{-3}})$ denotes the Planck function at temperature T_j and a_j is the scaling factor for the j^{th} Planck function. The absorption coefficient is related to the mass absorption coefficient (opacity) by $\mu = \kappa\rho$ where $\kappa\,(\mathrm{cm^2\,g^{-1}})$ is the mass absorption coefficient (opacity) and $\rho\,(\mathrm{g\,cm^{-3}})$ is the density of the dust component. The formulation of our model assumes that the stellar contribution to the SED in this range is negligible. We further assume that all of the dust in a population is in thermal equilibrium with all of the other dust species, regardless of particle sizes or the ability to absorb and re-emit starlight. We first used a least squares minimization to fit the Planck functions to the FORCAST continuum. We fit the functions to the entire FORCAST wavelength range available except for the $8-12.5$ μm range, which is dominated by silicate emission. Two Planck functions were used for all of the spectral models except for o[1] Cen and V Vul where only a single Planck function was needed to fit the underlying continuum. The best fitting Planck function parameters are shown in Figure 3.1 and summarized in Table 3.3, however, the sum of the Planck scaling factors, a_j, have been normalized to unity in order to represent the fraction of dust at each temperature T_j. The best fitting Planck functions are plotted with the FORCAST spectra in Figure 3.1. It is probably not realistic to model the dust as a single temperature component or even as a two-temperature component–a temperature gradient is probably more realistic–but in order to keep the number of parameters at a minimum we only use a maximum of two Planck functions in our model.

After finding the best fitting Planck functions, the best fitting dust fraction coefficients, c_i, were found by a non-negative least squares minimization of the model to the entire observed FORCAST wavelength range. The reduced χ^2 of the spectrum is given by

$$\chi^2_{\mathrm{red}} = \frac{1}{N-M}\sum_{i=1}^{N}\left|\frac{F_{\mathrm{model}}(\lambda_i)-F_{\mathrm{obs}}(\lambda_i)}{\sigma_i}\right|^2, \tag{3.2}$$

where N is the number of wavelength points, M the number of fit parameters, $F_{\mathrm{model}}(\lambda_i)$ is the model flux at a given wavelength, $F_{\mathrm{obs}}(\lambda_i)$ is the observed flux at a given wavelength, and σ_i the absolute error of the observed flux at each wavelength λ_i. The reduced χ^2 values are summarized in Table 3.3.

Errors on the dust fraction coefficients were calculated from 5000 realizations of a Monte Carlo simulation with Gaussian noise distributions. We omitted a mineral

species from the fit if the error, $\sigma_{\overline{c_i}}$, on $\overline{c_i}$ is greater than the value of $\overline{c_i}$ itself. Figure 3.4 illustrates the distributions of the best fitting dust fraction coefficients, c_i, and the covariance between the coefficients (Foreman-Mackey, 2016). Most of the coefficients show little to no correlation with the exception of the carbon, graphite, and metallic iron species which are strongly anti-correlated in most cases. Even though this model is only an approximation, it gives a good fit overall to the observed spectra (see Figure 3.3). A full radiative transfer model that could account for a temperature gradient in the disk that may produce a better fitting result is beyond the scope of this work.

3.4.3 Grain Size Distribution

To study the grain size distribution, we used two dust grain sizes in our model with radii of 0.1 and 2.0 μm. These sizes were chosen based on the work of Bouwman et al. (2001) and Honda et al. (2004) which found that, in the 10 μm spectral region, 0.1 μm grains sufficiently describe grains with $a < 1.0$ μm while 1.5 – 2.0 μm grains sufficiently describe grains with $a > 1.5$ μm. Larger sized grains were not considered as the emission features from larger grains become too weak to distinguish from the continuum emission. Because the grains with radii of 2.0 μm are in the Mie scattering regime, we used the python module *pymiecoated* (Leinonen, 2012) to calculate the mass absorption coefficients for the 2.0 μm grains. *pymiecoated* computes the scattering properties of single- and dual-layered spheres in the Mie regime using the results of Bohren & Huffman (1983) and the optical constants of bulk materials. The mass absorption coefficient for crystalline forsterite was taken directly from Koike et al. (2003). Because we did not have the optical constants for this mineral we were unable to calculate the mass absorption coefficient for larger sized grains in the Mie scattering regime.

3.5 Results

The results of the spectral decomposition modeling are shown in Figure 3.3. Details of individual sources are provided in Table 3.3. The spectroscopic features present in these sources span a broad range of dust properties and characteristics. All of the RV Tauri stars in our sample, with the exceptions of UY CMa, TX Per, and R Sct have been

reported as disk sources (Gezer et al., 2015). Two sources, o^1 Cen and V Vul display a simple blackbody continuum. However, model fits demonstrate that they both also exhibit a weak IR excess (see Figure 3.1 (c) and (r)), suggesting that these systems may be in the final stages of dissipation. The remaining RV Tauri stars all exhibit emission from carbon-rich minerals with varying degrees of amorphous and crystalline silicates.

Two of our SRd sources, V441 Her and TV Per, show prominent silicate features. The presence of these features suggests that these sources, too, may have dusty disks akin to the disks of the RV Tauri stars. Alternatively, these features might also arise from normal dusty outflows. In the case of V441 Her, the 10 μm feature is strong while the 20 μm feature is weak, as is expected for relatively fresh and unprocessed amorphous silicates (Nuth & Hecht, 1990). In contrast, TV Per exhibits strong 10 and 20 μm silicate emission, suggestive of prolonged exposure to hard radiation. We discuss this more fully in Section 3.6.

Table 3.3: RV Tauri and SRd Star Mineralogy

Star	$\chi^2_{\rm red}$	Mineral	$\overline{c_i}$	$\sigma_{\overline{c_i}}$	V_f	σ_{V_f}	T_1(K)	F_{T_1}	T_2(K)	F_{T_2}
TW Cam	0.26	Graphite-small	3.75	0.15	0.58	2.6E-2	1365 ± 105	0.019 ± 3.6E-3	332 ± 8	0.981 ± 3.6E-3
		Graphite-large	1.14	0.06	0.18	1.1E-2				
		Carbon-large	1.08	0.10	0.17	1.7E-2				
		Pyroxene-small	0.26	0.03	0.04	4.1E-3				
		SiC-small	0.20	0.04	0.03	5.7E-3				
UY CMa	0.08	Graphite-small	1.76	0.49	0.36	1.0E-1	1251 ± 201	0.010 ± 4.1E-3	337 ± 7	0.990 ± 4.1E-3
		Graphite-large	1.29	0.11	0.26	3.6E-2				
		Carbon-large	1.20	0.21	0.24	4.9E-2				
		Pyroxene-small	0.47	0.06	0.10	1.7E-2				
		Forsterite-small	0.21	0.04	0.04	8.6E-3				
o^1 Cen	0.32	Iron-small	7.01	0.48	0.49	3.8E-2	3780 ± 193	1.0	-	-
		Graphite-small	5.96	0.49	0.42	3.7E-2				
		Graphite-large	1.17	0.06	0.08	5.5E-3				
		Pyroxene-small	0.17	0.03	0.01	2.1E-3				
RU Cen	0.23	Graphite-small	3.53	0.20	0.45	2.8E-2	535 ± 16	0.010 ± 1.4E-3	203 ± 2	0.990 ± 1.4E-3
		Carbon-large	2.01	0.18	0.25	2.4E-2				
		Pyroxene-small	0.89	0.05	0.11	8.0E-3				
		Graphite-large	0.86	0.08	0.11	1.1E-2				
		SiC-small	0.50	0.06	0.06	8.3E-3				
		Forsterite-small	0.11	0.02	0.01	3.0E-3				
SX Cen	0.24	Graphite-small	2.65	0.26	0.41	4.5E-2	715 ± 14	0.042 ± 4.8E-3	244 ± 7	0.958 ± 4.8E-3
		Carbon-large	1.77	0.14	0.27	2.7E-2				
		Graphite-large	0.95	0.08	0.15	1.5E-2				
		Pyroxene-large	0.72	0.19	0.11	3.0E-2				
		Olivine-large	0.32	0.18	0.05	2.8E-2				

Continued on next page

Table 3.3 – *Continued from previous page*

Star	$\chi^2_{\rm red}$	Mineral	$\overline{c_i}$	$\sigma_{\overline{c_i}}$	$V_{\rm f}$	$\sigma_{V_{\rm f}}$	T_1(K)	F_{T_1}	T_2(K)	F_{T_2}
		Pyroxene-small	0.08	0.06	0.01	9.8E-3				
SU Gem	0.40	Graphite-small	4.06	0.12	0.59	1.9E-2	1444 ± 83	0.023 ± 3.1E-3	349 ± 5	0.977 ± 3.1E-3
		Carbon-large	1.16	0.07	0.17	1.1E-2				
		Graphite-large	1.07	0.05	0.15	7.5E-3				
		Pyroxene-small	0.38	0.02	0.06	2.9E-3				
		SiC-small	0.27	0.03	0.04	3.9E-3				
AC Her	1.43	Graphite-small	3.43	0.06	0.48	9.4E-3	489 ± 4	0.022 ± 9.4E-4	207 ± 1	0.978 ± 9.4E-4
		Carbon-large	1.51	0.05	0.21	6.6E-3				
		Graphite-large	0.92	0.02	0.13	3.6E-3				
		Pyroxene-small	0.76	0.01	0.11	2.3E-3				
		SiC-small	0.50	0.02	0.07	2.6E-3				
		Forsterite-small	0.09	0.01	0.01	9.8E-4				
V441 Her	0.15	Graphite-small	3.14	0.14	0.40	2.2E-2	1607 ± 68	0.019 ± 1.8E-3	363 ± 3	0.981 ± 1.8E-3
		Carbon-small	2.76	0.20	0.35	2.6E-2				
		Graphite-large	1.07	0.05	0.14	8.3E-3				
		Olivine-small	0.44	0.08	0.06	1.0E-2				
		Pyroxene-small	0.23	0.04	0.03	5.2E-3				
		SiC-small	0.21	0.04	0.03	5.3E-3				
U Mon	0.50	Carbon-small	3.55	0.50	0.30	6.3E-2	772 ± 10	0.020 ± 1.0E-3	254 ± 1	0.980 ± 1.0E-3
		Graphite-small	3.17	0.13	0.27	4.5E-2				
		Iron-large	2.94	1.88	0.25	1.6E-1				
		Pyroxene-small	0.87	0.06	0.07	1.3E-2				
		SiC-small	0.56	0.05	0.05	9.0E-3				
		Graphite-large	0.42	0.15	0.04	1.4E-2				
		Olivine-small	0.38	0.10	0.03	9.8E-3				
CT Ori	0.25	Graphite-small	3.91	0.17	0.53	2.5E-2	684 ± 13	0.041 ± 4.0E-3	258 ± 5	0.959 ± 4.0E-3

Continued on next page

Table 3.3 – *Continued from previous page*

Star	$\chi^2_{\rm red}$	Mineral	$\overline{c_i}$	$\sigma_{\overline{c_i}}$	$V_{\rm f}$	$\sigma_{V_{\rm f}}$	T_1(K)	F_{T_1}	T_2(K)	F_{T_2}
		Carbon-large	1.58	0.12	0.21	1.7E-2				
		Graphite-large	0.97	0.07	0.13	1.1E-2				
		Pyroxene-small	0.57	0.03	0.08	5.0E-3				
		SiC-small	0.38	0.04	0.05	5.7E-3				
TV Per	0.58	Carbon-small	3.75	0.58	0.29	6.5E-2	2340 ± 12	0.002 ± 4.0E-5	297 ± 1	0.998 ± 4.0E-5
		Iron-large	3.24	2.20	0.25	1.7E-1				
		Graphite-small	2.47	0.16	0.19	3.5E-2				
		Pyroxene-small	1.47	0.07	0.11	2.0E-2				
		Olivine-small	1.04	0.14	0.08	1.7E-2				
		SiC-small	0.87	0.07	0.07	1.3E-2				
		Graphite-large	0.30	0.17	0.02	1.4E-2				
AR Pup	1.93	Graphite-small	4.07	0.11	0.48	1.4E-2	734 ± 7	0.062 ± 3.0E-3	280 ± 3	0.938 ± 3.0E-3
		Carbon-small	2.88	0.06	0.34	8.3E-3				
		Graphite-large	1.02	0.02	0.12	2.8E-3				
		Olivine-large	0.23	0.01	0.03	1.5E-3				
		Pyroxene-small	0.19	0.01	0.02	6.9E-4				
R Sge	0.17	Graphite-small	3.66	0.54	0.43	6.8E-2	862 ± 29	0.026 ± 3.6E-3	270 ± 7	0.974 ± 3.6E-3
		Carbon-small	3.02	0.42	0.36	5.5E-2				
		Graphite-large	0.97	0.13	0.11	1.8E-2				
		Pyroxene-small	0.51	0.03	0.06	6.2E-3				
		SiC-small	0.34	0.05	0.04	6.8E-3				
AI Sco	0.32	Graphite-small	3.94	0.17	0.59	3.0E-2	1049 ± 74	0.030 ± 6.1E-3	322 ± 7	0.970 ± 6.1E-3
		Carbon-large	1.15	0.14	0.17	2.1E-2				
		Graphite-large	1.10	0.08	0.16	1.3E-2				
		Pyroxene-small	0.30	0.03	0.04	4.2E-3				
		SiC-small	0.19	0.04	0.03	6.3E-3				

Continued on next page

Table 3.3 – *Continued from previous page*

Star	$\chi^2_{\rm red}$	Mineral	$\overline{c_i}$	$\sigma_{\overline{c_i}}$	V_f	σ_{V_f}	T_1(K)	F_{T_1}	T_2(K)	F_{T_2}
R Sct	1.18	Graphite-small	5.42	0.23	0.70	3.1E-2	1857 ± 44	0.017 ± 7.0E-3	158 ± 18	0.983 ± 7.0E-3
		Graphite-large	1.10	0.05	0.14	8.0E-3				
		Carbon-large	1.04	0.07	0.13	1.0E-2				
		Pyroxene-small	0.23	0.02	0.03	2.2E-3				
RV Tau	0.26	Graphite-small	3.70	0.13	0.43	1.9E-2	760 ± 10	0.052 ± 2.9E-3	256 ± 3	0.948 ± 2.9E-3
		Carbon-small	3.21	0.21	0.37	2.5E-2				
		Graphite-large	0.92	0.06	0.11	7.1E-3				
		Pyroxene-small	0.47	0.03	0.05	3.3E-3				
		SiC-small	0.38	0.03	0.04	3.9E-3				
V Vul	0.36	Iron-small	8.06	0.55	0.55	4.1E-2	678 ± 4	1.0	-	-
		Graphite-small	4.92	0.41	0.34	3.1E-2				
		Graphite-large	1.05	0.05	0.07	5.0E-3				
		Pyroxene-large	0.31	0.07	0.02	4.9E-3				
		SiC-large	0.16	0.06	0.01	4.4E-3				
		Pyroxene-small	0.10	0.05	0.01	3.3E-3				

Note. – $\overline{c_i}$ is the average best fit coefficient of a given mineral species. $\sigma_{\overline{c_i}}$ is the standard deviation of the average best fit coefficient, V_f is the volume fraction, $\sigma(V_f)$ is the error in the volume fraction, $T_{1,2}$ are the blackbody dust temperatures, and $F_{T_{1,2}}$ is the fraction of dust at those temperatures, respectively. 'small' refers to 0.1 μm spherical grains, 'large' designates 2.0 μm spherical grains.

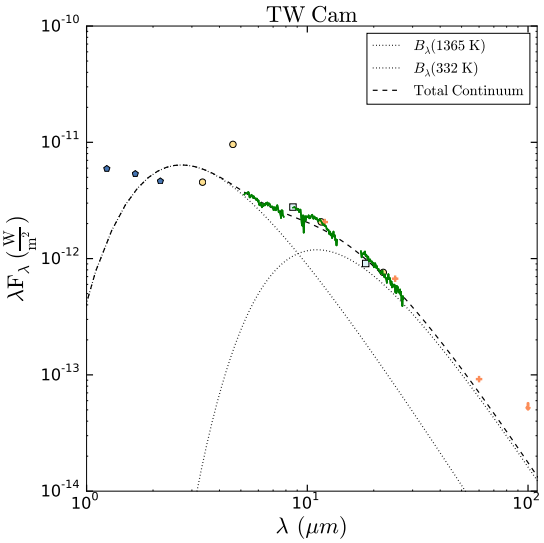

(a) TW Cam

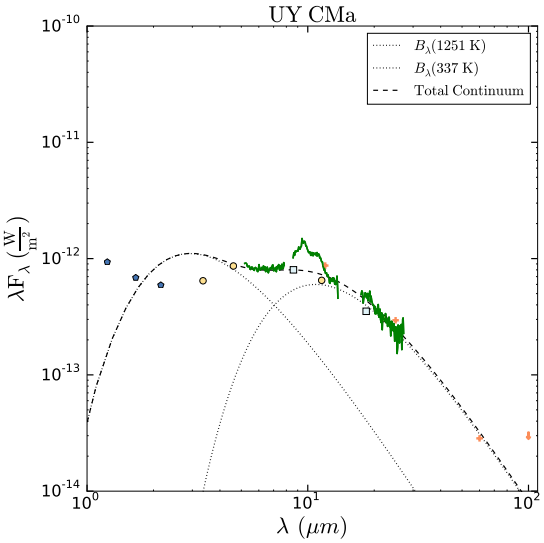

(b) UY CMa

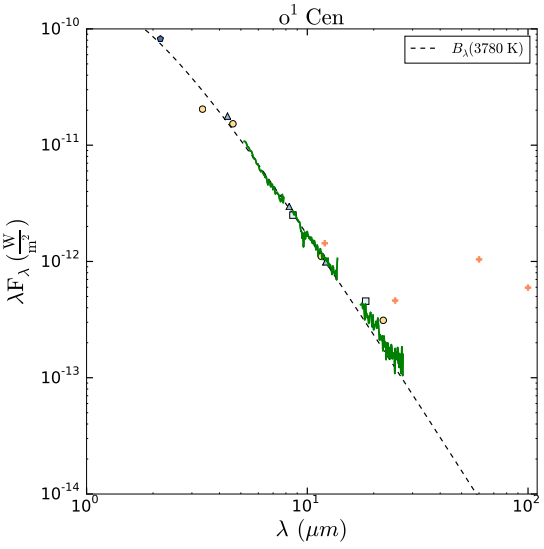

(c) o^1 Cen

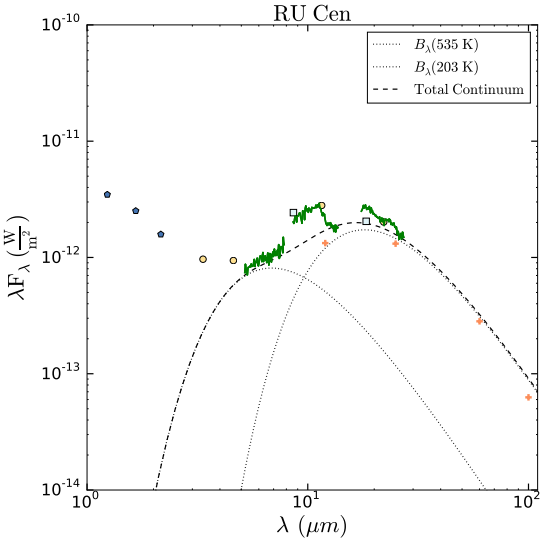

(d) RU Cen

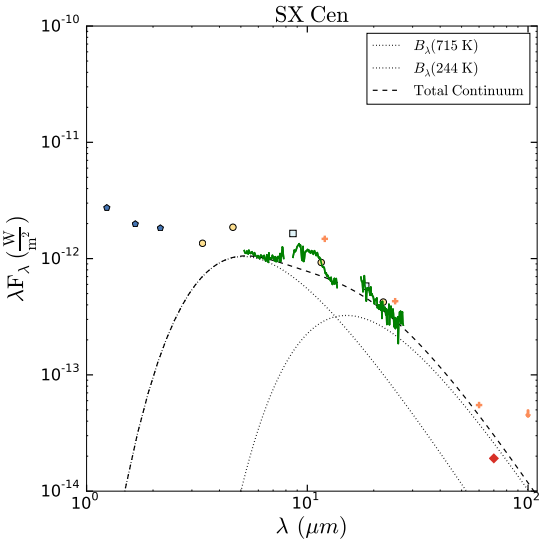

(e) SX Cen

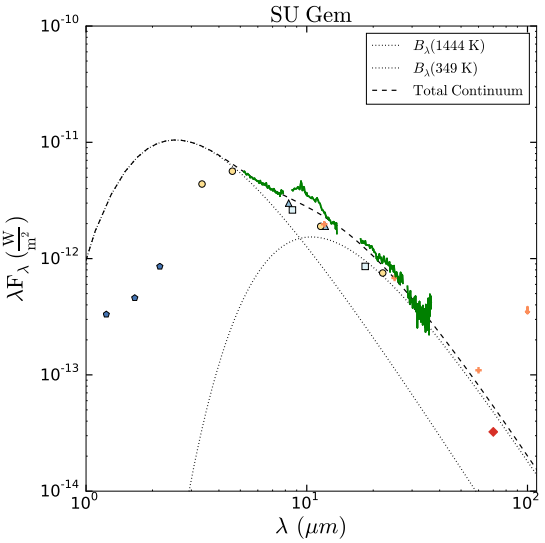

(f) SU Gem

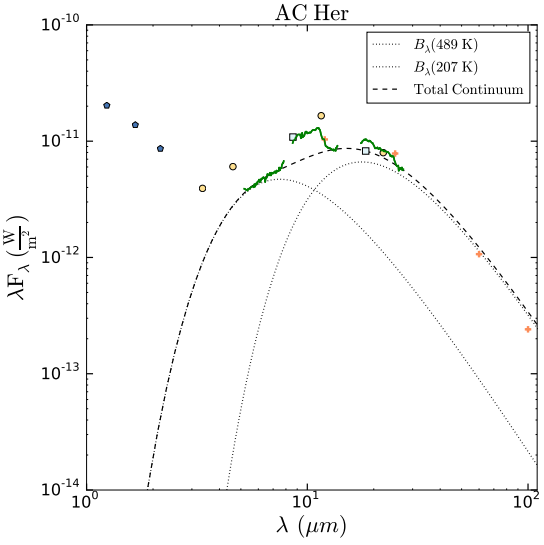

(g) AC Her

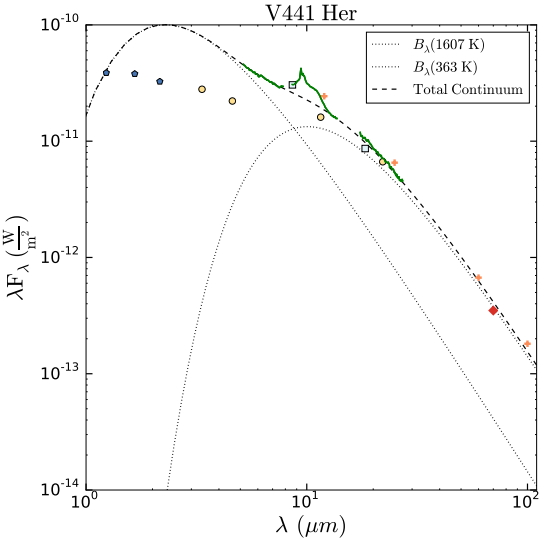

(h) V441 Her

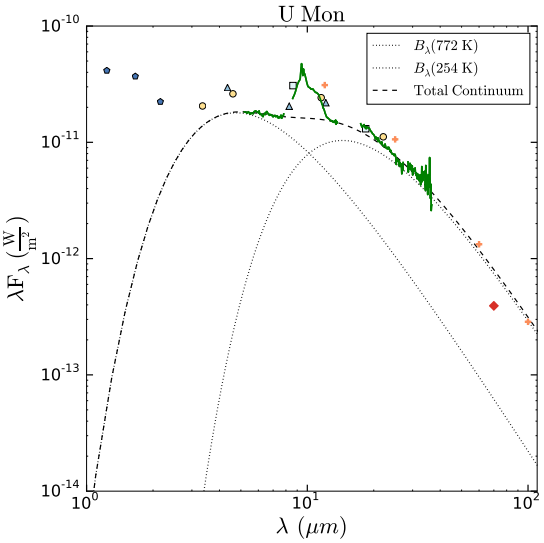

(i) U Mon

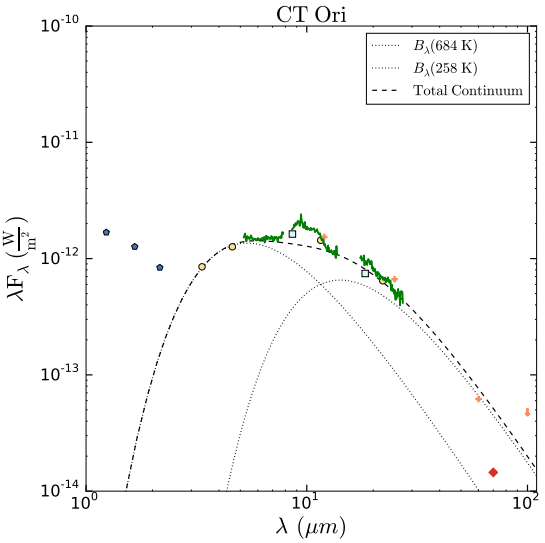

(j) CT Ori

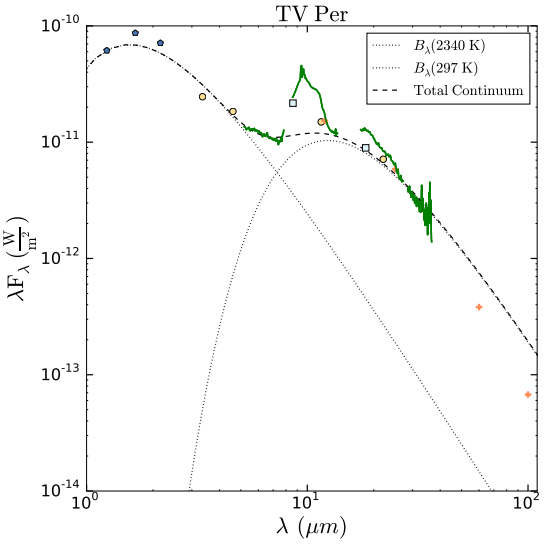

(k) TV Per

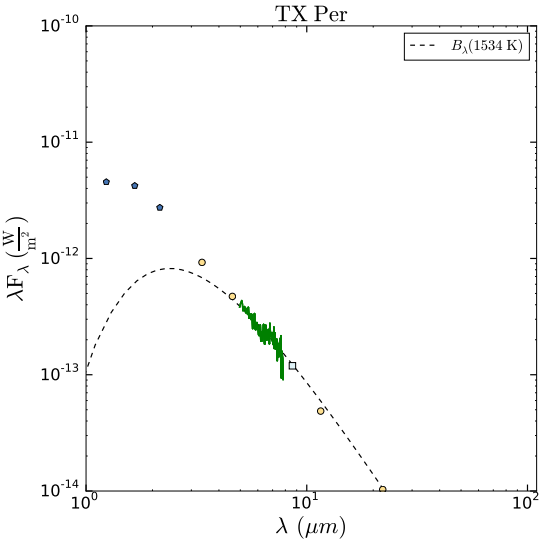

(l) TX Per

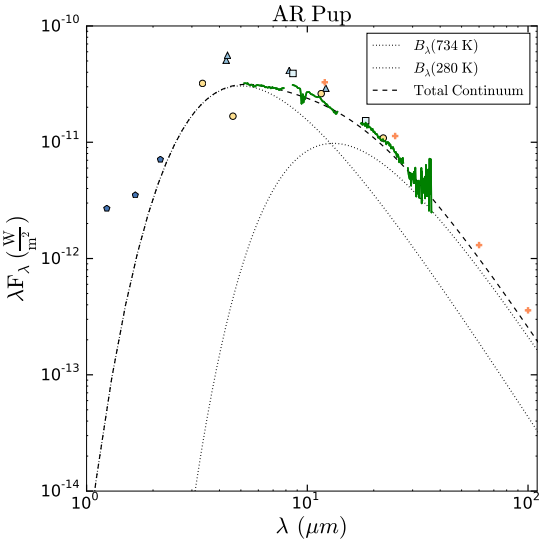

(m) AR Pup

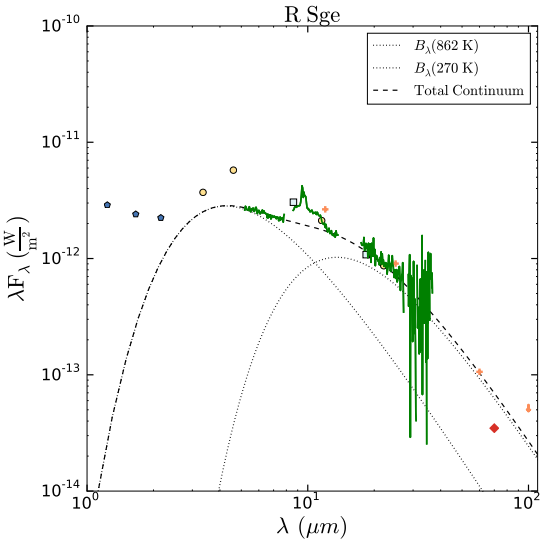

(n) R Sge

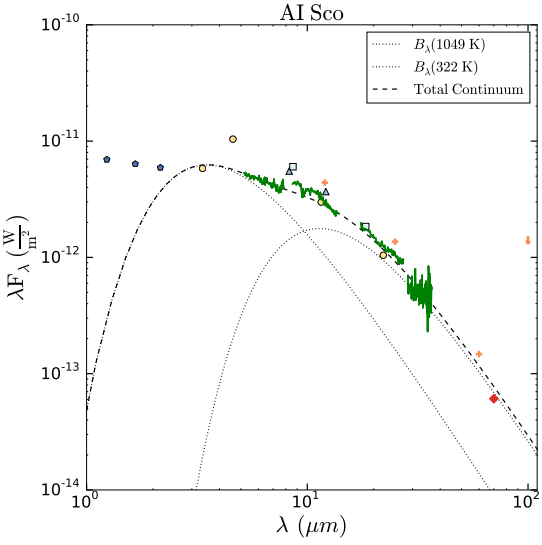

(o) AI Sco

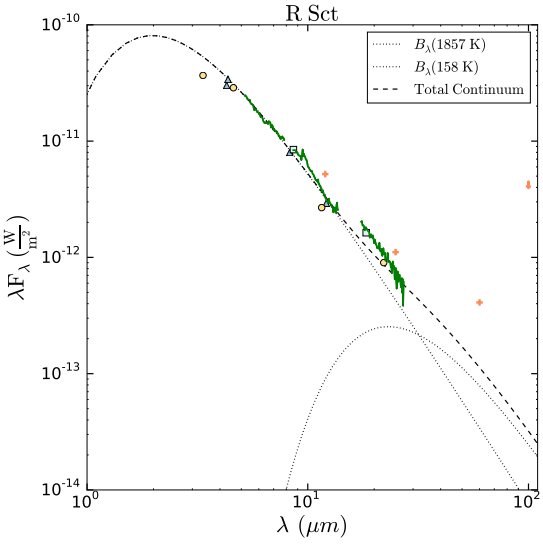

(p) R Sct

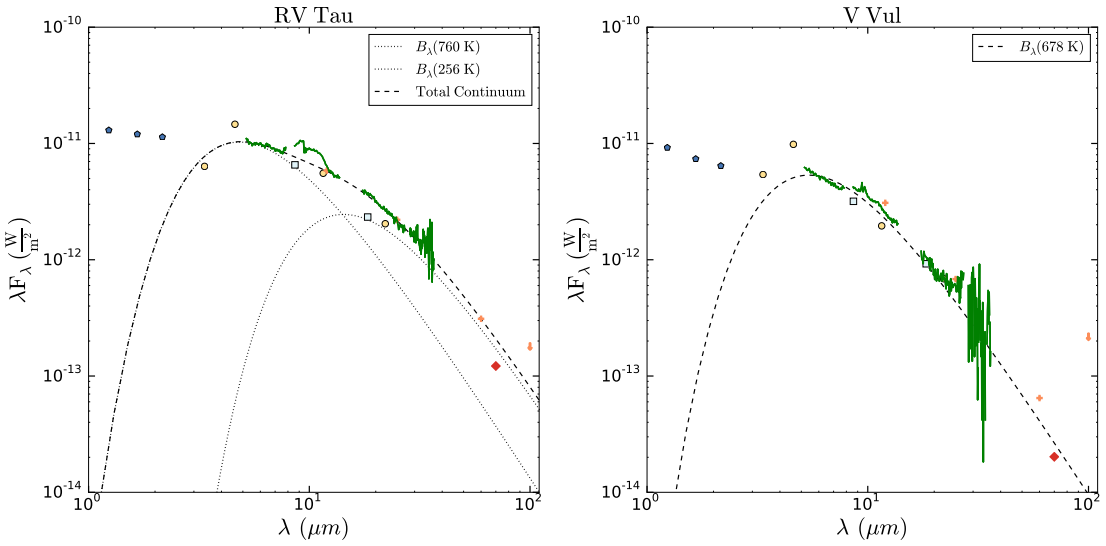

(q) RV Tau (r) V Vul

Figure 3.1 – The observed SOFIA/FORCAST spectrum (green curve) of our sample of stars is plotted together with the archival photometry from 2MASS (blue pentagons), *MSX* (blue triangles), *AKARI* (light blue squares), *WISE* (yellow circles), *IRAS* (orange crosses), *Herschel* (red diamonds), and the best fitting Planck functions (black dotted and dashed curves). *WISE* photometry upper limits are depicted as orange downward arrows.

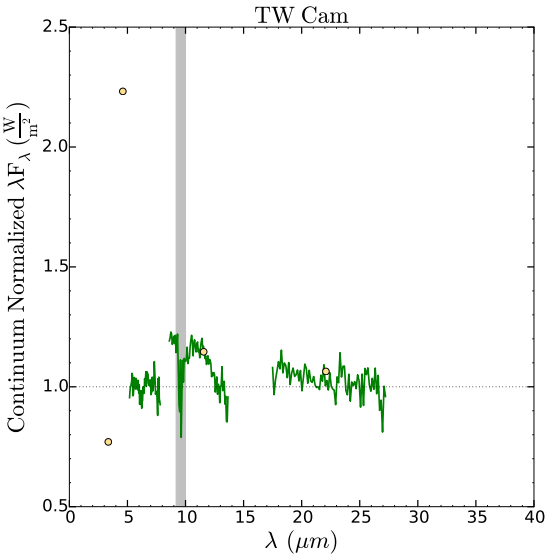

(a) TW Cam

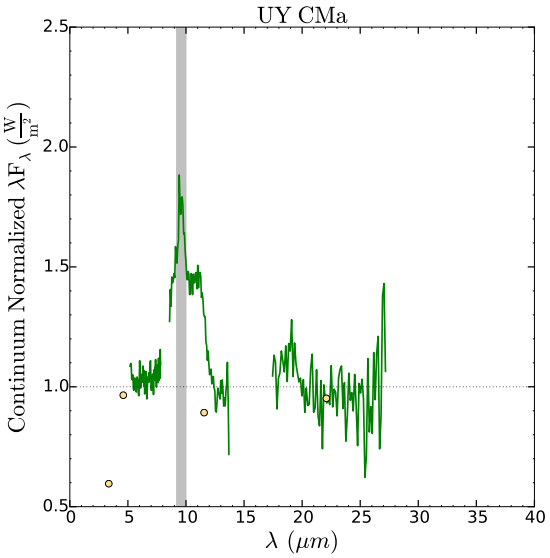

(b) UY CMa

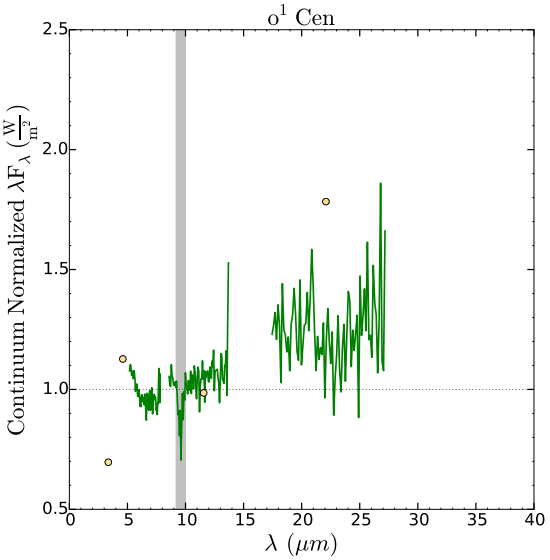

(c) o^1 Cen

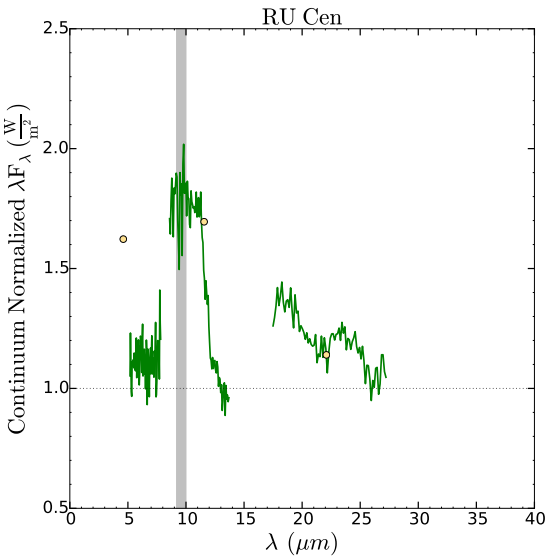

(d) RU Cen

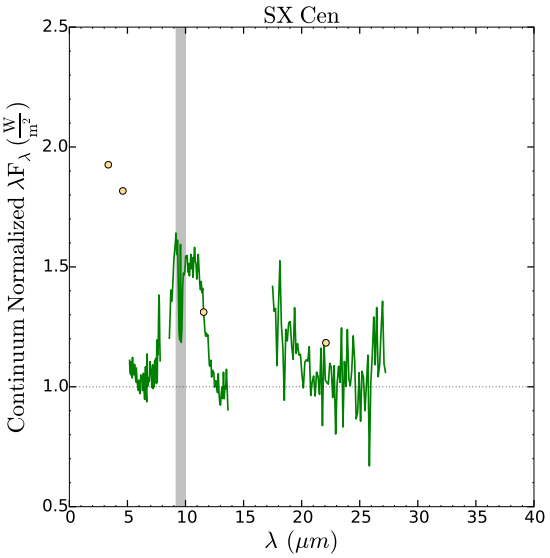

(e) SX Cen

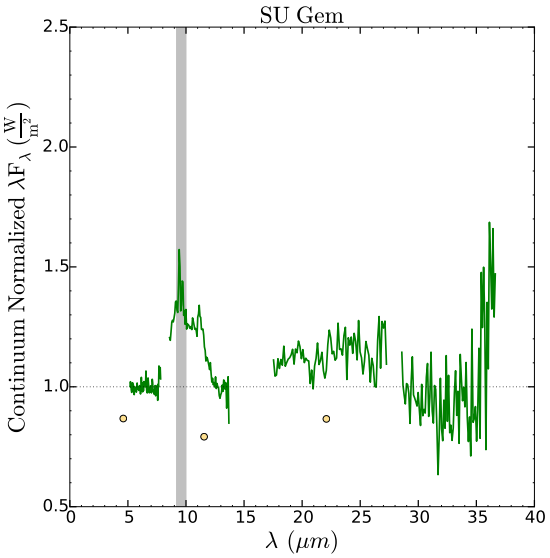

(f) SU Gem

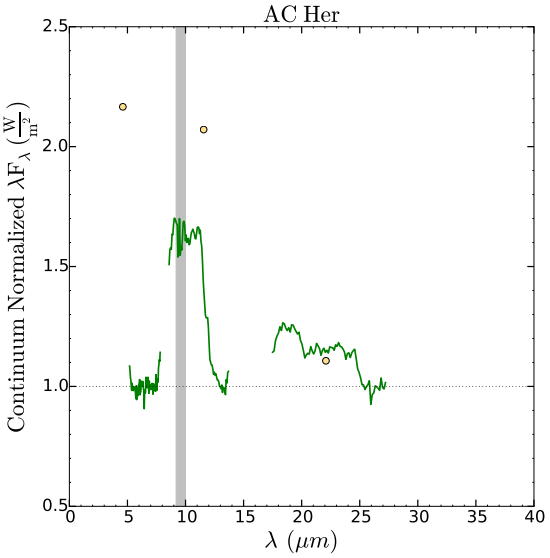

(g) AC Her

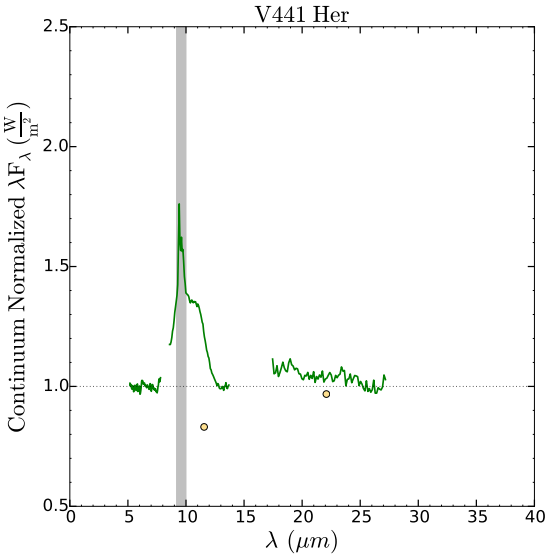

(h) V441 Her

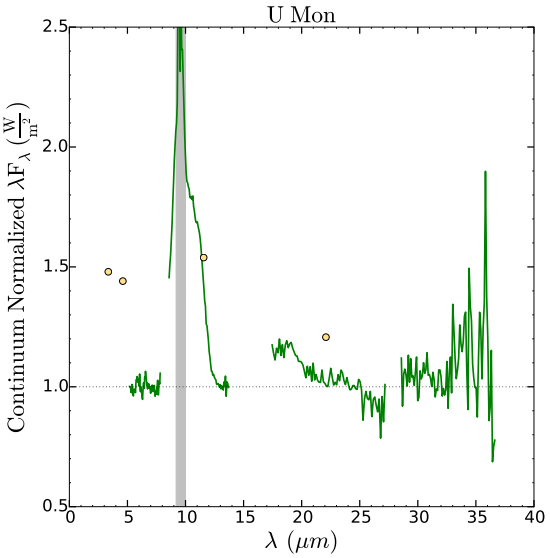

(i) U Mon

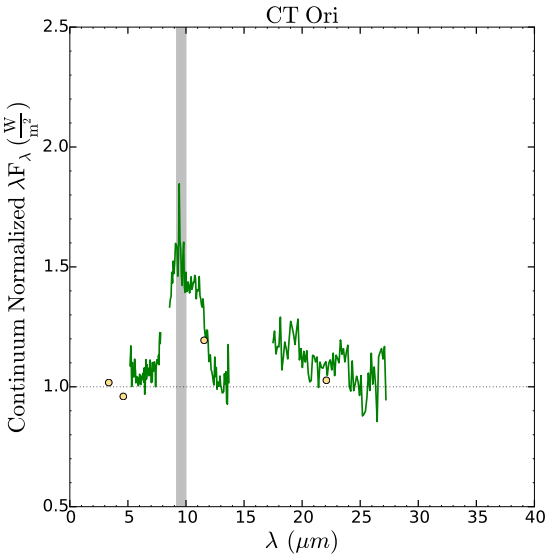

(j) CT Ori

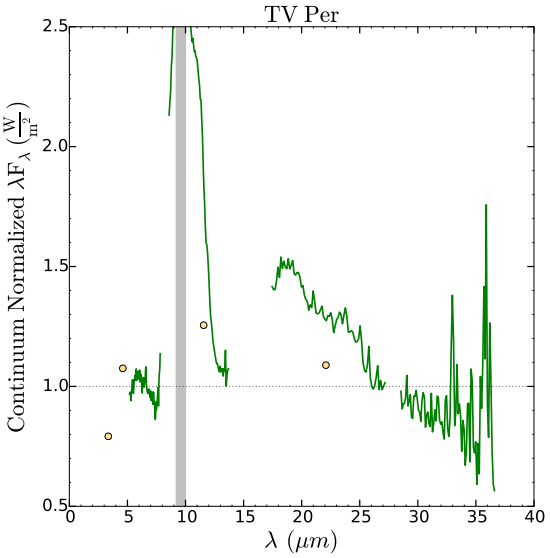

(k) TV Per

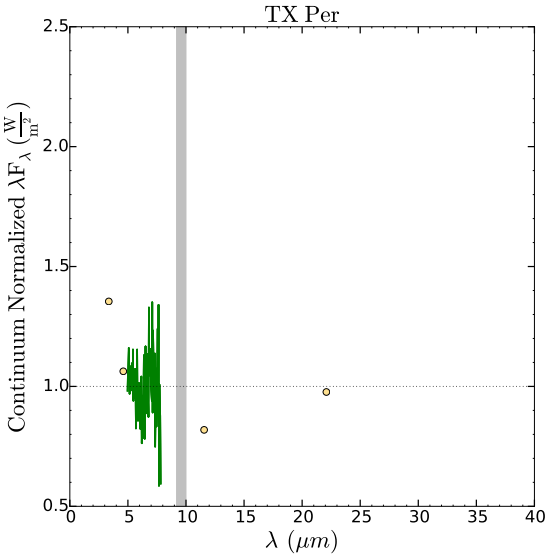

(l) TX Per

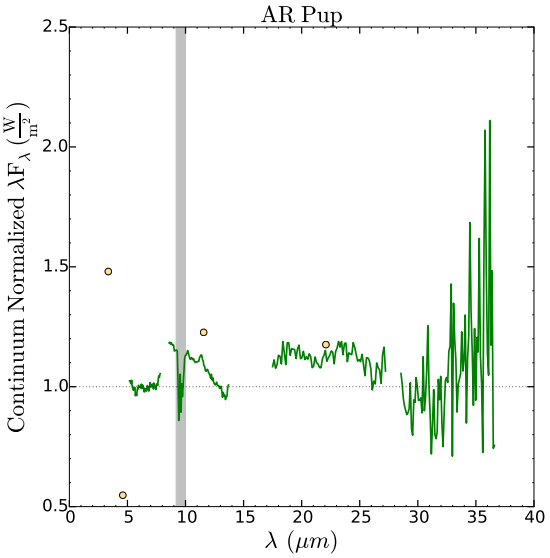

(m) AR Pup

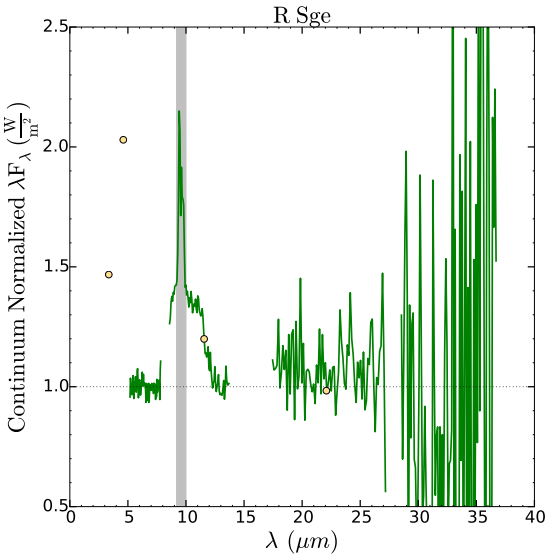

(n) R Sge

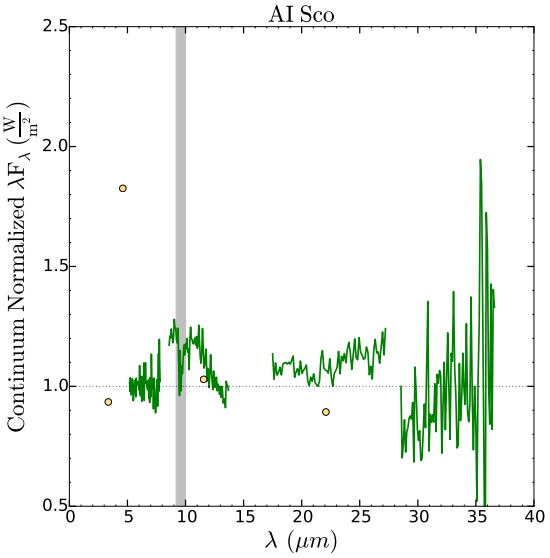

(o) AI Sco

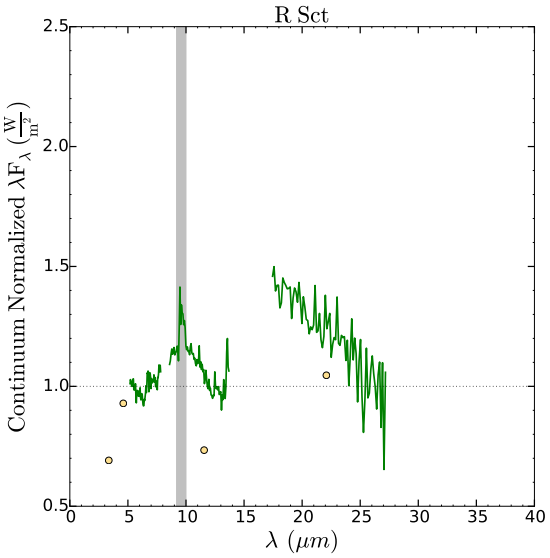

(p) R Sct

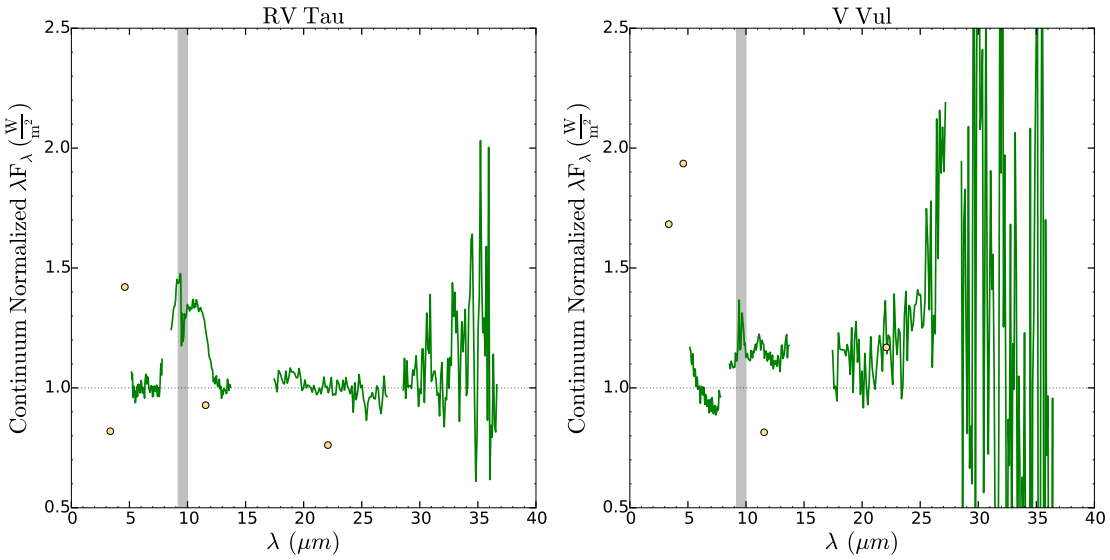

(q) RV Tau (r) V Vul

Figure 3.2 – Continuum normalized SOFIA/FORCAST spectrum (green curve) after dividing by the best fitting continuum of our sample of stars showing the *WISE* archival photometry (yellow points) and telluric ozone region (gray band).

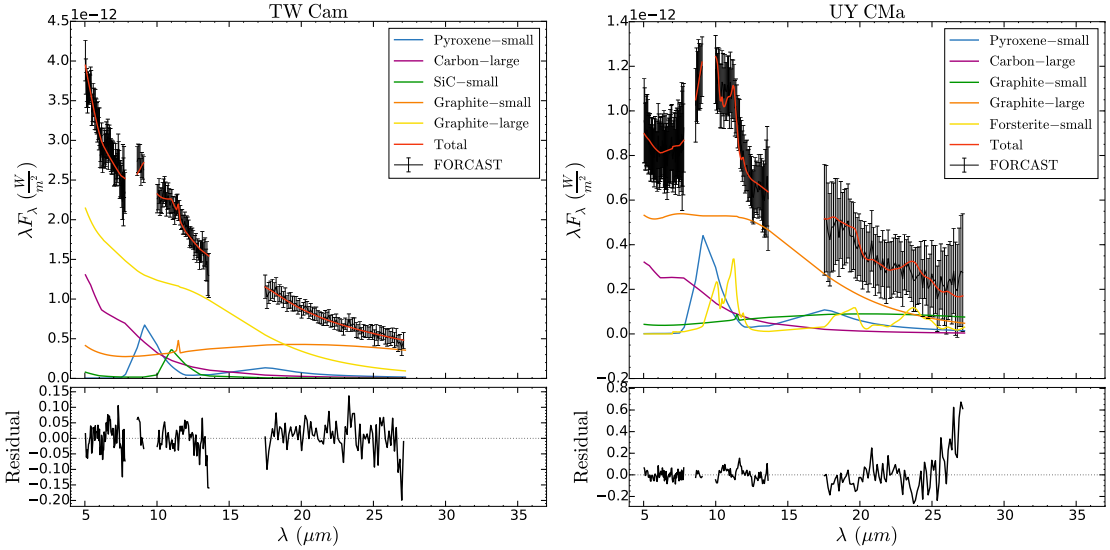

(a) TW Cam

(b) UY CMa

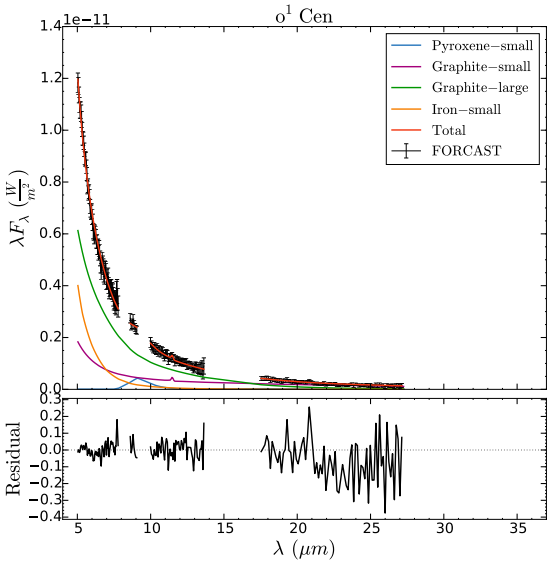

(c) o^1 Cen

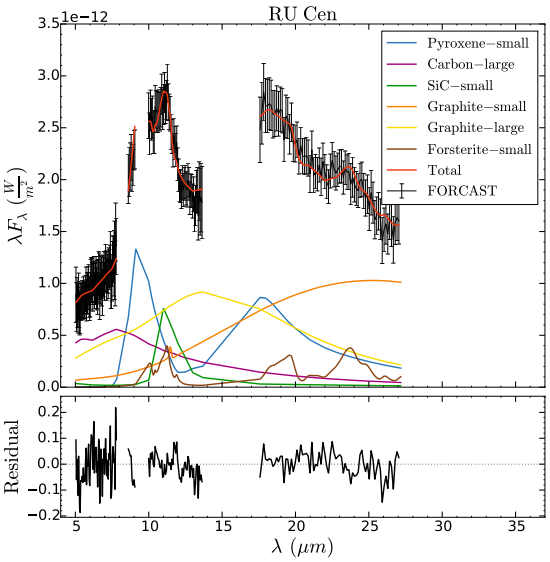

(d) RU Cen

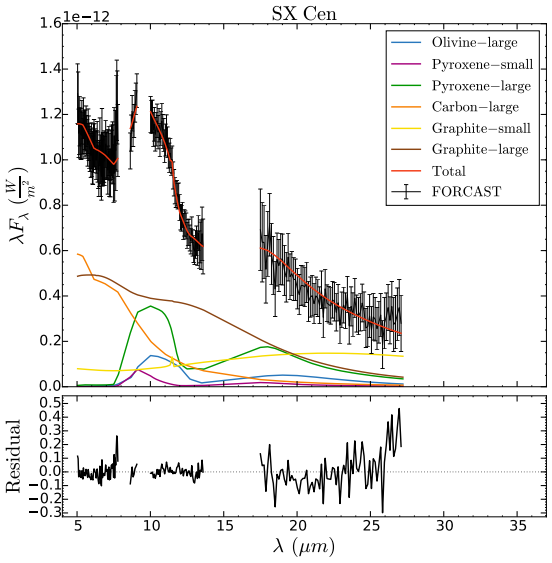

(e) SX Cen

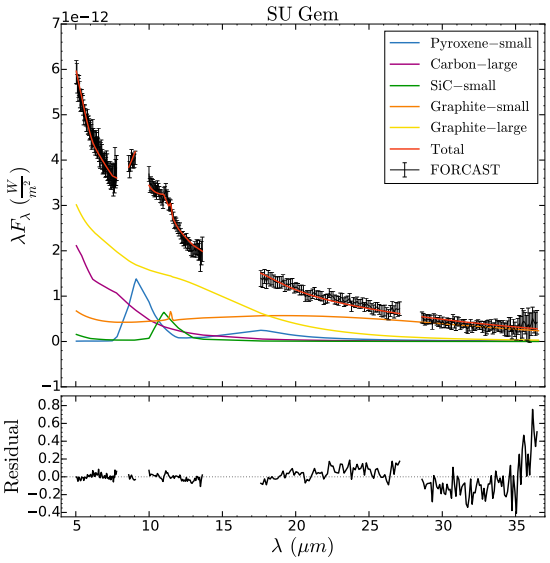

(f) SU Gem

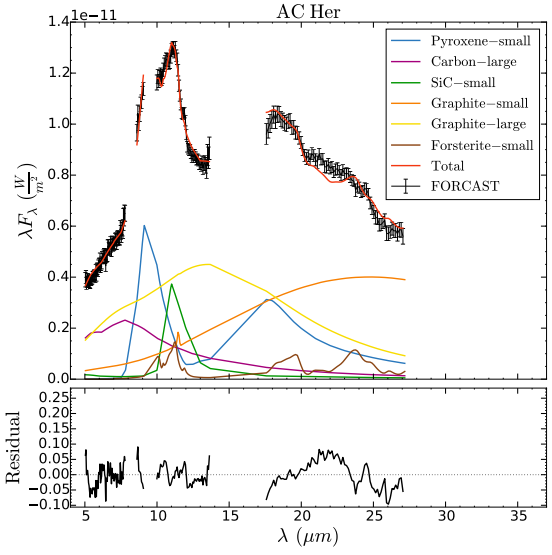

(g) AC Her

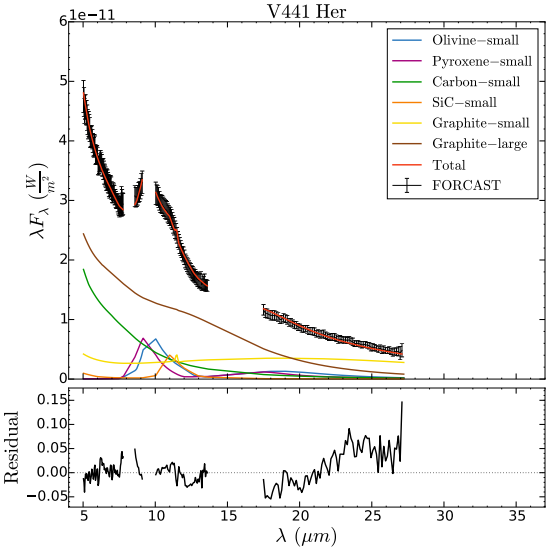

(h) V441 Her

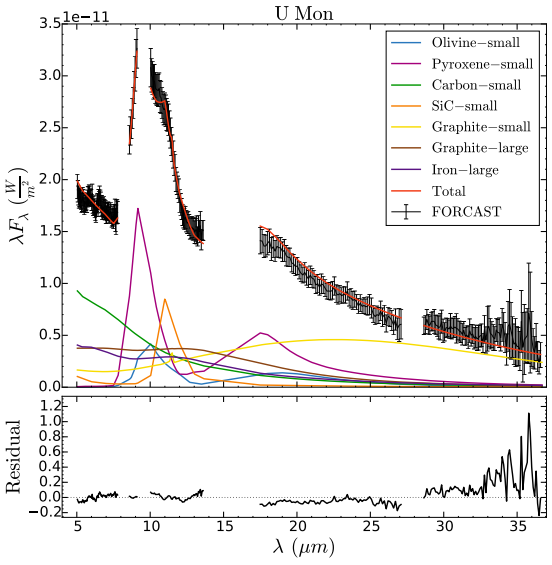

(i) U Mon

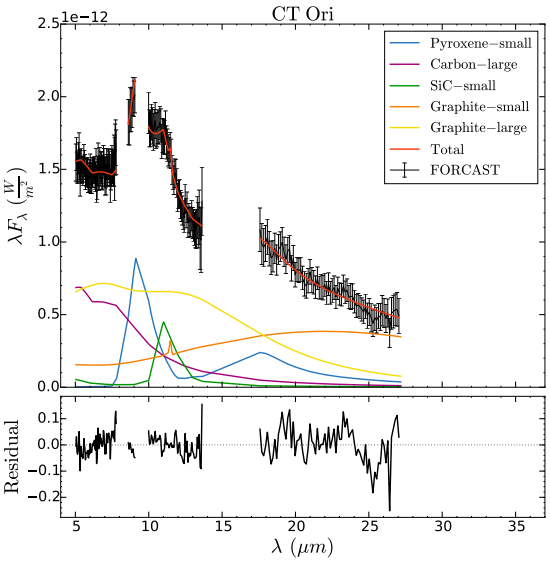

(j) CT Ori

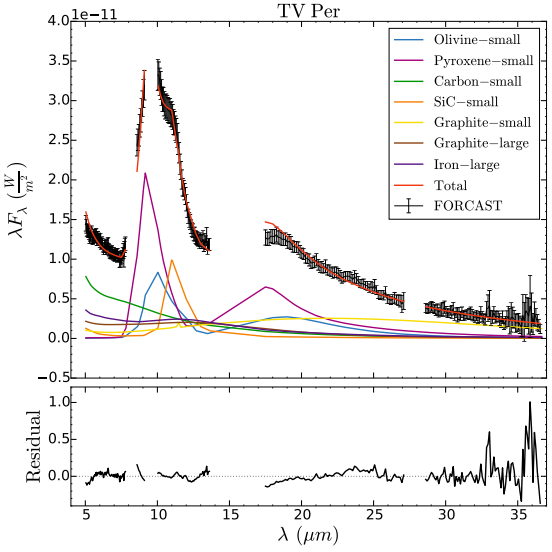

(k) TV Per

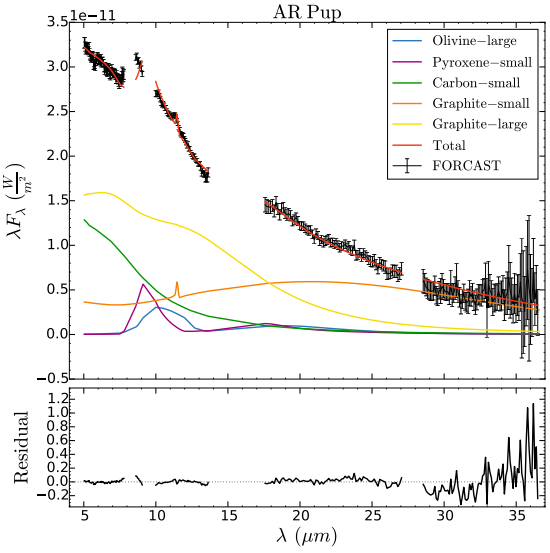

(l) AR Pup

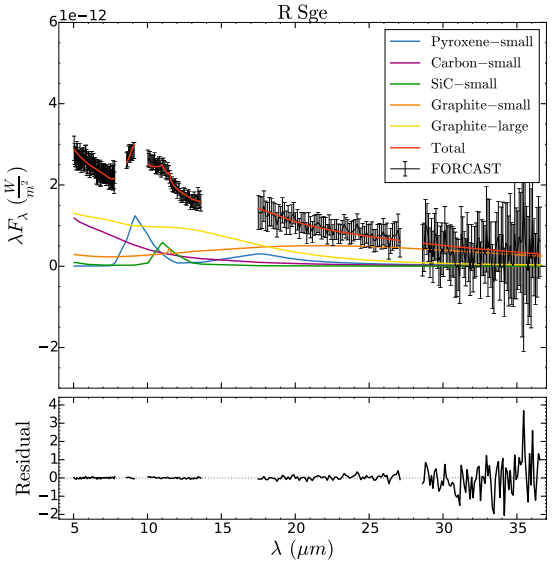

(m) R Sge

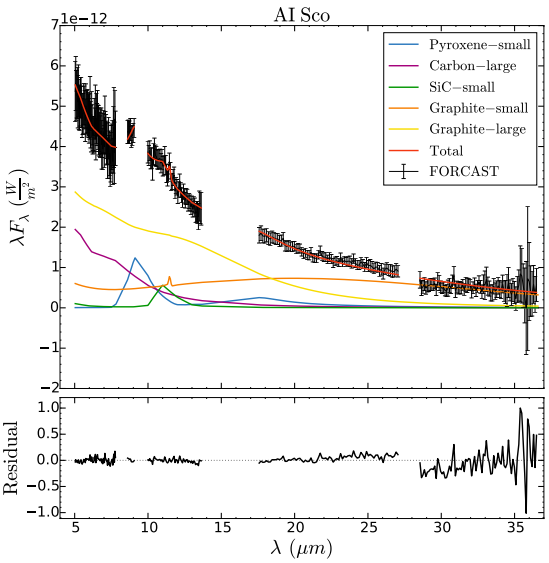

(n) AI Sco

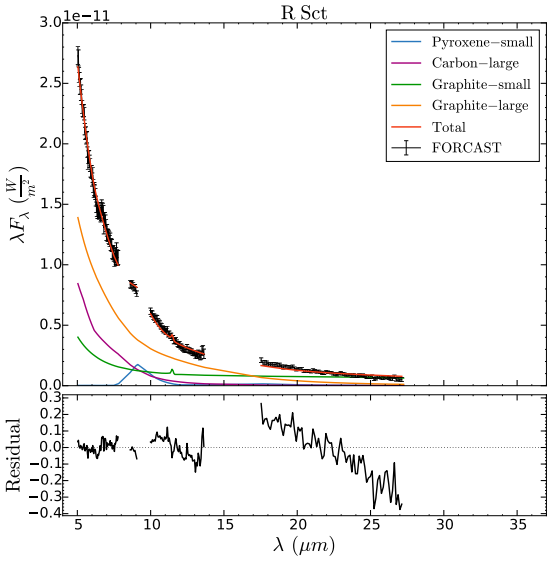

(o) R Sct

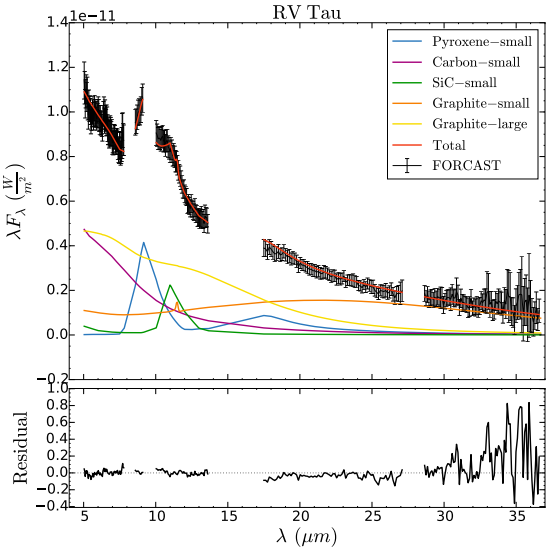

(p) RV Tau

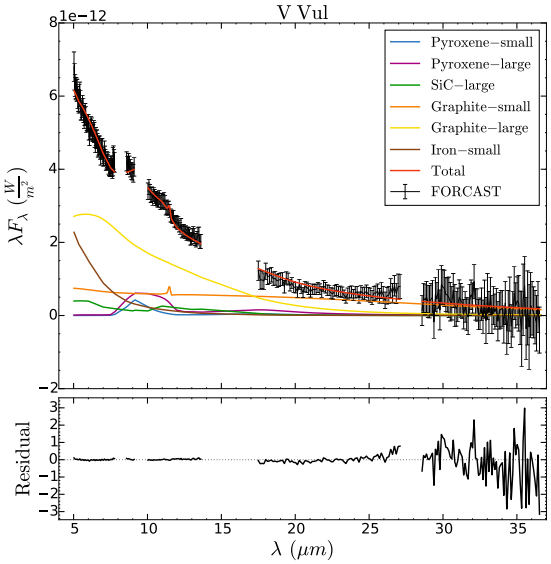

(q) V Vul

Figure 3.3 – Best model fits for our sample of stars, showing the contribution of the different mineral species. *Top*: the observed SOFIA/FORCAST spectra and 1σ errors (black points) are plotted together with the best model fit (red curve) and the mineral species (colored curves). The data points between 9.19 – 10.0 μm have been removed as these are strongly affected by telluric ozone absorption. *Bottom*: the normalized residual spectra after dividing by the best model of the observed spectra.

3.6 Discussion

The 10 and 20 μm emission features can be used to quantify the grain size and age of the circumstellar dust (van Boekel et al., 2003, 2005; Juhász et al., 2010). The peak-to-continuum ratio of the 10 μm feature can be used as a measure of the amount of grain growth because larger grains will produce a less prominent feature. In addition, the continuum subtracted 10/20 μm flux ratio has been shown to decrease monotonically with increased processing and therefore can be used to indicate the age of the circumstellar silicates (Nuth & Hecht, 1990). Older, more processed grains will have a lower 10/20 μm ratio. A plot of these two ratios for all our program stars can be seen in Figure 3.5. Most of the sources show a low peak to continuum value (i.e. < 2.0) and a low 10/20 μm ratio (i.e. < 50) indicating that the grains are relatively large and have undergone significant processing. This supports the idea that the dust is constrained to a Keplerian disk. There are two outliers in Figure 3.5, TV Per and UY CMa. TV Per has a high peak to continuum value and a small 10/20 μm ratio indicating that the dust grains are small and old. The small grain size is consistent with our model, which predicts a small spherical grain volume fraction of $\sim 74\%$ for TV Per. This suggests that the circumstellar environment around TV Per is such that the grains are unable to grow to large sizes. UY CMa has a low peak to continuum value and a large 10/20 μm ratio indicating that the dust grains are both large and young. This is also consistent with our model which predicts a small grain volume fraction of $\sim 50\%$ around UY CMa. Robinson & Hyland (1977) and Mitchell & Robinson (1981) found that for low optical depths, some of the circumstellar silicate dust may be in absorption rather than emission if it is at a low temperature. The viewing angle of the disks will also affect the peak-to-continuum ratio of the 10 μm feature (Crapsi et al., 2008) As mentioned in Section 3.4.2, factors like the grain size and shape will affect the observed emission features. The optical depth, viewing angle, temperature, and particle size of the grains may mask the 10/20 μm ratio and could contribute to the high volume fraction of small grains found by our model.

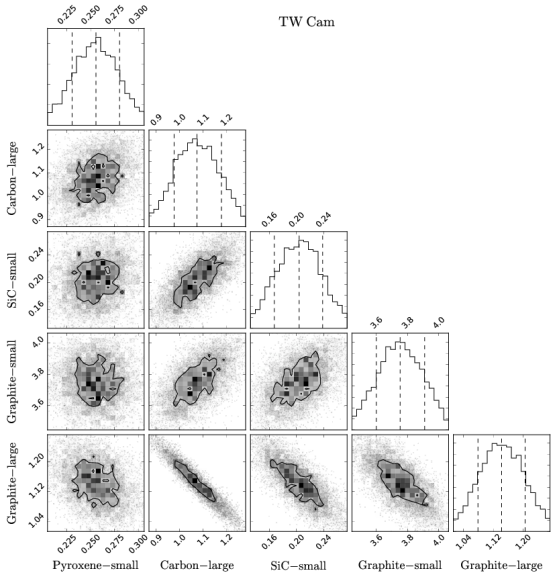

(a) TW Cam

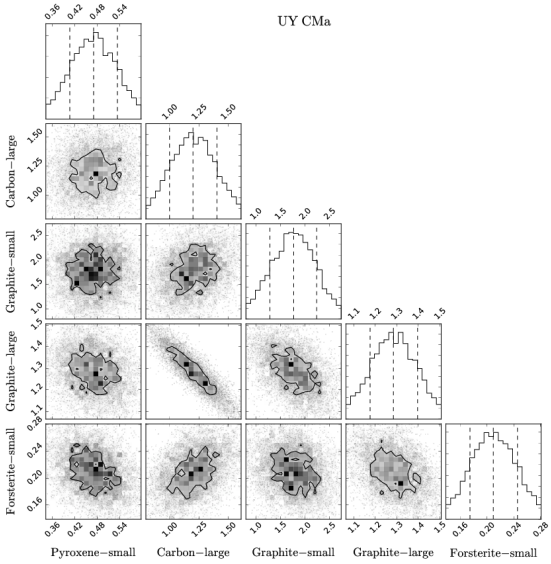

(b) UY CMa

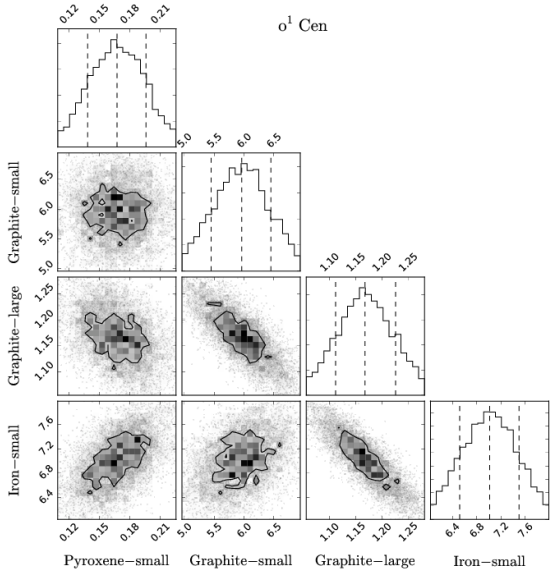

(c) o^1 Cen

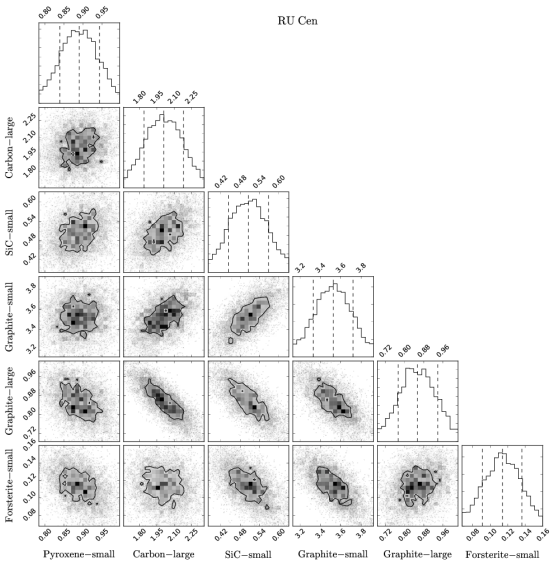

(d) RU Cen

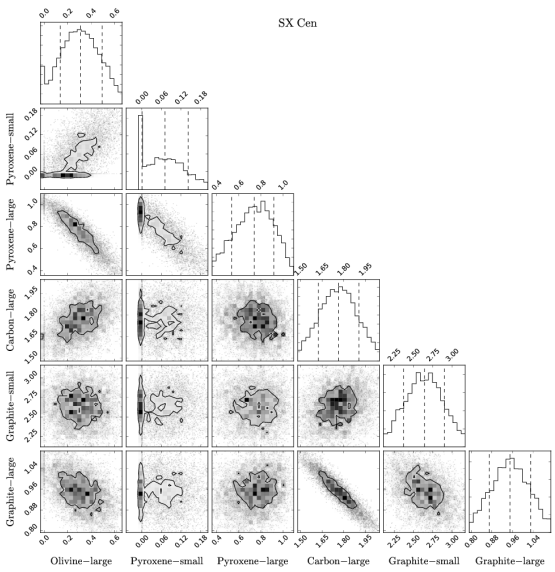

(e) SX Cen

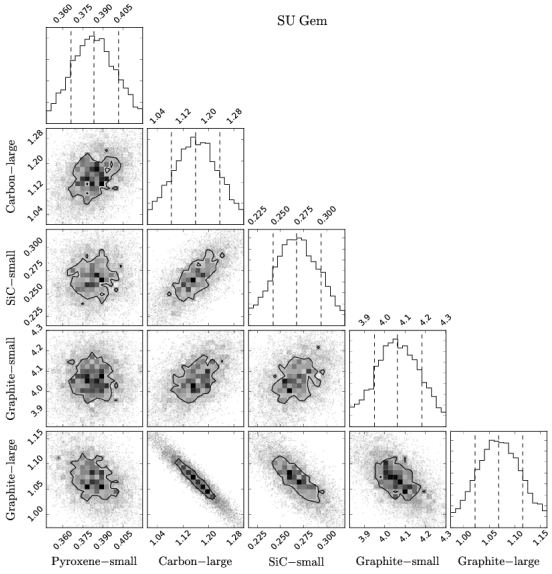

(f) SU Gem

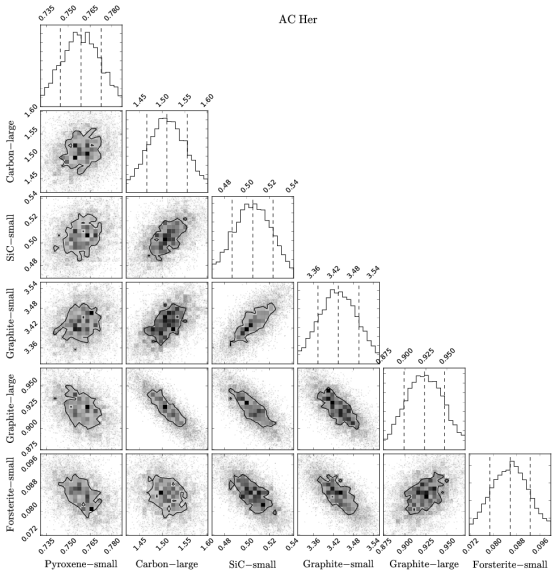

(g) AC Her

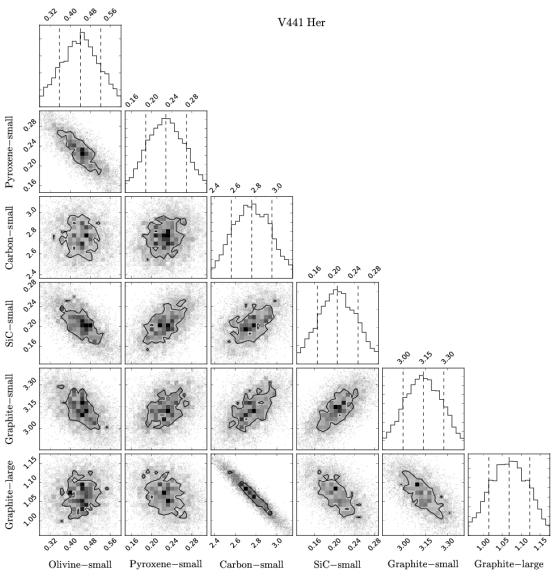

(h) V441 Her

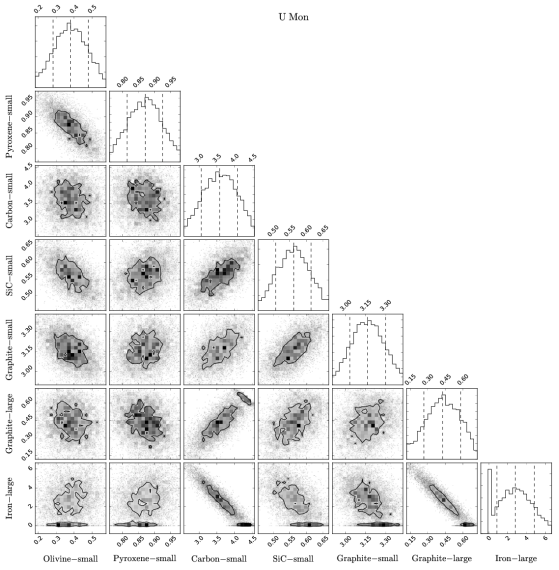

(i) U Mon

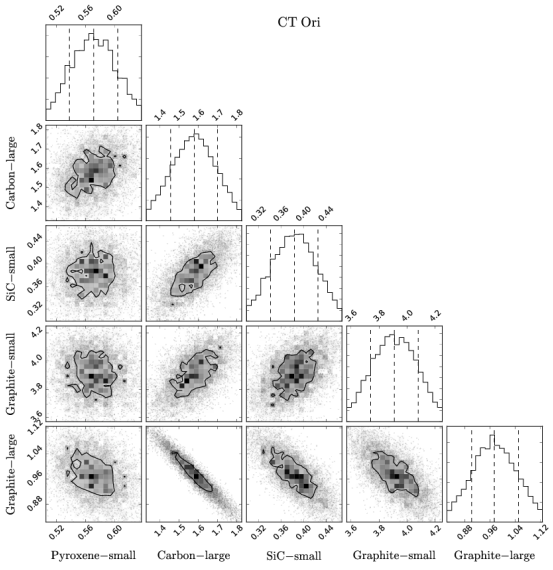

(j) CT Ori

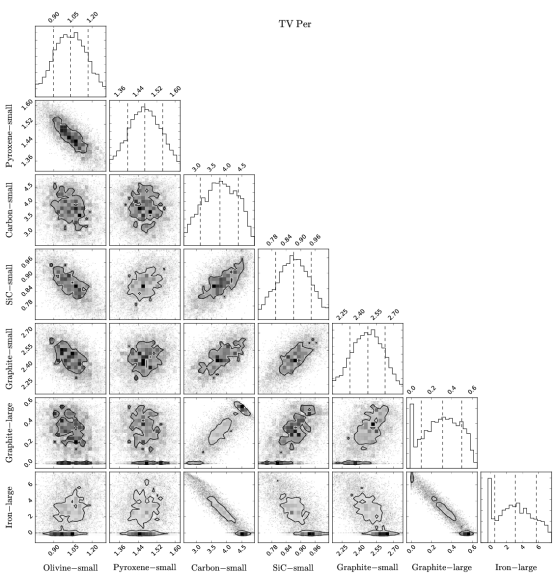

(k) TV Per

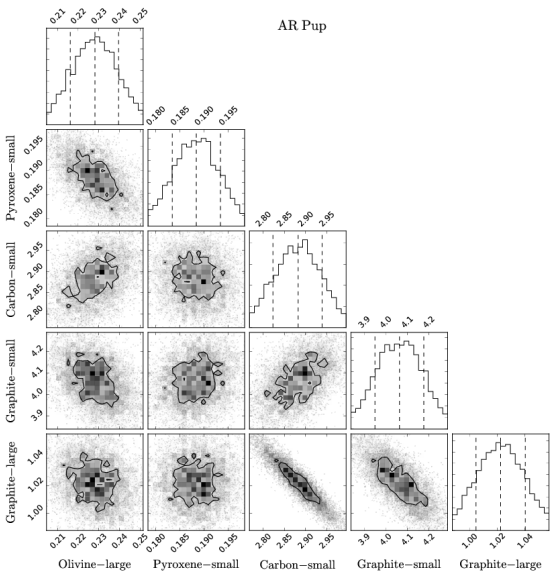

(l) AR Pup

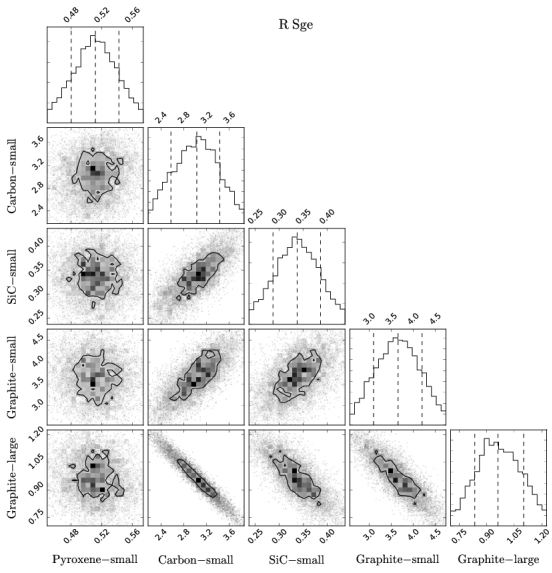

(m) R Sge

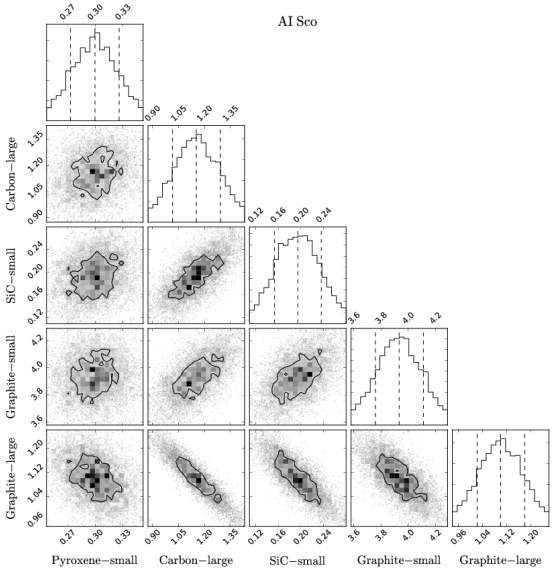

(n) AI Sco

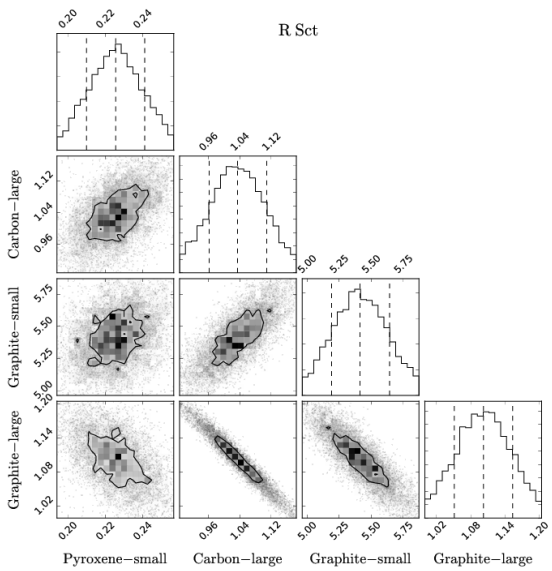

(o) R Sct

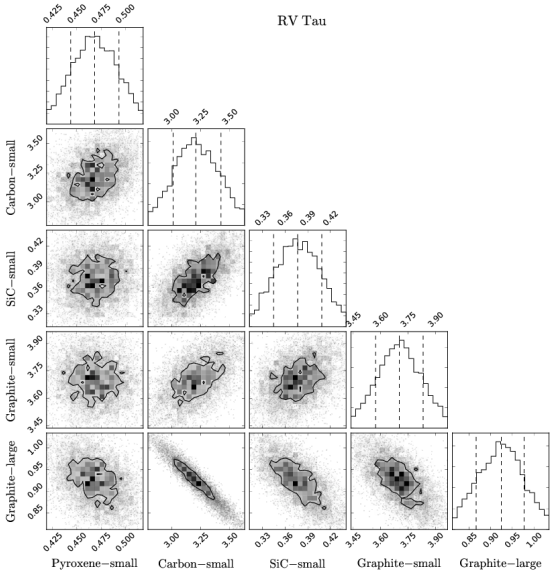

(p) RV Tau

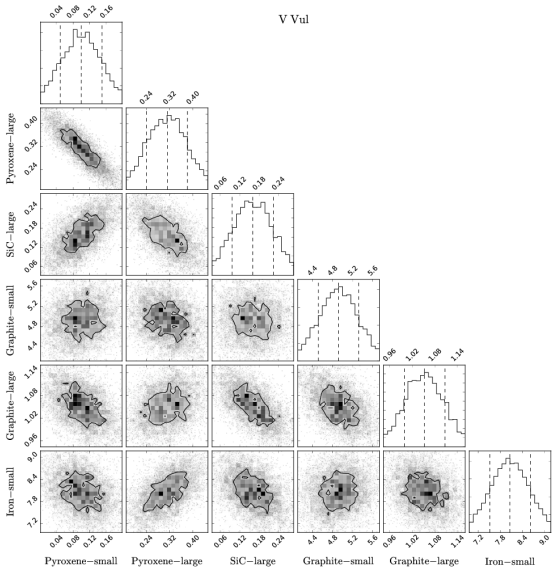

(q) V Vul

Figure 3.4 – Normalized probability distribution functions, c_i, of each mineral species after 5000 realizations of a Monte Carlo simulation with Gaussian noise distributions and the covariance between the coefficients. The dashed lines show the mean ($\overline{c_i}$) and the 1σ ($\sigma_{\overline{c_i}}$) confidence levels. The contours show the 1σ confidence levels.

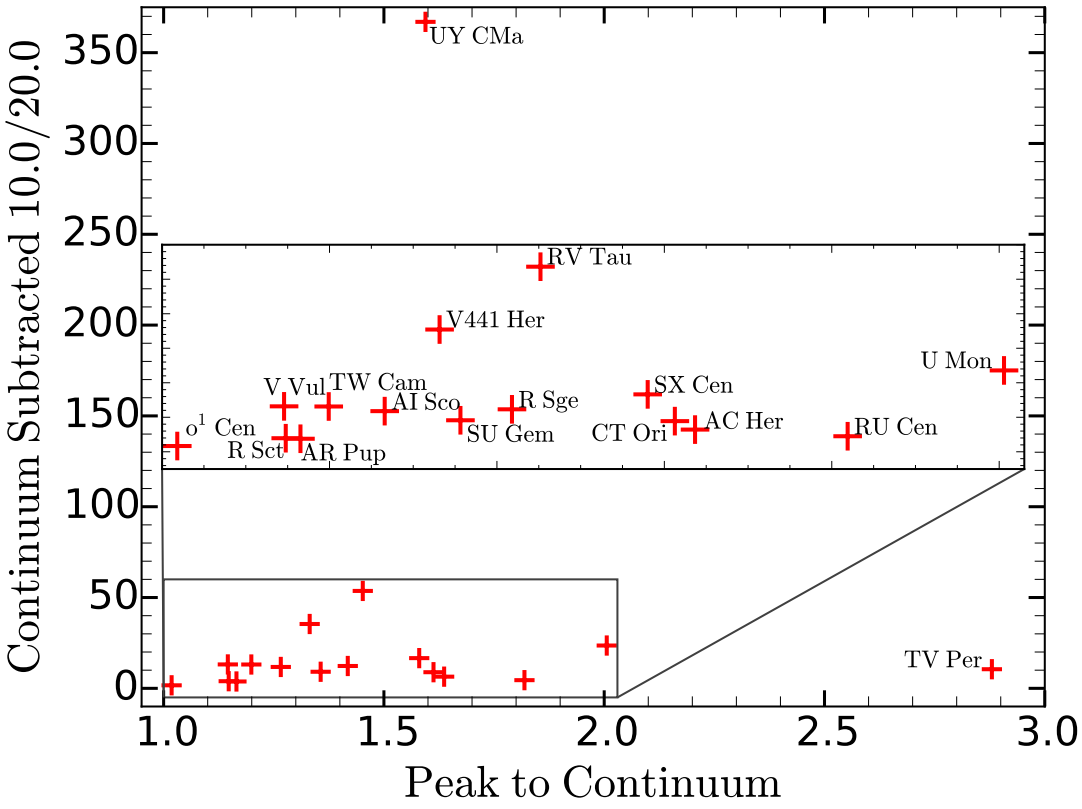

Figure 3.5 – Ratio of the continuum subtracted flux at 10 and 20 μm versus the peak to continuum ratio of the 10 μm silicate feature.

3.6.1 Crystallinity

Although Molster et al. (2002a,b) showed that the silicate crystallinity fraction in disk sources was much higher than that observed in outflow sources, we do not see a high silicate crystallinity fraction in any of the objects in our sample listed as "disk" SEDs in Table 3.2 and for all of the FORCAST spectra there are no obvious crystalline emission features present. One explanation is that crystalline silicate material is not abundant in any of the stars observed. However, crystalline olivines have been detected around AC Her and are thought to be present at the $\sim 10-50\%$ level around AR Pup and U Mon (Blommaert et al., 2014; de Ruyter et al., 2005). The lack of strong crystalline silicate emission features does not necessarily indicate a lack of presence. If a temperature difference exists between the amorphous and crystalline silicates, it is possible to include up to 40% of crystalline silicates in the circumstellar dust without seeing crystalline features in the spectra (Kemper et al., 2001). Another possible explanation for this observation is that crystalline silicates are generally colder than amorphous silicates, which could mean that the grains are not co-spatial or that they have different optical properties. In fact, when modeling the circumstellar material around AC Her, Hillen et al. (2015) found the spatial distribution of the forsterite to be different from the amorphous dust. The difference in optical properties could be due in part to the different iron content of each material, which increases the opacity in the near-IR significantly (Molster et al., 2002c; Dorschner et al., 1995). Additionally, the spectral features will be less prominent if the crystalline grains are larger than the amorphous grains. Therefore, if the crystalline silicates are only moderately abundant (i.e. $\lesssim 40\%$), cooler, and larger than the amorphous silicates, the spectral features of the crystalline silicates could easily be masked by the amorphous silicates. Interestingly, Blommaert et al. (2014) did not detect crystalline olivines around AR Pup and U Mon in the mid-IR and interpreted this as an indication that the crystalline olivines are hot ($\sim$ 600 K) around these two stars. If they are indeed hot, than the crystalline olivine abundances must be relatively low or the grains must be large around these two stars for them to go undetected by FORCAST.

3.6.2 Dual Chemistry

Our model predicts that most of the dust is carbon rich with some oxygen rich silicates. This dual formation of carbon and oxygen rich minerals has been observed in several classical novae, namely V1280 Sco (Sakon et al., 2016), V705 Cas (Evans et al., 2005), V842 Cen (Smith et al., 1994), and QV Vul (Gehrz et al., 1992) as well as IRAS 09425-6040, a carbon AGB star which shows circumstellar silicate dust features (Suh, 2016). The formation of both carbon rich and oxygen rich dust could be due to a chemical gradient in the wind as the stars evolve from oxygen rich to carbon rich after undergoing C dredge-up processes due to a recent AGB thermal pulse. Suh (2016) successfully modeled the dust envelope around IRAS 09425-6040 with an outer oxygen rich shell and an inner carbon rich shell, validating this hypothesis. Similarly, the carbon-rich planetary nebula BD $+30^\circ$ 3639 exhibits spatially separated carbon-rich polycyclic aromatic hydrocarbons and oxygen-rich silicate dust (Guzman-Ramirez et al., 2015). The post-AGB binary HR 4049 is a peculiar example of a depleted oxygen rich star with a featureless mid-IR spectrum possibly resulting from amorphous carbon masking the spectral features from silicates (Acke et al., 2013). While it is possible we may be observing the stars in transition from oxygen rich to carbon rich, it would require that all of these stars result from a narrow range of masses that terminate AGB evolution just as the carbon exceeds the oxygen abundance. A more plausible explanation for the dual chemistry mineralogy is that the dust formed in a common envelope environment of a binary system where the carbon and oxygen abundances can rapidly change. This mechanism has been invoked as the possible origin of post-AGB disks (Kashi & Soker, 2011; Lü et al., 2013; Hardy et al., 2016).

3.6.3 Viewing Effects

Most of the FORCAST continua are well described by two Planck functions, suggesting that we are viewing the systems from a nearly face-on orientation and see both the inner ($\sim$ 1000 K) and outer ($\sim$ 250 K) regions of the disks. Our results are corroborated by Hillen et al. (2015) who used a radiative transfer code to model the dust around AC Her as a highly evolved (i.e. mm sized grains), circumstellar disk with an inclination of $50 \pm 8^\circ$ and found good agreement with observations. Bujarrabal et al. (2007) detected

an extended bipolar outflow and an unresolved, compact (presumably disk) component around V441 Her with an inclination of $\sim 75°$. The typical uniform disk diameter of the N band emission region of the RV Tauri stars interferometrically observed by Hillen et al. (2017) is $\sim$ 40 mas. making it difficult to verify the inclination angle of other systems.

3.6.4 Limitations of the Fit

It is worth mentioning the various difficulties encountered in the modeling of the dust species present around our program stars and the limitations of our simplified model. As mentioned in Section 3.3, less than half of the program stars were observed with the G6 grism (28.7 – 37.1 μm). The addition of this data would have aided the modeling and identification of the minerals as crystalline silicates have prominent emission features in this region. Similarly, the lack of coverage from 14 – 17 μm between grisms G3 and G5 made it more difficult to constrain the abundance of amorphous silicates which have emission features around 17 μm. Amorphous carbon and metallic iron, on the other hand, lack prominent IR features and our model could be fitting these species to the overall dust continuum or temperature gradient thereby increasing the relative abundances.

Because our model included 13 dust species and some of the program stars had relatively low signal-to-noise FORCAST spectra, it was difficult to confirm the uniqueness of our models. For spectra with high signal-to-noise ratios, excluding dust species from the model had a noticeably negative impact on the goodness of fit (see Figure 3.6). Whereas, for low signal-to-noise spectra the exclusion of dust species changed the overall shape of the fit but the $\chi^2_{\rm red}$ values changed very little (see Figure 3.7). For both high and low signal-to-noise spectra, adding additional dust species improves the goodness of fit very little, if at all. We checked this by including Mg-rich crystalline enstatite (Jaeger et al., 1998a), iron oxide (FeO; Henning et al., 1995), amorphous alumina (porous; Begemann et al., 1997), and amorphous silica (Henning & Mutschke, 1997) to our model one at a time. The $\chi^2_{\rm red}$ values either remained the same or marginally improved for all of the program stars. The volume fraction of the added dust species depended on the signal-to-noise ratio of the spectra, with lower signal-to-noise spectra generally including 1 – 4% by volume and high signal-to-noise spectra including $\leq$ 1%

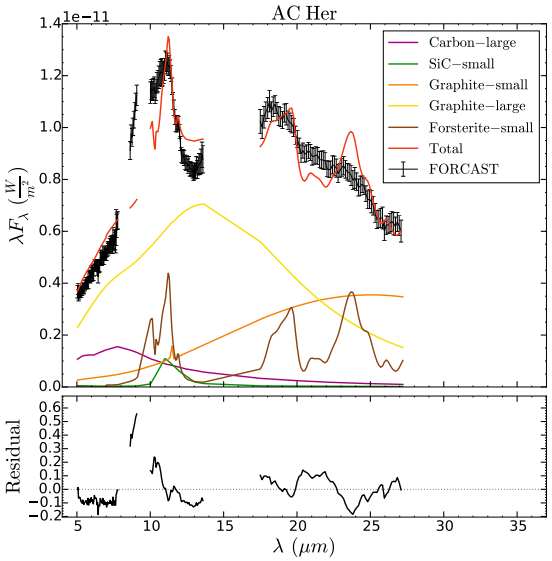

(a) Pyroxene-small removed; $\chi^2_{\text{red}} = 9.13$

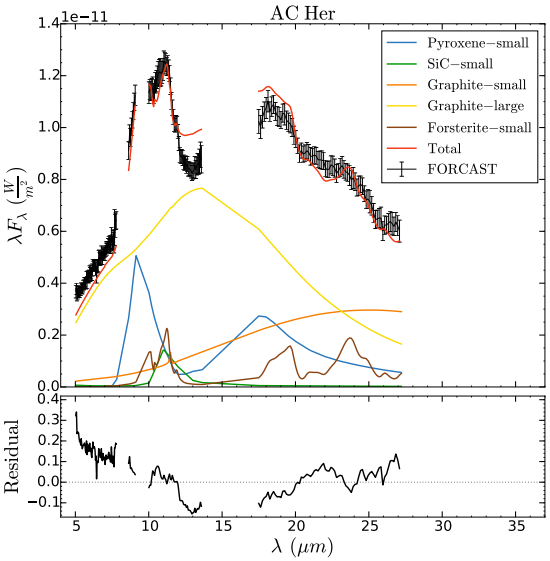

(b) Carbon-large removed; $\chi^2_{\text{red}} = 5.45$

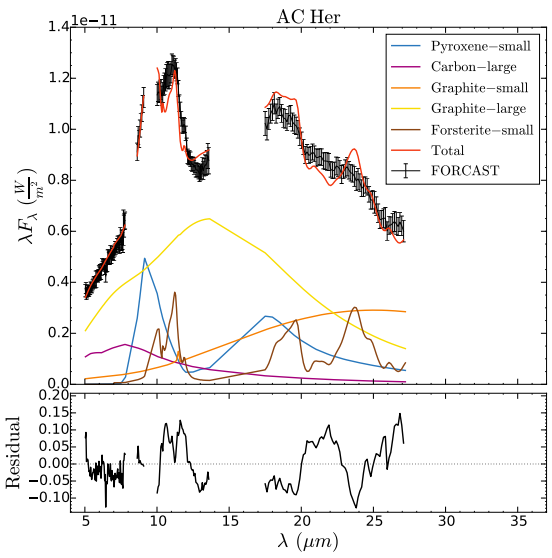

(c) SiC-small removed; $\chi^2_{\text{red}} = 2.37$

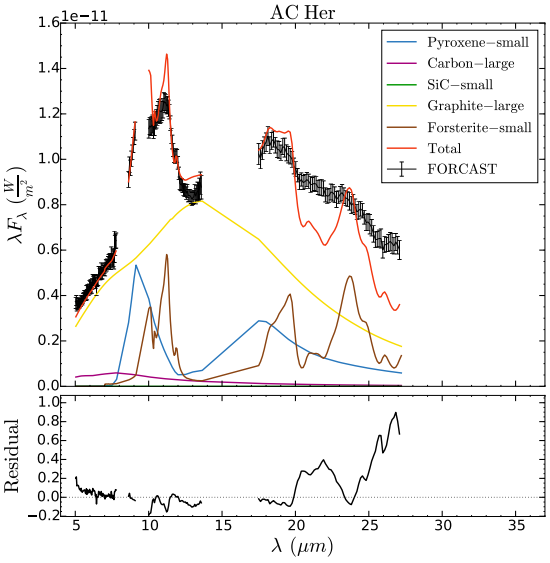

(d) Graphite-small removed; $\chi^2_{\text{red}} = 10.2$

by volume. Figure 3.8 illustrates the effect of adding additional dust species to AC Her (high signal-to-noise spectra) and Figure 3.9 illustrates the effect of adding additional dust species to UY CMa (low signal-to-noise spectra).

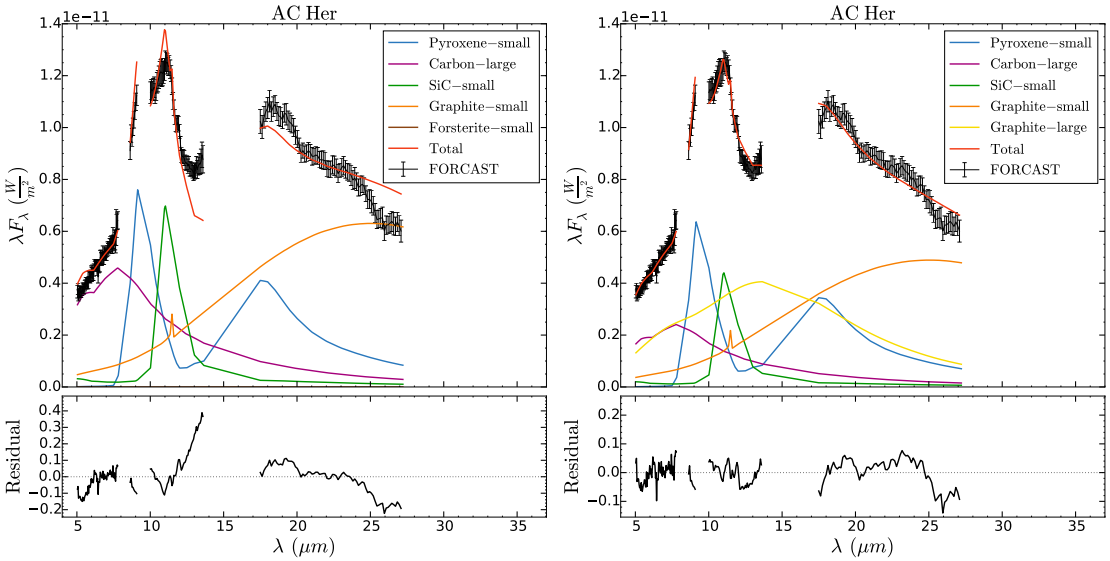

(e) Graphite-large removed; $\chi^2_{\rm red} = 5.46$ (f) Forsterite removed; $\chi^2_{\rm red} = 1.01$

Figure 3.6 – The effect on the fit when *removing* dust species from the best model of AC Her.

3.6.5 Crystallinity of the ISM

An upper limit on the degree of crystallinity of silicates in the diffuse ISM has been estimated by Kemper et al. (2004) to be $0.2\% \pm 0.2\%$ by mass. This estimate is similar to the average crystalline silicate fraction we find for our program stars of $0.4\% \pm 0.05\%$ by volume. We concur with Kemper et al. (2004) that this suggests crystalline material is either diluted in the ISM by other amorphous grain producing processes such as supernovae, or there is an amorphization process that occurs in the ISM on a shorter timescale than the destruction timescale, possibly heavy ion bombardment. Our mineralogy model of each star predicts that the majority of the dust is in the form of graphite and amorphous carbon. On average our model predicts $80\% \pm 1\%$ graphite and amorphous carbon, and $57\% \pm 1\%$ graphite around each star by volume. This large volume fraction of graphite and carbon around post-AGB stars may help explain the 2175 Å bump observed in the interstellar extinction curve which is possibly due to these two species (Rouleau et al., 1997; Duley & Seahra, 1998; Bradley et al., 2005).

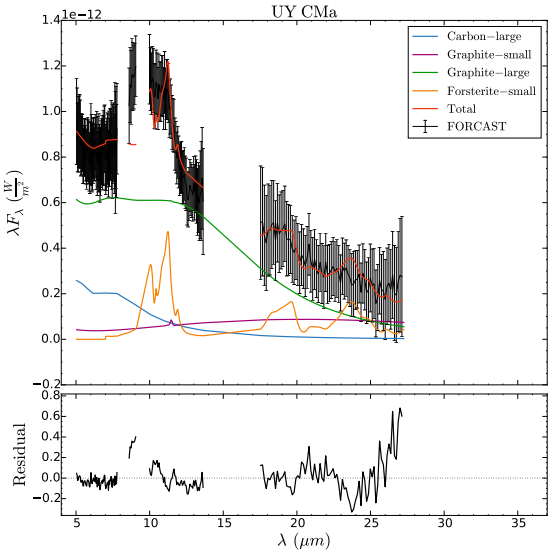

(a) Pyroxene-small removed; $\chi^2_{\rm red} = 0.34$

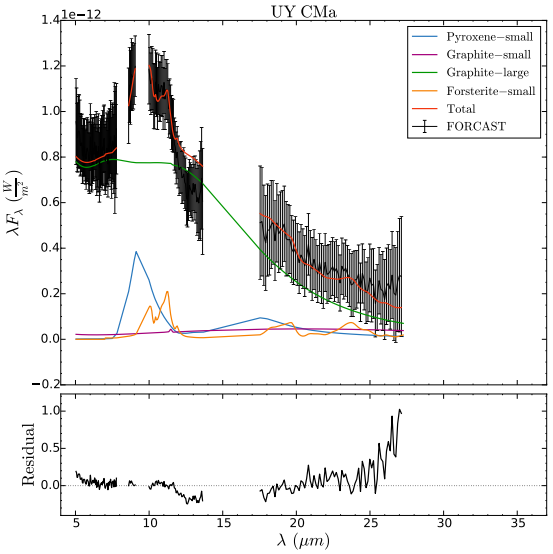

(b) Carbon-large removed; $\chi^2_{\rm red} = 0.25$

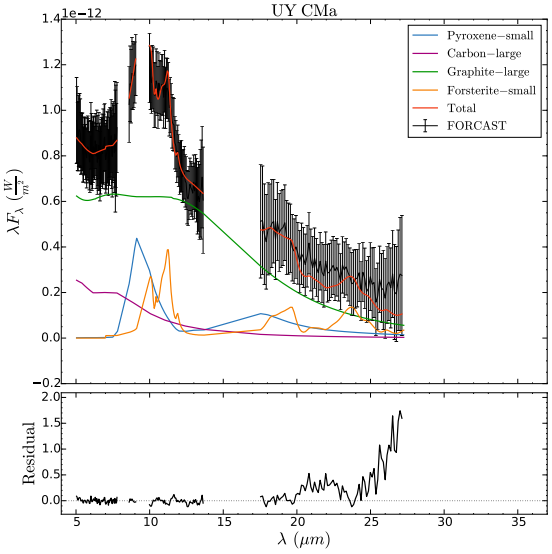

(c) Graphite-small removed; $\chi^2_{\rm red} = 0.14$

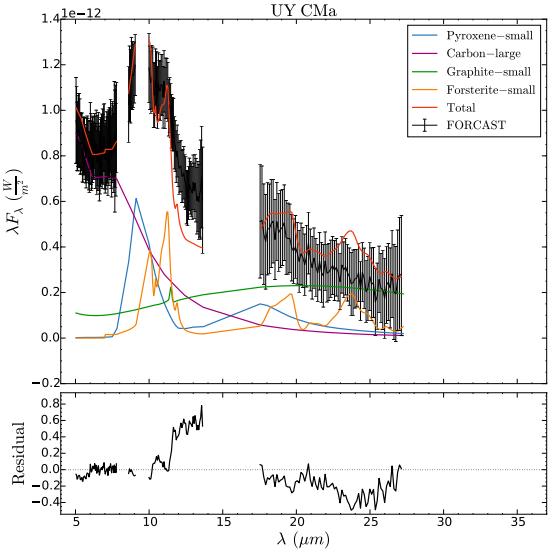

(d) Graphite-large removed; $\chi^2_{\rm red} = 0.90$

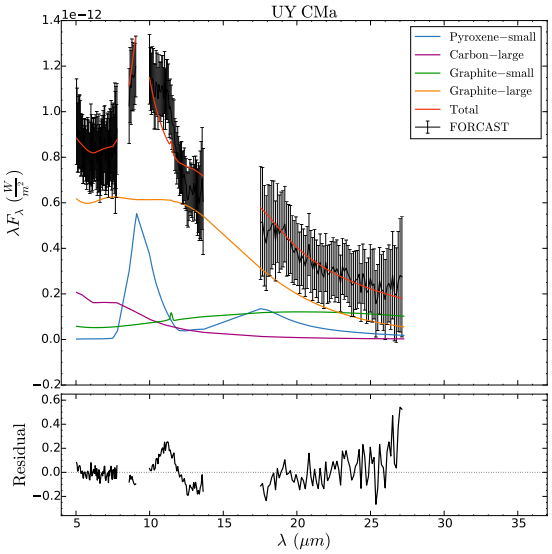

(e) Forsterite removed; $\chi^2_{\rm red} = 0.26$

Figure 3.7 – The effect on the fit when *removing* dust species from the best model of UY CMa.

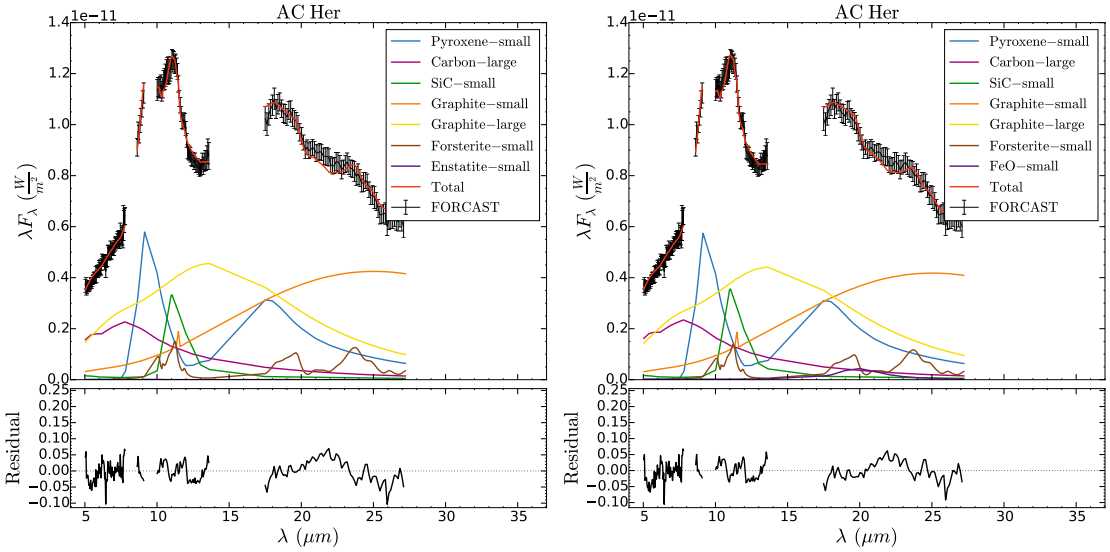

(a) Enstatite-small added; $\chi^2_{\rm red} = 0.61$

(b) FeO-small added; $\chi^2_{\rm red} = 0.56$

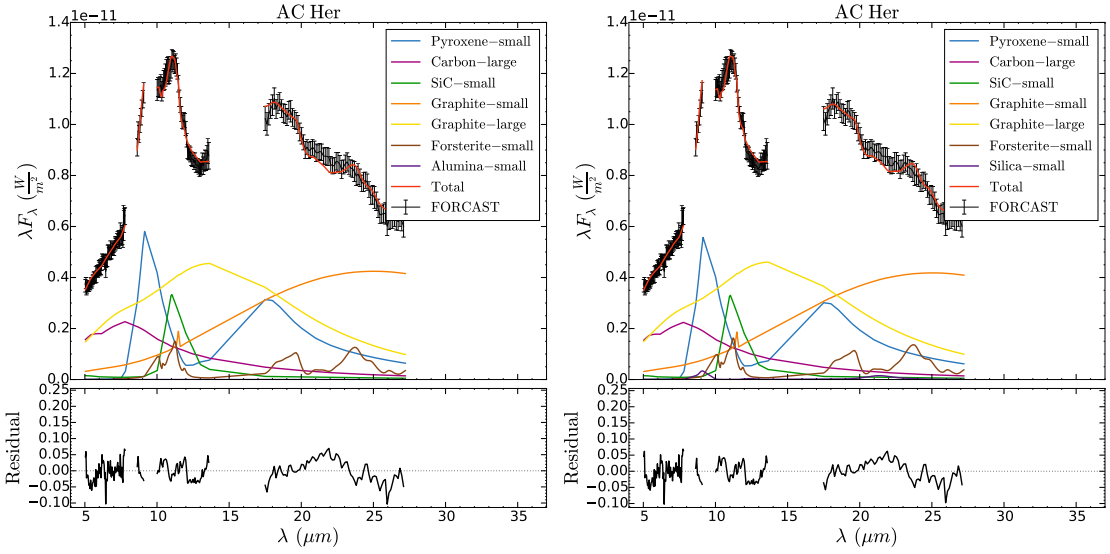

(c) Alumina-small added; $\chi^2_{\rm red} = 0.61$

(d) Silica-small added; $\chi^2_{\rm red} = 0.59$

Figure 3.8 – The effect on the fit when *adding* dust species to the best model of AC Her. The best fitting coefficient, c_i, for Alumina-small in panel (c) was 0.00.

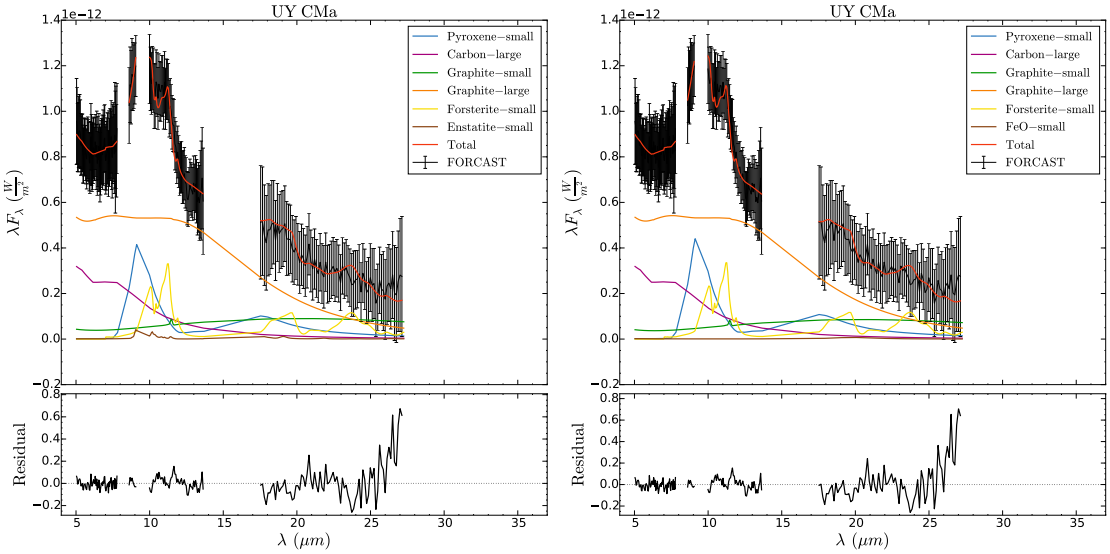

(a) Enstatite-small added; $\chi^2_{\rm red} = 0.085$

(b) FeO-small added; $\chi^2_{\rm red} = 0.085$

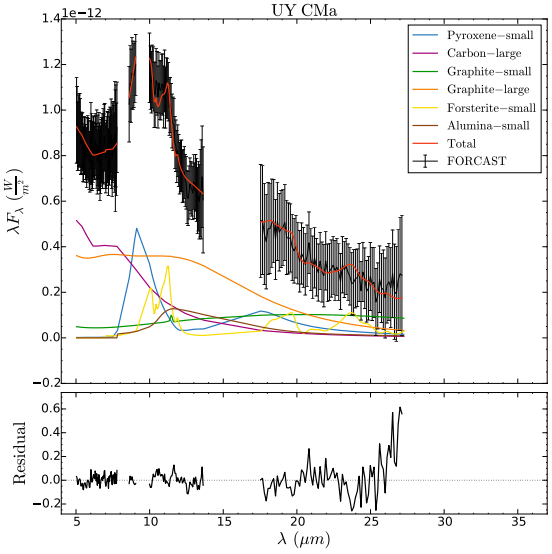

(c) Alumina-small added; $\chi^2_{\rm red} = 0.080$

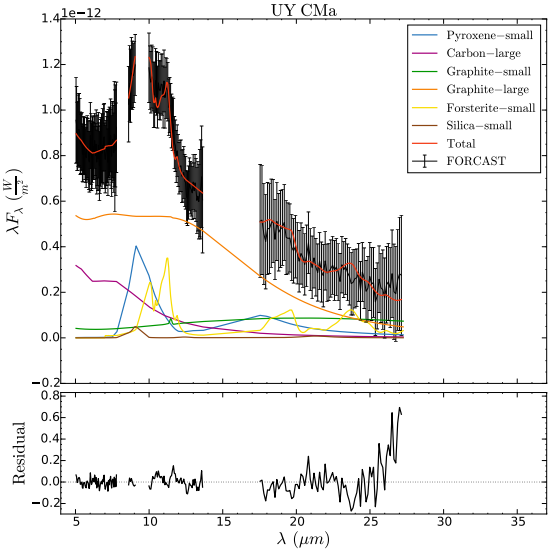

(d) Silica-small added; $\chi^2_{\rm red} = 0.085$

Figure 3.9 – The effect on the fit when *adding* dust species to the best model of UY CMa.

3.7 Conclusion

We have presented a first look at data obtained with SOFIA/FORCAST of 15 RV Tauri and 3 SRd variable stars. These data have demonstrated the diversity of dust features present in these systems, possibly tracing the evolutionary track from post-AGB star to PN. These observations of IR excess support the hypothesis that the systems in question are at an advanced stage in their transition to PNe. Our main conclusions can be summarized as follows:

- Almost all of the stars observed display a 10 μm and/or 20 μm emission feature. For most of the stars observed, the FORCAST continua are well described by two Planck functions one at $\sim$ 1000 K and one at $\sim$ 250 K with a majority of the dust ($\sim$ 97%) in the cooler form. A single Planck function fit the underlying contiuum of o^1 Cen and V Vul, indicating that these systems may be in the final stages of disk dissipation.

- Our mineralogy model indicates the presence of both carbon rich and oxygen rich dust species with a majority of the dust, $80\% \pm 1\%$ by volume on average, in the form of amorphous carbon and graphite. All of the stars display this dual chemistry circumstellar dust. This requires that either these stars result from a narrow range of masses that terminate AGB evolution just as the carbon exceeds the oxygen abundance or that the formation process is not single star evolution. We speculate the formation process is common envelope evolution.

- The spectra do not exhibit any obvious crystalline emission features and our model only predicts UY CMa, RU Cen, and AC Her to have crystalline forsterite at volume fractions of $4\% \pm 0.9\%$, $1\% \pm 0.3\%$, and $1\% \pm 0.1\%$, respectively.

- Most of the spectra show a low peak to continuum value (i.e. < 2.0) and a low 10/20 μm ratio (i.e. < 50) indicating that the grains are relatively large and have undergone significant processing, supporting the hypothesis that the dust is constrained to a Keplerian disk and that we are viewing the heavily processed, central regions of the disk from a nearly face-on orientation.

- The average composition of the SRd variables contains 8% more small carbon

dust and less graphite (14% less of the small species and 5% less of the large) than the average composition of the RV Tauri stars. Of the three SRd variables modeled in this work, none of them contained the large carbon species–on average the RV Tauri stars contained 13% by volume. Overall the average volume fraction of large grains for the SRd variables was 16% compared to 30% for the RV Tauri stars. The paucity of large grains around any of the SRd variables supports the hypothesis that these stars are single star systems.

– Between the featureless IR dust species, amorphous carbon is included in more of our models (16 out of 17) than metallic iron (4 out of 17).

Chapter 4

Summary

The goal of this thesis was to study the mineralogy and mass-loss histories of post-main sequence stars using airborne mid-IR imaging and spectroscopy. With the Faint Object infraRed CAmera for the SOFIA Telescope (FORCAST) on board the NASA Stratospheric Observatory for Infrared Astronomy (SOFIA) the candidate luminous blue variables MN 90 and HD 168625 have been imaged with near diffraction limited resolution. Two-dimensional radiative transfer modeling of MN 90 and HD 168625 reveals recent mass-loss in the circumstellar environment. The SOFIA/FORCAST grism spectroscopic study of 15 RV Tauri stars and 3 SRd variable stars, a sample of proto-planetary nebulae, demonstrated the diversity of dust features present in these systems.

The SOFIA/FORCAST images between 7.7 – 37.1 μm of HD 168625 compliment previously obtained mid-IR imaging. The dust color temperature and optical depth maps that we derive from our observations show evidence for the limb-brightened peaks of an equatorial torus and for very small, transiently heated dust grains. A least-squares fit of a $\lambda B_\lambda(T_d)$ curve with emissivity $Q_{abs}(\lambda) \propto \lambda^{-1}$ to the SED of HD 168625 yields an estimated dust temperature of 160 K, with the peak of the emission at 18 μm. Our detailed radiative transfer model using **2-D**ust supports the claim that the dust resides in a thin, axisymmetric dust shell and estimates that HD 168625 lost 2.4×10^{-3} $M_\odot$ of dust in a massive stellar wind with a mass-loss rate of 1.3×10^{-7} $M_\odot\, yr^{-1}$ that ended approximately 2600 years ago. Using a canonical gas-to-dust ratio of 100 we estimate a total mass-loss of 0.24 $M_\odot$ for HD 168625 which is a lower limit given we are only observing the inner equatorial torus, $\sim 10 - 20\%$ of the solid angle of the entire nebula.

These **2-D**ust estimates assume that HD 168625 has a luminosity of 2.5×10^4 $L_\odot$, at the lower end of luminosities of LBVs in their quiescent state, and a distance of 1.2 kpc. Our SOFIA/FORCAST image at 37.1 μm of MN 90 shows a limb-brightened, spherical dust shell surrounding the central star. A least-squares fit of a $\lambda B_\lambda(T_d)$ curve with emissivity $Q_{abs}(\lambda) \propto \lambda^{-1}$ to the SED of MN 90 yields a dust temperature of 69 K, with the peak of the emission at 42 μm. Our **2-D**ust model supports the idea that the dust resides in a thin, spherical dust shell and estimates that MN 90 lost 2.5×10^{-2} $M_\odot$ of dust in a massive stellar wind with a mass-loss rate of 8.3×10^{-6} $M_\odot\, yr^{-1}$ that ended approximately 6000 years ago. Using the canonical gas-to-dust mass ratio of 100, we estimate a total mass-loss of 2.5 $M_\odot$ for MN 90. These **2-D**ust estimates assume that MN 90 has a luminosity of 7.1×10^4 $L_\odot$, at the lower end of luminosities of LBVs in their quiescent state, and a distance of 4.2 kpc. Our **2-D**ust model of MN 90 has good agreement with observations if we assume very small, transiently heated silicate grains. With a more direct and reliable measurement of the distances to MN 90 and HD 168625, more accurate dust mass and mass-loss rates could be estimated. The uncertainty in the distance to MN 90 and the limited information regarding its physical parameters make it a prime candidate for follow-up observations and photometric monitoring.

The SOFIA/FORCAST 5 – 40 μm mid-infrared grism spectroscopic survey of RV Tauri and SRd variable stars suggests the presence of both carbon rich and oxygen rich dust species, with a majority of the dust being in the form of amorphous carbon and graphite, for all of the stars observed. This requires that either these stars result from a narrow range of masses that terminate AGB evolution just as the carbon exceeds the oxygen abundance or that the formation process is not single star evolution. We speculate the formation process is common envelope evolution of a binary system where the carbon and oxygen abundances can rapidly change. The spectra do not exhibit any obvious crystalline emission features and our model only predicts UY CMa, RU Cen, and AC Her to have crystalline forsterite at volume fractions less than 4%. Most of the spectra show a low peak to continuum value (i.e. < 2.0) and a low 10/20 μm ratio (i.e. < 50) indicating that the grains are relatively large and have undergone significant processing, supporting the hypothesis that the dust is constrained to a Keplerian disk and that we are viewing the heavily processed, central regions of the disk from a nearly face-on orientation. These observations support the hypothesis that the systems in

question are at an advanced stage in their transition to PNe.

References

Acke, B., Degroote, P., Lombaert, R., et al. 2013, A&A, 551, A76

Alcolea, J., & Bujarrabal, V. 1991, A&A, 245, 499

Aldoretta, E. J., Caballero-Nieves, S. M., Gies, D. R., et al. 2015, AJ, 149, 26

Arneson, R. A., Gehrz, R. D., Woodward, C. E., et al. 2017, ApJ, 843, 51

Becklin, E. E., Tielens, A. G. G. M., Gehrz, R. D., & Callis, H. H. S. 2007, in Proc. SPIE, Vol. 6678, Infrared Spaceborne Remote Sensing and Instrumentation XV, 66780A

Beelen, A., Cox, P., Benford, D. J., et al. 2006, ApJ, 642, 694

Begemann, B., Dorschner, J., Henning, T., et al. 1997, ApJ, 476, 199

Benjamin, R. A., Churchwell, E., Babler, B. L., et al. 2003, PASP, 115, 953

Berriman, G. B. 2008, in Proc. SPIE, Vol. 7016, Observatory Operations: Strategies, Processes, and Systems II, 701618

Bertoldi, F., & Cox, P. 2002, A&A, 384, L11

Blommaert, J. A. D. L., de Vries, B. L., Waters, L. B. F. M., et al. 2014, A&A, 565, A109

Bohren, C. F., & Huffman, D. R. 1983, Absorption and Scattering of Light by Small Particles (New York: Wiley)

Bouwman, J., Meeus, G., de Koter, A., et al. 2001, A&A, 375, 950

Bradley, J., Dai, Z. R., Erni, R., et al. 2005, Science, 307, 244

Bujarrabal, V., Alcolea, J., Van Winckel, H., Santander-García, M., & Castro-Carrizo, A. 2013, A&A, 557, A104

Bujarrabal, V., Bachiller, R., Alcolea, J., & Martin-Pintado, J. 1988, A&A, 206, L17

Bujarrabal, V., Castro-Carrizo, A., Alcolea, J., & Van Winckel, H. 2015, A&A, 575, L7

Bujarrabal, V., Gomez-Gonzalez, J., & Planesas, P. 1989, A&A, 219, 256

Bujarrabal, V., van Winckel, H., Neri, R., et al. 2007, A&A, 468, L45

Cami, J., de Jong, T., Justtannont, K., Yamamura, I., & Waters, L. B. F. M. 1998, Ap&SS, 255, 339

Cardelli, J. A., Clayton, G. C., & Mathis, J. S. 1989, ApJ, 345, 245

Carey, S. J., Noriega-Crespo, A., Mizuno, D. R., et al. 2009, PASP, 121, 76

Chan, S. J., & Kwok, S. 1990, A&A, 237, 354

Chentsov, E. L., & Gorda, E. S. 2004, Astronomy Letters, 30, 461

Chentsov, E. L., & Luud, L. 1989, Astrophysics, 31, 415

Churchwell, E., Babler, B. L., Meade, M. R., et al. 2009, PASP, 121, 213

Clark, J. S., Larionov, V. M., & Arkharov, A. 2005, A&A, 435, 239

Clarke, M., Vacca, W. D., & Shuping, R. Y. 2015, in Astronomical Society of the Pacific Conference Series, Vol. 495, Astronomical Data Analysis Software an Systems XXIV (ADASS XXIV), ed. A. R. Taylor & E. Rosolowsky, 355

Crapsi, A., van Dishoeck, E. F., Hogerheijde, M. R., Pontoppidan, K. M., & Dullemond, C. P. 2008, A&A, 486, 245

Dayal, A., Hoffmann, W. F., Bieging, J. H., et al. 1998, ApJ, 492, 603

de Ruyter, S., van Winckel, H., Dominik, C., Waters, L. B. F. M., & Dejonghe, H. 2005, A&A, 435, 161

de Ruyter, S., van Winckel, H., Maas, T., et al. 2006, A&A, 448, 641

Deroo, P., Reyniers, M., van Winckel, H., Goriely, S., & Siess, L. 2005, A&A, 438, 987

Deroo, P., van Winckel, H., Min, M., et al. 2006, A&A, 450, 181

Dorschner, J., Begemann, B., Henning, T., Jaeger, C., & Mutschke, H. 1995, A&A, 300, 503

Draine, B. T. 2003, ARA&A, 41, 241

Draine, B. T., & Lee, H. M. 1984, ApJ, 285, 89

Duley, W. W., & Seahra, S. 1998, ApJ, 507, 874

Dwarkadas, V. V., & Owocki, S. P. 2002, ApJ, 581, 1337

Dwek, E., Galliano, F., & Jones, A. P. 2007, ApJ, 662, 927

Egan, M. P., Price, S. D., & Kraemer, K. E. 2003, in Bulletin of the American Astronomical Society, Vol. 35, American Astronomical Society Meeting Abstracts, 1301

Evans, A., Tyne, V. H., Smith, O., et al. 2005, MNRAS, 360, 1483

Fokin, A. B. 1994, A&A, 292, 133

Foreman-Mackey, D. 2016, The Journal of Open Source Software, 24, doi:10.21105/joss.00024

Frank, A., Balick, B., & Davidson, K. 1995, ApJ, 441, L77

Fritz, T. K., Gillessen, S., Dodds-Eden, K., et al. 2011, ApJ, 737, 73

Gehrz, R. 1989, in IAU Symposium, Vol. 135, Interstellar Dust, ed. L. J. Allamandola & A. G. G. M. Tielens, 445

Gehrz, R. D. 1972, ApJ, 178, 715

Gehrz, R. D., Becklin, E. E., de Pater, I., et al. 2009, Advances in Space Research, 44, 413

Gehrz, R. D., Jones, T. J., Woodward, C. E., et al. 1992, ApJ, 400, 671

Gehrz, R. D., & Ney, E. P. 1972, PASP, 84, 768

Gehrz, R. D., & Woolf, N. J. 1970, ApJ, 161, L213

Gehrz, R. D., Roellig, T. L., Werner, M. W., et al. 2007, Review of Scientific Instruments, 78, 011302

Gezer, I., Van Winckel, H., Bozkurt, Z., et al. 2015, MNRAS, 453, 133

Gielen, C., van Winckel, H., Min, M., Waters, L. B. F. M., & Lloyd Evans, T. 2008, A&A, 490, 725

Gielen, C., van Winckel, H., Waters, L. B. F. M., Min, M., & Dominik, C. 2007, A&A, 475, 629

Gielen, C., van Winckel, H., Reyniers, M., et al. 2009, A&A, 508, 1391

Gielen, C., Bouwman, J., van Winckel, H., et al. 2011, A&A, 533, A99

Giridhar, S., Lambert, D. L., & Gonzalez, G. 1998, ApJ, 509, 366

—. 2000, ApJ, 531, 521

Giridhar, S., Lambert, D. L., Reddy, B. E., Gonzalez, G., & Yong, D. 2005, ApJ, 627, 432

Gonzalez, G., Lambert, D. L., & Giridhar, S. 1997a, ApJ, 481, 452

—. 1997b, ApJ, 479, 427

Gordon, M. S., Shenoy, D., Humphreys, R. M., et al. 2017, ArXiv e-prints, arXiv:1708.00018

Green, G. M., Schlafly, E. F., Finkbeiner, D. P., et al. 2015, ApJ, 810, 25

Griffin, M. J., Abergel, A., Abreu, A., et al. 2010, A&A, 518, L3

Groenewegen, M. A. T., Waelkens, C., Barlow, M. J., et al. 2011, A&A, 526, A162

Guzman-Ramirez, L., Lagadec, E., Wesson, R., et al. 2015, MNRAS, 451, L1

Gvaramadze, V. V., Kniazev, A. Y., & Fabrika, S. 2010, MNRAS, 405, 1047

Hardy, A., Schreiber, M. R., Parsons, S. G., et al. 2016, MNRAS, 459, 4518

He, J. H., Szczerba, R., Hasegawa, T. I., & Schmidt, M. R. 2014, ApJS, 210, 26

Henning, T., Begemann, B., Mutschke, H., & Dorschner, J. 1995, A&AS, 112, 143

Henning, T., & Mutschke, H. 1997, A&A, 327, 743

Herter, T. L., Adams, J. D., De Buizer, J. M., et al. 2012, ApJ, 749, L18

Hillen, M., de Vries, B. L., Menu, J., et al. 2015, A&A, 578, A40

Hillen, M., Van Winckel, H., Menu, J., et al. 2017, A&A, 599, A41

Hinkle, K. H., Brittain, S. D., & Lambert, D. L. 2007, ApJ, 664, 501

Honda, M., Kataza, H., Okamoto, Y. K., et al. 2004, ApJ, 610, L49

Humphreys, R. M., Davidson, K., & Smith, N. 1999, PASP, 111, 1124

Hutsemekers, D., van Drom, E., Gosset, E., & Melnick, J. 1994, A&A, 290, 906

Iben, Jr., I. 1981, ApJ, 246, 278

Jaeger, C., Molster, F. J., Dorschner, J., et al. 1998a, A&A, 339, 904

Jaeger, C., Mutschke, H., & Henning, T. 1998b, A&A, 332, 291

Juhász, A., Bouwman, J., Henning, T., et al. 2010, ApJ, 721, 431

Jura, M. 1986, ApJ, 309, 732

Karakas, A. I., & Lattanzio, J. C. 2014, PASA, 31, e030

Kashi, A., & Soker, N. 2011, MNRAS, 417, 1466

Kastner, J. H., Huenemoerder, D. P., Schulz, N. S., et al. 2004, ApJ, 605, L49

Kastner, J. H., Principe, D. A., Punzi, K., et al. 2016, AJ, 152, 3

Kemper, F., de Koter, A., Waters, L. B. F. M., Bouwman, J., & Tielens, A. G. G. M. 2002, A&A, 384, 585

Kemper, F., Vriend, W. J., & Tielens, A. G. G. M. 2004, ApJ, 609, 826

Kemper, F., Waters, L. B. F. M., de Koter, A., & Tielens, A. G. G. M. 2001, A&A, 369, 132

Kiss, L. L., Derekas, A., Szabó, G. M., Bedding, T. R., & Szabados, L. 2007, MNRAS, 375, 1338

Knapp, G. R., Sandell, G., & Robson, E. I. 1993, ApJS, 88, 173

Kniazev, A. Y., Gvaramadze, V. V., & Berdnikov, L. N. 2015, MNRAS, 449, L60

Koike, C., Chihara, H., Tsuchiyama, A., et al. 2003, A&A, 399, 1101

Kukarkin, B. V. 1958, in IAU Symposium, Vol. 5, Comparison of the Large-Scale Structure of the Galactic System with that of Other Stellar Systems, ed. N. G. Roman, 49

Langer, N., Hamann, W.-R., Lennon, M., et al. 1994, A&A, 290, 819

Lau, R. M., Herter, T. L., Morris, M. R., & Adams, J. D. 2014, ApJ, 785, 120

Lau, R. M., Herter, T. L., Morris, M. R., Becklin, E. E., & Adams, J. D. 2013, ApJ, 775, 37

Leinonen, J. 2012, Python code for calculating Mie scattering from single and dual-layered spheres

Lisse, C. M., Christian, D. J., Wolk, S. J., et al. 2017, AJ, 153, 62

Lü, G., Zhu, C., & Podsiadlowski, P. 2013, ApJ, 768, 193

Maas, T., Van Winckel, H., & Lloyd Evans, T. 2005, A&A, 429, 297

Maas, T., Van Winckel, H., & Waelkens, C. 2002, A&A, 386, 504

Mahy, L., Hutsemékers, D., Royer, P., & Waelkens, C. 2016, A&A, 594, A94

Martayan, C., Lobel, A., Baade, D., et al. 2016, A&A, 587, A115

Mathis, J. S., Rumpl, W., & Nordsieck, K. H. 1977, ApJ, 217, 425

McDonald, I., Zijlstra, A. A., Lagadec, E., et al. 2015, MNRAS, 453, 4324

Meixner, M., Ueta, T., Bobrowsky, M., & Speck, A. 2002, ApJ, 571, 936

Meixner, M., Zalucha, A., Ueta, T., Fong, D., & Justtanont, K. 2004, ApJ, 614, 371

Meixner, M., Ueta, T., Dayal, A., et al. 1999, ApJS, 122, 221

Michałowski, M. J., Murphy, E. J., Hjorth, J., et al. 2010, A&A, 522, A15

Min, M., Hovenier, J. W., & de Koter, A. 2003, A&A, 404, 35

—. 2005, A&A, 432, 909

Mitchell, R. M., & Robinson, G. 1981, MNRAS, 196, 801

Mizuno, D. R., Kraemer, K. E., Flagey, N., et al. 2010, AJ, 139, 1542

Molster, F. J., Waters, L. B. F. M., & Kemper, F. 2010, in Lecture Notes in Physics, Berlin Springer Verlag, Vol. 815, Lecture Notes in Physics, Berlin Springer Verlag, ed. T. Henning, 143–201

Molster, F. J., Waters, L. B. F. M., & Tielens, A. G. G. M. 2002a, A&A, 382, 222

Molster, F. J., Waters, L. B. F. M., Tielens, A. G. G. M., & Barlow, M. J. 2002b, A&A, 382, 184

Molster, F. J., Waters, L. B. F. M., Tielens, A. G. G. M., Koike, C., & Chihara, H. 2002c, A&A, 382, 241

Morgan, W. W., Code, A. D., & Whitford, A. E. 1955, ApJS, 2, 41

Murakami, H., Baba, H., Barthel, P., et al. 2007, PASJ, 59, S369

Nazé, Y., Rauw, G., & Hutsemékers, D. 2012, A&A, 538, A47

Neugebauer, G., Habing, H. J., van Duinen, R., et al. 1984, ApJ, 278, L1

Nota, A., Livio, M., Clampin, M., & Schulte-Ladbeck, R. 1995, ApJ, 448, 788

Nota, A., Pasquali, A., Clampin, M., et al. 1996, ApJ, 473, 946

Nuth, III, J. A., & Hecht, J. H. 1990, Ap&SS, 163, 79

O'Connell, D. J. K. 1961, Ricerche Astronomiche, 6

O'Hara, T. B., Meixner, M., Speck, A. K., Ueta, T., & Bobrowsky, M. 2003, ApJ, 598, 1255

Pasquali, A., Nota, A., Smith, L. J., et al. 2002, AJ, 124, 1625

Payne-Gaposchkin, C. 1952, Nature, 170, 223

Pegourie, B. 1988, A&A, 194, 335

Percy, J. R. 1993, in Astronomical Society of the Pacific Conference Series, Vol. 45, Luminous High-Latitude Stars, ed. D. D. Sasselov, 295

Percy, J. R., & Coffey, J. 2005, Journal of the American Association of Variable Star Observers (JAAVSO), 33, 193

Percy, J. R., Sasselov, D. D., Alfred, A., & Scott, G. 1991, ApJ, 375, 691

Percy, J. R., & Ursprung, C. 2006, Journal of the American Association of Variable Star Observers (JAAVSO), 34, 125

Pilbratt, G. L. 2003, in Proc. SPIE, Vol. 4850, IR Space Telescopes and Instruments, ed. J. C. Mather, 586–597

Poglitsch, A., Waelkens, C., Geis, N., et al. 2010, A&A, 518, L2

Pollack, J. B., Hollenbach, D., Beckwith, S., et al. 1994, ApJ, 421, 615

Popper, D. M., & Seyfert, C. K. 1940, PASP, 52, 401

Preston, G. W., Krzeminski, W., Smak, J., & Williams, J. A. 1963, ApJ, 137, 401

Rao, S. S., & Giridhar, S. 2014, RMxAA, 50, 49

Rieke, G. H., Young, E. T., Engelbracht, C. W., et al. 2004, ApJS, 154, 25

Robberto, M., & Herbst, T. M. 1998, ApJ, 498, 400

Robinson, G., & Hyland, A. R. 1977, MNRAS, 180, 495

Rouleau, F., Henning, T., & Stognienko, R. 1997, A&A, 322, 633

Sakon, I., Sako, S., Onaka, T., et al. 2016, ApJ, 817, 145

Schoenberner, D. 1983, ApJ, 272, 708

Shenoy, D., Humphreys, R. M., Jones, T. J., et al. 2016, AJ, 151, 51

Shenton, M., Evans, A., & Williams, P. M. 1995, MNRAS, 273, 906

Shenton, M., Albinson, J. S., Barrett, P., et al. 1992, A&A, 262, 138

Skinner, C. J. 1997, in Astronomical Society of the Pacific Conference Series, Vol. 120, Luminous Blue Variables: Massive Stars in Transition, ed. A. Nota & H. Lamers, 322

Skrutskie, M. F., Cutri, R. M., Stiening, R., et al. 2006, AJ, 131, 1163

Smith, C. H., Aitken, D. K., & Roche, P. F. 1994, MNRAS, 267, 225

Smith, N. 2007, AJ, 133, 1034

—. 2014, ARA&A, 52, 487

Smith, N., & Stassun, K. G. 2017, AJ, 153, 125

Smith, N., & Tombleson, R. 2015, MNRAS, 447, 598

Smith, N., & Townsend, R. H. D. 2007, ApJ, 666, 967

Smith, N., Vink, J. S., & de Koter, A. 2004, ApJ, 615, 475

Sogawa, H., & Kozasa, T. 1999, ApJ, 516, L33

Speck, A. K., Corman, A. B., Wakeman, K., Wheeler, C. H., & Thompson, G. 2009, ApJ, 691, 1202

Speck, A. K., Meixner, M., & Knapp, G. R. 2000, ApJ, 545, L145

Speck, A. K., Thompson, G. D., & Hofmeister, A. M. 2005, ApJ, 634, 426

Sterken, C., Arentoft, T., Duerbeck, H. W., & Brogt, E. 1999, A&A, 349, 532

Straniero, O., Chieffi, A., Limongi, M., et al. 1997, ApJ, 478, 332

Straniero, O., Gallino, R., & Cristallo, S. 2006, Nuclear Physics A, 777, 311

Suh, K.-W. 2000, MNRAS, 315, 740

—. 2002, MNRAS, 332, 513

—. 2016, ApJ, 819, 61

Sylvester, R. J., Kemper, F., Barlow, M. J., et al. 1999, A&A, 352, 587

Takeuti, M., & Petersen, J. O. 1983, A&A, 117, 352

Taylor, W. D., Evans, C. J., Simón-Díaz, S., et al. 2014, MNRAS, 442, 1483

Tielens, A. G. G. M., Waters, L. B. F. M., Molster, F. J., & Justtanont, K. 1998, Ap&SS, 255, 415

Tuchman, Y., Lebre, A., Mennessier, M. O., & Yarri, A. 1993, A&A, 271, 501

Ueta, T., & Meixner, M. 2003, ApJ, 586, 1338

Ueta, T., Meixner, M., Dayal, A., et al. 2001a, ApJ, 548, 1020

Ueta, T., Meixner, M., Hinz, P. M., et al. 2001b, ApJ, 557, 831

Umana, G., Buemi, C. S., Trigilio, C., Leto, P., & Hora, J. L. 2010, ApJ, 718, 1036

van Boekel, R., Min, M., Waters, L. B. F. M., et al. 2005, A&A, 437, 189

van Boekel, R., Waters, L. B. F. M., Dominik, C., et al. 2003, A&A, 400, L21

van Genderen, A. M., van den Bosch, F. C., Dessing, F., et al. 1992, A&A, 264, 88

van Marle, A. J., Langer, N., & García-Segura, G. 2007, A&A, 469, 941

van Winckel, H. 2003, ARA&A, 41, 391

Van Winckel, H., Waelkens, C., Fernie, J. D., & Waters, L. B. F. M. 1999, A&A, 343, 202

Van Winckel, H., Waelkens, C., & Waters, L. B. F. M. 1995, A&A, 293

Van Winckel, H., Waelkens, C., Waters, L. B. F. M., et al. 1998, A&A, 336, L17

Volk, K., & Cohen, M. 1989, AJ, 98, 931

Voors, R. H. M., Waters, L. B. F. M., de Koter, A., et al. 2000, A&A, 356, 501

Wachter, S., Mauerhan, J. C., Van Dyk, S. D., et al. 2010, AJ, 139, 2330

Waelkens, C., & Waters, L. B. F. M. 1993, in Astronomical Society of the Pacific Conference Series, Vol. 45, Luminous High-Latitude Stars, ed. D. D. Sasselov, 219

Waters, L. B. F. M., Trams, N. R., & Waelkens, C. 1992, A&A, 262, L37

Waters, L. B. F. M., Waelkens, C., Mayor, M., & Trams, N. R. 1993, A&A, 269, 242

Weis, K. 2011, in IAU Symposium, Vol. 272, Active OB Stars: Structure, Evolution, Mass Loss, and Critical Limits, ed. C. Neiner, G. Wade, G. Meynet, & G. Peters, 372–377

Weis, K. 2012, in Astrophysics and Space Science Library, Vol. 384, Eta Carinae and the Supernova Impostors, ed. K. Davidson & R. M. Humphreys, 171

Werner, M. W., Roellig, T. L., Low, F. J., et al. 2004, ApJS, 154, 1

Wright, E. L., Eisenhardt, P. R. M., Mainzer, A. K., et al. 2010, AJ, 140, 1868

Young, E. T., Becklin, E. E., Marcum, P. M., et al. 2012, ApJ, 749, L17

Yuan, H. B., Liu, X. W., & Xiang, M. S. 2013, MNRAS, 430, 2188